Coherent Lifetimes of Excitons and Plexcitons in organic-inorganic Nanostructures

Dissertation der Fakultät für Physik
der Ludwig-Maximilians-Universität München

Vorgelegt von

Thomas Simon
aus Neumarkt i. d. Opf.
2017

Erstgutachter:	Prof. Dr. Jochen Feldmann
Zweitgutachter:	Prof. Dr. Thomas Weitz
Datum der Abgabe:	20. September 2017
Datum der mündlichen Prüfung:	8. Dezember 2017

Für meine Eltern und
Großeltern

Nihil in terra
sine causa fit

Hiob 5, 6

List of publications and awards

Publications presented in this work:

- Thomas Simon, Dimitry Melnikau, Ana Sánchez-Iglesias, Marek Grzelczak, Luis Liz-Marzán, Yury Rakovich, and Jochen Feldmann, A. Urban, *Exploring the Optical Nonlinearities of Plasmon-Exciton Hybrid Resonances in Coupled Colloidal Nanostructures*, **The Journal of Physical Chemistry C** (120), 22, 12226-12233

- Bernhard Bohn, Thomas Simon, Moritz Gramlich, Alexander Richter, Lakshminarayana Polavarapu, Alexander Urban, and Jochen Feldmann, *Dephasing and quantum beating of excitons in methyl ammonium lead iodide perovskite nanoplatelets*, **ACS Photonics**, 10.1021/acsphotonics.7b01292

Further publications:

- Thomas Simon, Nicolas Bouchonville, Maximilian Berr, Alexandar Vaneski, Asmir Adrović, David Volbers, Regina Wyrwich, Markus Döblinger, Andrei Susha, Andrey Rogach, Frank Jäckel, Jacek Stolarczyk, and Jochen Feldmann, *Redox shuttle mechanism enhances photocatalytic H2 generation on Ni-decorated CdS nanorods*, **Nature materials** (13), 11, 1013-1018

- Thomas Simon, Michael Carlson, Jacek Stolarczyk, and Jochen Feldmann, *Electron Transfer Rate vs Recombination Losses in Photocatalytic H2 Generation on Pt-decorated CdS Nanorods*, **ACS Energy Letters** (1), 6, 1137-1142

- Aurora Manzi, Thomas Simon, Clemens Sonnleitner, Markus Döblinger, Regina Wyrwich, Omar Stern, Jacek Stolarczyk, and Jochen Feldmann, *Light-induced cation exchange for copper sulfide based CO2 reduction,* **Journal of the American Chemical Society** (137), 44, 14007-14010

- Vincent Lau, Victor Yu, Florian Ehrat, Tiago Botari, Igor Moudrakovski, Thomas Simon, Viola Duppel, Elise Medina, Jacek Stolarczyk, Jochen Feldmann, Volker Blum, and Bettina Lotsch, *Urea-Modified Carbon Nitrides: Enhancing Photocatalytic Hydrogen Evolution by Rational Defect Engineering*, **Advanced Energy Materials**, DOI: 10.1002/aenm.201602251

- Florian Ehrat, Thomas Simon, Jacek Stolarczyk, and Jochen Feldmann, *Size Effects on Photocatalytic H2 Generation with CdSe/CdS Core-Shell Nanocrystals*, **Zeitschrift für Physikalische Chemie** (229), 1-2, 205-219

- Michael Carlson, Thomas Simon, Jacek Stolarczyk, and Jochen Feldmann*, Length dependence of photocatalytic activity with CdS/Pt matchstick structures*, manuscript in preparation 2017

- Carlos Cardenas-Daw, Thomas Simon, Jacek Stolarczyk, and Jochen Feldmann, *The migration of constituent protons in hybrid organic-inorganic perovskite triggers intrinsic doping*, submitted 2017

Awards:

- CeNS Publication award 2014, Category: Best interdisciplinary publication
- CeNS Travelling award 2016 for attending SPIE Optics & Photonics, San Diego

Conference contributions

- Thomas Simon, Michael Carlson, Jacek Stolarczyk and Jochen Feldmann, *Optimizing the charge transport for photocatalytic H_2 generation*, **NIM Young Ideas in Nanoscience**, Munich, Germany, May 2017

- Thomas Simon, *Time Resolved Fluorescence Spectroscopy*, **Workshop on optical spectroscopy of new materials**, Syracuse, Italy, March 2017

- Thomas Simon, Dimitry Melnikau, Ana Sanchez-Iglesia, Marek Grzelczak, Luis M Liz-Marzán, Yury P Rakovich, Jochen Feldmann, *Alexander S Urban Coupled plasmon-exciton hybrid excitations in colloidal gold nanorods coated with J-aggregated dye molecules*, **SPIE Optics & Photonics**, San Diego, USA, September 2016

- Thomas Simon, *Ultrafast non-linear optical dynamics in strongly coupled plasmon/dye hybrid structures & Four wave mixing*, **Workshop on Photonics and Optoelectronics with New Materials**, Fall Lenggries, Germany, July 2016

- Thomas Simon, *Gold und Farbe – eine bunte Kopplung,* **Nacht der Ideen**, Berlin, June 2016

- Thomas Simon, Michael Carlson, Jacek Stolarczyk, and Jochen Feldmann, *Electron-hole recombination dynamics in CdS nanocrystals: limiting steps of photocatalytic H2 generation*, **DPG Frühjahrstagung**, Regensburg, Germany, March 2016

- Thomas Simon, Michael Carlson, Jacek Stolarczyk and Jochen Feldmann, *Optimizing the charge transport for photocatalytic H_2 generation*, **SolTech Workshop**, Munich, Germany, March 2016

- Thomas Simon, Dimitry Melnikau, Alexander Urban, Jochen Feldmann, and Yury Rakovich,*Transient absorption spectroscopy on gold nanorods coated with molecular J-aggregates*, **DPG Frühjahrstagung**, Berlin, Germany, March 2015

- Thomas Simon, Dimitry Melnikau, Alexander Urban, Jacek Stolarczyk, Yury Rakovich and Jochen Feldmann, *Non-linear spectroscopy with J-aggregates coupled on Au-nanorods – a study of excitonic-plasmonic hybrid resonances*, **SolTech Workshop**, Kloster Banz, March 2015

- Thomas Simon, *Ultrashort laser pulse generation and ultrafast spectroscopy, Workshop on Photonics and Optoelectronics*, Riezlern, Austria, October 2014

- Thomas Simon, Jacek Stolarczyk and Jochen Feldmann, *Redox shuttle mechanism enhances photocatalytic H2 generation on Ni-decorated CdS nanorods,* **Nanotexnology**, Thessaloniki, Greece July 2014

- Thomas Simon, Maximilian Berr, Aleksandar Vaneski, David Volbers, Regina Wyrwich, Markus Doeblinger, Andrei Susha, Andrey Rogach, Frank Jaeckel, Jacek Stolarczyk and Jochen Feldmann, *Highly efficient photocatalytic water splitting with colloidal CdS nanorods by mediated hole scavenging*, **EMRS**, Lille, France, May 2014

- Thomas Simon, Nicolas Bouchonville, Maximilian Berr, Alexandar Vaneski, Asmir Adrovic, David Volbers, Regina Wyrwich, Markus Döblinger, Andrei Susha, Andrey Rogach, Frank Jäckel, Jacek Stolarczyk and Jochen Feldmann, *Highly efficient H_2 generation with CdS nanorods by redox shuttle mediated hole scavenging with OH radicals*, **Nanax**, Bad Hofgastein, Austria, May 2014

- Thomas Simon, Nicolas Bouchonville, Maximilian Berr, Alexandar Vaneski, Asmir Adrovic, David Volbers, Regina Wyrwich, Markus Döblinger, Andrei Susha, Andrey Rogach, Frank Jäckel, Jacek Stolarczyk and Jochen Feldmann, *Highly efficient H_2 generation with CdS nanorods by redox shuttle mediated hole scavenging with OH radicals*, **SolTech Workshop**, Wildbad Kreuth, Germany, April 2014

- Thomas Simon, Jacek Stolarczyk and Jochen Feldmann, *Highly efficient photocatalysis enhanced by a cyclic hole shuttling process*, **NIM Young ideas in Nanoscience**, Munich, Germany, November 2013

Table of Content

Kurzfassung

Kohärente Phänomene spielen in vielen Teilbereichen der Physik eine zentrale Rolle. Sie in Materie direkt zu beobachten ist jedoch oftmals schwierig, da die Lebensdauer auf Grund von Störeinflüssen sehr kurz ist. In der vorliegenden Arbeit wurden kohärente Dynamiken von Polarisationen in Nanokristallen mit Ultrakurzzeitspektroskopie untersucht. Die Besonderheit der Nanokristalle war hierbei, dass sie sowohl aus einer organischen als auch aus einer anorganischen Komponente aufgebaut waren. Bei dem einen Materialkomplex handelte es sich um Goldnanostäbchen, die mit einem organischen Farbstoff beschichtet waren. Das andere Materialsystem bestand aus einem Halbleiter mit organischen Methylammoniumkationen und anorganischen Bleitrihalidanionen in Perowskit Kristallstruktur. Beide Systeme sind ein aktueller Forschungsschwerpunkt: Zum einen eignen sich kleine Edelmetallpartikel auf Grund kollektiver Schwingungsmoden der Leitungsbandelektronen (Plasmonen) ideal zur lokalen Verstärkung eines elektromagnetischen Feldes. Zum anderen konnten unlängst mit vergleichbaren Halbleitermaterialen äußerst effiziente Solarzellen und Leuchtdioden gefertigt werden.

Zwei unterschiedliche kohärente Prozesse wurden mit den Strukturen untersucht: Bei dem ersten handelte es sich um Rabi Oszillationen zwischen den Anregungen auf dem Farbstoff in Form von Exzitonen und der Polarisation der Plasmonen auf den Goldnanostäbchen. Auf Grund des starken elektromagnetischen Feldes und des großen Dipolmoments der Farbstoffmoleküle kommt es zur starken Kopplung und einem periodischen Austausch von Energie durch zyklische Emission und Reabsorption von Photonen. Die spektrale Konsequenz ist die Ausbildung zweier neuer Resonanzen des gekoppelten Systems. Diese hybriden Anregungen zwischen Plasmonen und Exzitonen werden als *Plexzitonen* bezeichnet. Im Rahmen dieser Arbeit wurde deren optisches Verhalten unter nichtlinearer Anregung untersucht. Dabei konnte gezeigt werden, dass Plexzitonen sowohl plasmonische als auch exzitonische Eigenschaften besitzen, welche durch den spektralen Überlapp zwischen Plasmon und Exziton variiert werden können. Dies ist von besonderem Interesse, da eine derartige hybride Kombination zwischen Metall und Halbleiter vielschichtige Anwendungsgebiete haben könnte.

Der zweite kohärente Prozess war entartete Vier-Wellen-Mischung mit ultrakurzen Laserpulsen und wurde an Nanokristallen aus organisch-anorganischen Halbleiterhybriden durchgeführt. Das Experiment erlaubte die Bestimmung der Lebensdauer kohärenter Polarisationen in der Zeitdomäne. Somit konnte für vergleichbare Systeme die Dephasierungszeit (T_2) von Exzitonen gemessen werden, welche umgekehrt proportional zur entsprechenden homogenen Linienbreite ist. Es konnte gezeigt werden, dass die homogene Linienbreite mit etwa 2-3 meV nur einen Bruchteil der gesamten Linienbreite von Exzitonen in einem Film bei Temperaturen von 5 K ausmacht. Mit demselben Experiment konnte darüber hinaus die Bindungsenergie der Exzitonen sehr genau auf 28 ± 2 meV bestimmt werden.

Beide Experimente stellen einen wichtigen Beitrag für zukünftige Arbeiten dar, weil sie zum einen zum Verständnis kohärenter Phänomene an komplexen makroskopischen Strukturen beitragen und zum anderen präzise Werte für wichtige Materialkonstanten quantifizieren.

Abstract

Coherent phenomena play an important role in many areas of physics. A direct observation in matter is frequently less trivial, since their lifetimes are very short due to dephasing effects. In this work, coherent dynamics of polarizations in nanocrystals were investigated by means of ultrafast spectroscopy. The nanocrystals distinguish themselves by consisting of both an organic and an inorganic component. The first material complex were gold nanorods coated with organic dye molecules. The other material system was a semiconductor comprising organic methylammonium cations and inorganic lead trihalide anions in a perovskite crystal structure. Both material systems are under the focus of current research. On the one hand, small noble metal particles exhibit strong local electromagnetic fields due to collective oscillations of the conduction band electrons (plasmons). On the other hand, highly efficient solar cells and light emitting diodes have been recently fabricated with comparable semiconductors.

Two different coherent processes were investigated with these structures: The first one were Rabi oscillations between excitations of the dye in the form of excitons and the plasmon polarization of the gold nanorods. Because of the high electromagnetic field strength and the extraordinary dipole moment of the dye molecules, both components are in the strong coupling regime and periodically exchange energy by cyclic emission and reabsorption of photons. As a consequence of this, two new spectral resonances of the coupled system emerge. These hybrid excitations between plasmons and excitons are called *plexcitons*. In the scope of this work, their optical behaviour was investigated under nonlinear excitation. It could be shown that plexcitons show both plasmonic and excitonic signatures which can be tuned by the spectral overlap between plasmon and exciton. Since such a hybrid combination between a metal and a semiconductor has potential for various applications, it is of special interest.

The second coherent process was degenerate four-wave mixing with ultrashort laser pulses and was conducted on nanocrystals of the hybrid organic-inorganic semiconductor. Coherent lifetimes of polarizations could be measured in the time domain. The dephasing time (T_2) of excitons for similar material systems was obtained which is proportional to the reciprocal of the respective homogeneous linewidth. It could be shown that the homogeneous linewidth of 2-3 meV is only a fraction of the total linewidth of excitons in a film at a temperature of 5 K. Furthermore, the exciton binding energy could be precisely measured to 28 ± 2 meV with the same experimental approach.

Both experiments constitute an important contribution for future studies because they facilitate the understanding of coherent phenomena on complex macroscopic structures and quantify reliable values for essential material constants.

1 Introduction

Nine months before I started working on this PhD thesis, the Noble prize in physics was awarded to David J. Wineland and Serge Haroche “for ground-breaking experimental methods that enable measuring and manipulation of individual quantum systems”. Both conducted experiments to measure the quantum state of a system while it is in a coherent superposition of two (or more) states [1-3]. This problem, first proposed by Erwin Schrödinger, got popular as “Schrödinger´s cat” because it illustrates the meaning of a coherent state by a paradox [4]: A cat can be either dead or alive in the daily world (described by classical physics). However, in quantum mechanics also a hybrid state where it is both dead AND alive can exist until the condition of the cat is measured. This preposterous construct explains a coherent superposition of two different quantum states, for example an atom in the ground or excited state.

Even today there is no clear scientific consensus about the “Schrödinger´s cat” conundrum which means that interpretations of quantum mechanical effects in the macroscopic world are lacking. Nevertheless, the coherence of a quantum state has a finite lifetime and gets diminished by so-called “decoherence” [5]. The decoherence of electromagnetic excitations in matter are quantified by the “dephasing time” [6]. The term de-phasing already describes the reason for the loss of coherence: Each subsystem of an ensemble can have its individual state. A coherent state only exists as long as all systems have a well-defined phase relation [7]. With higher complexity of the entire system, its degrees of freedom increase. The work of Heinz-Dieter Zeh suggests that the decoherence through interaction with the environment (thermal radiation, gas molecules, cosmic microwave back ground, etc.) [8, 9] is a considerable reason why quantum mechanical effects in the Schrödinger´s cat experiment have an extremely short lifetime. The experimental observation is neither possible with human senses nor any technical/experimental techniques which are known up to now. However, coherent effects are not “invisible”.

There are various experimental approaches to detect the coherence of electromagnetic excitations in matter. The motivation for my PhD thesis was to study coherent optical effects on new material systems.

Material science has made remarkable progress over the past three decades in the fabrication of nanostructures for many materials. Two material families are distinguished for solids: metals and dielectrics. Although metal nanoparticles were unwittingly used by the Romans to dye glass [10], they did not receive much scientific attention until the end of the 1990s. These structures can exhibit collective and coherent oscillations of the conduction band electrons, the so-called plasmon resonances [11]. Such materials have found numerous applications for example in sensing [12-14] and waveguiding [15, 16]. Semiconductors as an example for dielectric materials have been indispensable since the invention of the transistor [17] and inorganic semiconductors, especially silicon, have initiated the “digital revolution”; however, the price of silicon is the main limiting factor for the fabrication of voluminous devices like solar cells or display/illumination applications.

The keyword “organic semiconductors” summarizes any and all semiconducting materials of low-cost carbon base. Despite remarkable success throughout the past 30 years [18-22], organic devices have yet to outperform traditional semiconductors. Recently, a new hybrid material system between an organic and an inorganic semiconductor has been found to have remarkable properties for both electricity [23-26] and light generation [27, 28]. The material crystalizes in a perovskite crystal structure with the arbitrary molecular formula ABX_3. The cation A is a small organic molecule like methylammonium $CH_3NH_3^+$ or formamidinium $HC(NH_2)^+$ [29, 30]. A fully inorganic material with similar properties can be obtained with caesium ions [31-33]. According to the perovskite crystal lattice, the cation A is in the centre of a cage spanned by corner-sharing BX_6^{4-} octahedra. The other cation B is either a bivalent lead or tin metal ion [34]. Since the anion X consists of halide ions like chloride, bromide and iodide, the materials are sometimes referred to as mixed halide perovskites. The most common compound is methylammonium lead iodide $CH_3NH_3PbI_3$.

Hybrid materials can also be created by using plasmonic metal particles: Fluorescent materials as second compound are particularly interesting as the polarization of the plasmon can influence the emission rates similar to optical modes in a cavity [35-37]. In my thesis, I studied coherent nonlinear optical effects in two different colloidal hybrid nanostructures. The first one consisted of ellipsoidal gold nanocrystals encapsulated by organic cyanine dye molecules in a J-aggregate arrangement. The second material system were nanocrystals of lead halide perovskites. The experiments with the respective motivations are briefly introduced in the following.

On the one hand, the electromagnetic field of the plasmon polarization is greatly enhanced on the surface of metal particles and on the other hand, the dipole moment of J-aggregates is very high due to internal assembly of the dye molecules. Therefore, the coupling strength as a product of both quantities is significant for the first investigated structure. Here, the plasmon polarization not only influences the emission rates of the dye excitations; similar to molecular orbitals, both form hybrid states comprised by a superposition of purely plasmonic and purely excitonic modes, the so-called plexcitons. As described above, coherently coupled states are interesting since the material is simultaneously in both different states. The first experiment was dedicated to analyse whether plexcitons are plasmons and excitons at the same time. Femtosecond transient absorption spectroscopy was applied to discriminate between plasmonic and excitonic signatures. The subsequent analysis of the composite structures clearly reveals that plexcitons have both plasmonic and excitonic behaviour depending on the spectral overlap between the dye transition and the plasmon resonance. All experimental observations could be quantitatively explained on the basis of a simple coupled Lorentz oscillator model.

Degenerate four-wave mixing was applied to investigate third-order nonlinear optical effects of different lead halide perovskite nanostructures. The experimental method can be understood analogous to a spin echo where the dephasing time can be measured in the time domain. In my thesis, I measured dephasing times of excitons in methylammonium lead iodide/bromide nanocrystals in the subpicosecond regime at low

temperature (<10 K). Furthermore, I could observe the dynamics of a coherent superposition of different excitations within the material. This approach enabled the determination of the exciton binding energy in the time domain for lead halide perovskite nanocrystals. I obtained a value of 28 meV for bulk-like methylammonium lead iodide. So far there has been a controversial debate about the exact value because it is shaded by ensemble effects in many other experimental approaches [38].

The following thesis is structured in five parts. The next chapter introduces the theoretical background which is essential to understand the experimental work done in this thesis. I tried to shorten it and present only text-book knowledge allowing a schematic understanding of the physics behind the empirical data. The third chapter shows the most important techniques which were applied to achieve femtosecond resolution in the experiments. Chapters four and five contain the actual experimental results of this thesis: The fourth chapter comprises the work on gold nanorods coated with J-aggregate dye molecules in the strong coupling regime. Chapter five gives an overview about various different four-wave mixing experiments with lead halide perovskite nanocrystals. The main part of this thesis ends with a short conclusion. In this, I summarize the experimental findings of my work and give an outlook to the impacts of my results on the current and future scientific community.

2 Fundamentals and Principles

2.1 Strong coupling of plasmon polarizations and excitons

In the first two sections of this chapter, the optical properties of plasmonic nanoparticles and J-aggregated molecules are introduced. The last one gives a brief overview about strong coupling between a photon mode in a cavity and an emitter. This chapter is essential for the first experimental part (chapter four), where I investigated a material system consisting of gold nanorods and J-aggregated cyanine dye molecules in the strong coupling regime. Here, the electric field of the plasmon polarization of the gold particles couples to the transition dipole moment of the organic dye. The interaction can be understood analogous to the emitter-cavity problem where the plasmon replaces the optical resonator mode. Therefore, similar phenomena can be observed.

2.1.1 Gold nanoparticles as electromagnetic resonators

Dielectric properties of gold

Like the metals copper and silver, gold is a noble metal because of its electron configuration: The d-shells are completely filled with ten electrons whereas only one electron occupies the s-orbital of the respective chemical period. Since all d-bands are below the Fermi level of the solid crystal, they do not contribute to electric conductivity and account for the high chemical stability. The metallic properties originate from the single valence electrons in the s-orbitals since they are bound very weakly to their atomic cores. They delocalize in a solid crystal and form a sp-hybridized conduction band. It can be regarded as quasi free electron gas because the influence of an individual atomic core is marginal [39]. The term “quasi” indicates that the electrons are only free inside the crystal.

Many optical properties of a noble metal in the infrared and partially visible region can be described with the Drude Sommerfeld model for the free electron gas. The electric field of an incident electromagnetic wave is assumed to drive the motion of the valence electrons. Since they are quasi free, they do not feel any restoring force from their ions. The dielectric function is given by the (linear) susceptibility χ_{DS}:

$$\varepsilon = 1 + \chi_{\mathrm{DS}} = 1 - \frac{\omega_{\mathrm{p}}^2}{\omega^2 + i\frac{1}{\tau}\omega} \approx 1 - \frac{\omega_{\mathrm{p}}^2}{\omega^2}. \tag{2.1}$$

Here, ω is the frequency of the electromagnetic wave. The parameter $\omega_{\mathrm{p}} = \sqrt{\frac{ne^2}{\varepsilon_0 m_{\mathrm{eff}}}}$ is called plasma frequency where n is the carrier density and m_{eff} the effective carrier mass. Each electron is assumed to scatter after the time τ by collisions. The approximation in equation (2.1) is valid because $\omega \gg \frac{1}{\tau}$ in the near-infrared and visible region [40].

According to Matthiessen´s rule, the scattering time τ is particularly influenced by collisions with other electrons, phonons or defects. These are assumed to occur independently and determine the electrical conductivity σ:

$$\frac{1}{\tau} = \frac{1}{\tau_{\mathrm{e}}} + \frac{1}{\tau_{\mathrm{ph}}} + \frac{1}{\tau_{\mathrm{def}}} + \cdots = \frac{ne^2}{\sigma m_{\mathrm{eff}}}. \tag{2.2}$$

With the values $n = 5.9{\cdot}10^{22}$ cm^{-3} and $m = 0.99m_{\mathrm{e}}$, the scattering time gives about $\tau =$ 30 fs for bulk gold [39]. When the photon energy is sufficient to excite interband transitions of the metal, which occurs typically in the visible or ultra violet regime, the Drude Sommerfeld model can no longer describe the dielectric properties [40]. An additional susceptibility χ_{IB} which regards the interband transition(s) has to be added: $\chi = \chi_{\mathrm{DS}} + \chi_{\mathrm{IB}}$.

Gold has optical transitions from the 5d to the 6sp band at the X and L points of the Brillouin zone. Respective band gaps are 1.7 and 2.38 eV [41]. However, the transition at the X point does not significantly contribute to the overall optical density because of very low oscillator strength.

Plasmon polaritons

The refractive index $n = \sqrt{1+\chi}$ of metals below the plasma frequency and interband transitions is almost solely imaginary because $\chi_{\mathrm{DS}} < -1$. Therefore, visible and infrared radiation can only penetrate a few nanometres into the crystal. The 1/e-penetration depth is about 30 nm for gold in the visible range [40]. However, when a gold particle has comparable or even smaller dimensions than the penetration depth, the light is not fully absorbed within the particle: Unlike in the bulk material, local dipole moments $\boldsymbol{p}_{\mathrm{ind}}$ are induced at each metal atom by the incident light similar to dielectric materials. If the particle dimensions are much smaller than the wavelength of the incident electromagnetic wave, the spatial dependence $\boldsymbol{p}_{\mathrm{ind}}(\boldsymbol{r}) \sim e^{i\boldsymbol{kr}}$ inside the particle can be neglected [40]. In this so called “quasi-static” regime, the macroscopic polarization of a particle with n induced dipoles per volume gives:

$$\boldsymbol{P} = n\boldsymbol{p}_{\mathrm{ind}} = n\alpha\boldsymbol{E}_{\mathrm{loc}}, \tag{2.3}$$

where α is the electric polarizability. The local field $\boldsymbol{E}_{\mathrm{loc}}$ at each atom is different to the macroscopic field because of the polarization of the material around. As illustrated in Figure 2.1a, the atom is considered to be located in a spherical hollow (Lorentz sphere) inside the particle.

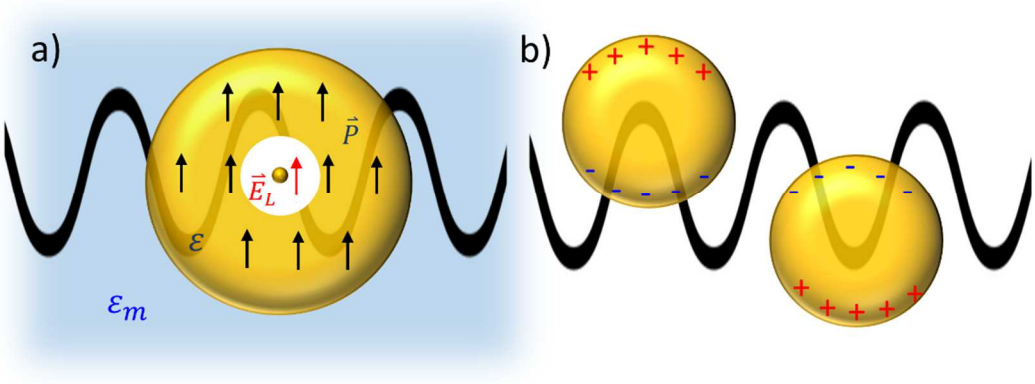

Figure 2.1: Polarizability of small metal spheres a) The polarization of the particle induces an electric field (Lorentz field) at each atom which is assumed to be located in the centre of a hollow. b) Localized surface plasmon resonance: coherent and collective oscillations of conduction band electrons periodically strongly polarize the particle.

The particle itself is embedded in a matrix with the dielectric constant ε_{m}. Since the hollow is filled with vacuum, the macroscopic field inside is $\varepsilon_{\mathrm{m}}\boldsymbol{E}$ with the electric field strength $\boldsymbol{E}$ inside the matrix. A surface charge $\boldsymbol{P}d\boldsymbol{S}$ is induced per surface element $d\boldsymbol{S}$ of the Lorentz sphere, which leads to an additional electric field $\boldsymbol{E}_{\mathrm{L}}$ (depolarization or Lorentz field). Therefore, the local field at the atom inside the hollow gives:

$$\boldsymbol{E}_{\mathrm{loc}} = \varepsilon_{\mathrm{m}}\boldsymbol{E} + \boldsymbol{E}_{\mathrm{L}}. \tag{2.4}$$

The Lorentz field strongly depends on the geometry of the particle. For a sphere, the calculation is rather simple by assuming $\boldsymbol{P}$ to be parallel to the z-axis, so $\boldsymbol{P}d\boldsymbol{S} = P_0 cos\theta dS$. The Lorentz field gives [42]:

$$\boldsymbol{E}_{\mathrm{L}} = \int \boldsymbol{P}d\boldsymbol{S}\frac{1}{4\pi\varepsilon_0}\frac{\hat{\boldsymbol{r}}}{|r|^3} = \int P_0 cos\theta \frac{1}{4\pi\varepsilon_0}\frac{\hat{\boldsymbol{r}}}{|r|^3}dS = \frac{1}{3\varepsilon_0}\boldsymbol{P}. \tag{2.5}$$

Therefore, equation (2.3) can be written as:

$$\boldsymbol{P} = n\alpha \boldsymbol{E}_{\mathrm{loc}} = n\alpha \left(\varepsilon_{\mathrm{m}} \boldsymbol{E} + \frac{1}{3\varepsilon_0} \boldsymbol{P} \right). \tag{2.6}$$

On the other hand, the macroscopic polarization of gold is given by its dielectric constant ε:

$$\boldsymbol{P} = \varepsilon_0 (\varepsilon - \varepsilon_{\mathrm{m}}) \boldsymbol{E}. \tag{2.7}$$

Equalizing equations (2.6) and (2.7), the Clausius-Mossotti relation can be derived which expresses the electric polarizability in terms of the dielectric constant [43]:

$$n\alpha = \frac{3\varepsilon_0 (\varepsilon - \varepsilon_{\mathrm{m}})}{\varepsilon + 2\varepsilon_{\mathrm{m}}}. \tag{2.8}$$

For $\varepsilon + 2\varepsilon_{\mathrm{m}} = 0$, the polarizability takes extraordinarily high values. This condition can be fulfilled for metals because their dielectric function is negative for $\omega < \omega_{\mathrm{p}}$. With the dielectric function of the Drude Sommerfeld model in equation (2.1), the resonance frequency can be determined:

$$\omega_{\mathrm{pl}} = \frac{\omega_{\mathrm{p}}}{\sqrt{1 + 2\varepsilon_{\mathrm{m}}}}. \tag{2.9}$$

This resonance is also called localized surface plasmon resonance: The electron cloud oscillates collectively along the $\boldsymbol{E}$ field of the electromagnetic wave (see Figure 2.1b). Periodic modulations of the electron density strongly polarize the particle. Significant power of the incoming electromagnetic wave dissipates by driving the oscillation. In the quasi-static regime, the extinction of the particle can be expressed by the Rayleigh scattering cross section [40]:

$$\sigma_{\mathrm{ext}}(\omega) = 9 \frac{\omega}{c} \varepsilon_{\mathrm{m}}^{3/2} V \frac{\varepsilon_2(\omega)}{\left(\varepsilon_1(\omega) + 2\varepsilon_{\mathrm{m}}(\omega)\right)^2 + \varepsilon_2(\omega)^2}. \tag{2.10}$$

V is the particle volume with the complex dielectric function $\varepsilon(\omega) = \varepsilon_1(\omega) + i\varepsilon_2(\omega)$ and c the speed of light. With the dielectric function of the Drude Sommerfeld model in equation (2.1), the extinction coefficient can be approximated with a Lorentz profile:

$$\sigma_{\text{ext}}(\omega) \approx \frac{\sigma_0}{\left(\omega - \omega_{\text{pl}}\right)^2 + (1/2\tau)^2}. \tag{2.11}$$

The numerator σ_0 summarizes all constants of equation (2.10). The profile is centred around the localized surface plasmon resonance ω_{pl}. For the sake of simplicity, it will be abbreviated with "plasmon resonance" or "plasmon" in the following work. The full width at half maximum (FWHM) is equivalent to $1/\tau$, which is the damping rate of the electron motion (see detailed discussion in the next section of this subchapter).

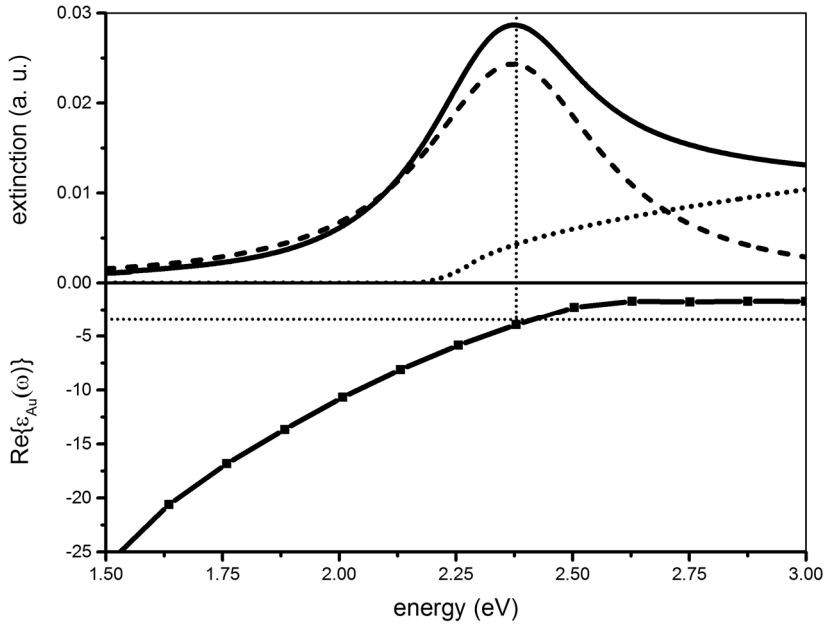

Figure 2.2: Optical behaviour of gold nanospheres Top: Extinction spectrum of colloidal gold spheres (r = 20 nm) in aqueous dispersion with fits for the plasmon resonance (dashed) and the interband absorption (dotted). Bottom: Real part of the dielectric constant for gold (taken from [44]). The plasmon resonance occurs when $\varepsilon_{\text{Au}}(\omega) = -2\varepsilon_{\text{water}}$ is fulfilled.

The top graph of Figure 2.2 shows the extinction spectrum of an aqueous colloidal suspension of 20 nm gold spheres which was measured during the work of this thesis. The plasmon resonance can be clearly observed at 2.4 eV as well as the interband absorption

of gold. From the data of Johnson and Christy [44], the real part of the dielectric function of gold is plotted in the bottom graph. The horizontal line illustrates the condition $-2\varepsilon_{\mathrm{water}} = -3.54$. As expected from equation (2.8), the plasmon resonance is located close to the intersection point where $\mathrm{Re}(\varepsilon_{\mathrm{Au}}(\omega)) = -2\varepsilon_{\mathrm{water}}$.

For larger spheres, the Rayleigh scattering cross section of equation (2.10) is no longer a good approximation for the extinction coefficient, since the phase of the electric field differs inside the particle. Consequently, the quasi-static regime breaks and so-called retarding effects redshift the plasmon resonance. Mie scattering theory can reproduce extinction spectra for arbitrary particle geometries. It is a multipole expansion of the scattered radiation of an incident monochromatic electromagnetic wave [45]. Both the absorption and scattering cross section can be calculated independently. The first multipole order is equivalent to the Rayleigh scattering cross section. It has been shown that Mie scattering accurately reproduces the scattering spectra of different metal particles [46-48].

However, not only the size of a metal particle can change the plasmon resonance but also its shape. Wet chemistry synthesis methods allow various shapes like triangles [49], stars [50], cubes [51] and nanorods [52]. The dielectric properties differ significantly from spherical particles of the respective metal. The geometry determines the Lorentz field in equation (2.4) at each metal atom. For ellipsoidal nanoparticles, the respective local field depends on the polarization $\boldsymbol{E}_i$ of the incident wave along the three principal axes a, b and c. Therefore, plasmon resonances can occur along each of them [53]. For spheroidal particles, the transverse dimensions are identical: $a = b < c$. Such structures will be denoted as gold nanorods in the following thesis. Depending on the polarization vector of the incident electric field, either the transverse or longitudinal plasmon resonance can be excited (sketched in Figure 2.3). The aspect ratio $c{:}\,a$ defines their spectral position: In comparison to a gold sphere, the longitudinal plasmon shifts to lower and the transverse plasmon to higher frequencies with increasing aspect ratio [40].

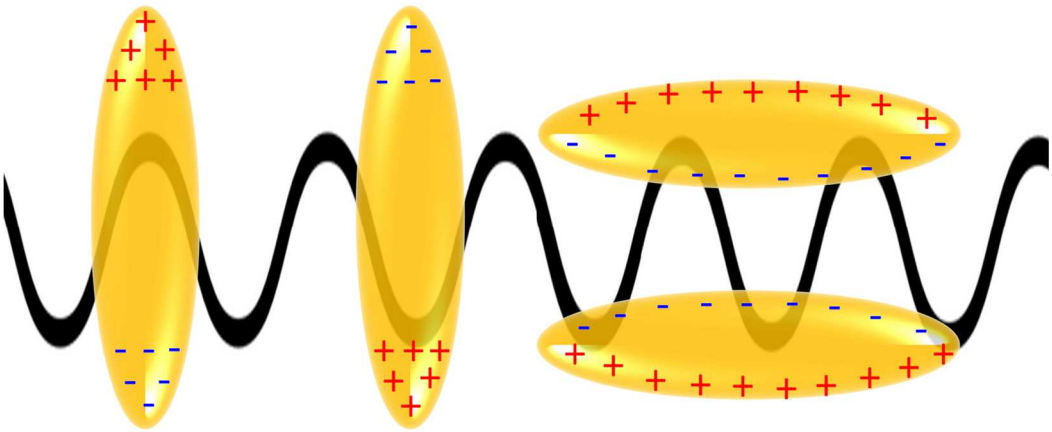

Figure 2.3: Localized surface plasmon resonances in elongated gold nanoparticles Depending on the polarization of the incident electromagnetic wave, longitudinal or transverse plasmon oscillations can be excited. The resonance frequency depends on the aspect ratio.

Damping mechanisms of plasmons in gold nanoparticles

Like every excitation mechanism in matter, plasmons decay radiatively or non-radiatively which is shown in Figure 2.4. The radiative pathway can be described classically by a Hertz dipole: The accelerated conduction band electrons emit radiation which can be observed as coherently scattered light from the particle [54]. Using an extension of the Drude Sommerfeld model, the radiative decay rate is found to be proportional to the volume of the particle [46]. Relaxation by fluorescence is very weak in comparison to coherent scattering [40].

The non-radiative pathway is the dissipation of the excitation energy into electron-hole pairs (Landau damping). Depending on the spectral position of the plasmon resonance, either an electron from the conduction band or from the lower 5d-band is excited above the Fermi level (“hot electron”). The relaxation of these hot carriers occurs by heating the particle and its environment [55].

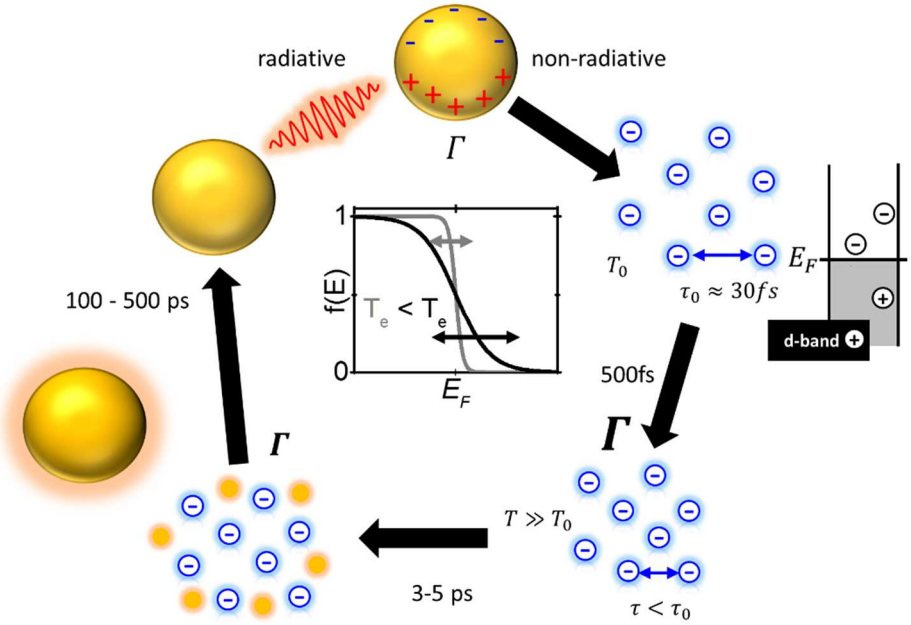

Figure 2.4: Damping mechanisms of plasmon resonances The radiative decay channel is the relaxation by emission of photons. The homogenous linewidth Γ enhances during the non-radiative decay because the energy is converted to heat. First, the electron gas heats up which increases the electron-electron scattering rate. The electron gas thermalized with the crystal lattice and finally the entire particle with its environment.

Plasmons are rapidly damped within few femtoseconds due to the high electron collision rate $\frac{1}{\tau}$. Equation (2.11) predicts a linewidth equal to $\frac{\hbar}{\tau}$ of the plasmon resonance. In general, the linewidth of isolated resonances is called homogenous linewidth and is inverse proportional to the dephasing time T_2:

$$\Gamma = \frac{2\hbar}{T_2}. \tag{2.12}$$

The dephasing time describes the decay of the polarization associated with the respective excitation (see 2.2.2). Typical dephasing times of plasmon resonances in noble metal particles lie in the range between 6 fs and 18 fs for gold nanorods [46]. If the plasmon resonance overlaps with interband transitions, the dephasing time decreases due to an increased interband damping rate.

Important scattering processes for individual electrons are considered by the Matthiessen´s rule, equation (2.2). The interaction with surface defects τ_{def} strongly depends on the particle size. It becomes important when the dimensions decrease significantly below the mean free path length of electrons. With the Fermi velocity v_F, the latter can be approximated to $l \approx v_F \tau = 41$ nm [40]. Gold nanorods with the dimensions of 34 x 18 nm are the smallest particles which were used in this thesis. They are still too large that surface scattering dominates.

The interaction with other electrons and phonons is related to the temperature of the electron gas and the lattice, respectively. The non-radiative decay of a plasmon polarization strongly influences both temperatures as illustrated in Figure 2.4. Within the first picosecond, the “hot electron” dissipates its excess energy to the electron gas. Therefore, the corresponding temperature increases up to 4000 K [56]. This results in a great misbalance between the internal energy of electron and phonon gas, so a subsequent thermalisation occurs within few picoseconds.

The enormous rise of the electron gas temperature decreases the average electron-electron scattering time $\bar{\tau}_{e-e}$ to about 10 fs. A model to understand this process is illustrated in the central plot of Figure 2.4: The Fermi-Dirac statistic smears out for the hot electron gas. Since the number of populated initial und unpopulated final states increases in the vicinity of the Fermi level, the energy range of scattering events enhances. The average electron-electron scattering time in the hot electron gas is comparable to the total dephasing time of plasmons in the “cold” gold nanorod. Therefore, the dephasing rate is significantly enhanced and the homogenous linewidth of the plasmon resonance increases. This can be observed with femtosecond transient absorption spectroscopy [56].

In this thesis, I monitored the dephasing of plasmons in gold nanorods which were strongly coupled to J-aggregated dye molecules. Femtosecond transient absorption spectroscopy was used to study the respective influences on the coupled resonances. With these experiments, I could show that the coupled resonances have tuneable plasmonic signatures.

2.1.2 Optical and morphological properties of J-aggregated dye molecules

In the years 1936 and 1937, E. E. Jelly and G. Scheibe independently discovered that the cyanine dye *pseudoisocyanin chloride* changes its optical properties when its concentration exceeds 10^{-3} M in aqueous solution [57, 58]. A new and redshifted absorption band appeared. The addition of sodium chloride led to a similar effect: The absorption band sharpened and its extinction coefficient increased significantly [59]. Furthermore, remarkable photoluminescence occured with an extremely small Stokes shift of only 15 meV. Both Scheibe and Jelly found that the appearance of this "mysterious" absorption band was reversible by heating or cooling the solution.

Scheibe explained the experimental findings on the basis of a supramolecular self-assembly of the dye molecules. Today, various dyes are known which show the described behaviour [60, 61]. The process is denoted as "Scheibe-" or "J-aggregation" (J for E. E. Jelly). The opposite effect where molecular aggregates have a blueshifted absorption band is denoted as H-aggregation (H for hypsocromic shift). In contrast to J-aggregates, these do not show fluorescence.

Up to now, no theory could comprehensively describe all optical phenomena of J-aggregates. Even though the coupled dipole model of Kasha [62] only applies for two dipoles, it can help to understand the fundamental principles. The theory describes the band alignment of a dimer with two identical dipole moments which are arranged at an angle θ towards the dipole axis (see Figure 2.5). Due to van-der Waals interaction, the transition energy of both monomers gets reduced in the dimer by ΔE_{VDW}. In addition to this, the dipole-dipole coupling splits the dimer transition into two bands separated by the interaction energy ΔE. For $\theta < 54.7°$, the lower band fulfils the selection rules for optical transitions and would therefore correspond to the J-band. For $\theta > 54.7°$, only the higher band is dipole allowed resembling the H-band.

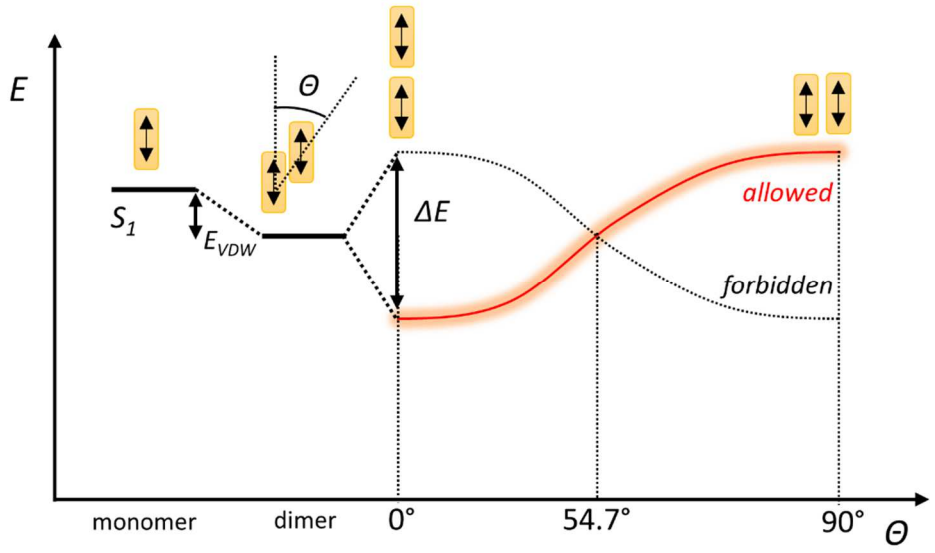

Figure 2.5: Dipole coupling Dimer aggregation with different arrangements according to Kasha [62]. The angle between both dipoles determines the coupling energy *ΔE*. Only one transition is dipole allowed (red). This is a simplified model for J- and H-aggregation.

Although J-aggregates have been thoroughly investigated within the past 80 years, their morphology and the arrangement of the dye monomers within the aggregate have never been cleared. Initially, Scheibe suggested a “coin pile” structure where the flat cyanin molecules staple along the aggregate axis [63]. Additionally, Förster proposed that that the dipole moments could be helically twisted around the axis [64]. Other experimental works suggested a brickwork or ladder-like arrangement [65]. Even crystalline or rod-like morphologies have been discussed [66]. Nowadays, the scientific community considers that the arrangement of the monomers is not unambiguous but rather dependent on the experimental parameters [67].

Efforts have been done to describe the optical excitations of J-aggregated dyes. Like in any other molecular system, an electron from the highest occupied molecular orbital (HOMO) is excited to the lowest unoccupied molecular orbital (LUMO) after the absorption of a photon. The electron vacancy in the HOMO (denoted as hole) together with the electron in the LUMO is termed as exciton. For a detailed discussion of excitons in semiconductors see 2.2.1. It could be shown that an exciton inside the aggregate is delocalized over many monomer units and therefore gains an extraordinarily high dipole

moment. For the dye *pseudoisocyanin chloride*, which was initially used by Scheibe and Jelly, a coherence length of the exciton between 60 and 100 monomer units [68] was found.

In this thesis the cyanine dye *5,5',6,6'-Tetrachloro-1,1',3,3'-tetraethyl-imidacarbocyanine iodide* was used to assemble J-aggregates. Its chemical structure is shown in Figure 2.6a [69]. Like all cyanine compounds, it consists of two heterocyclic rings. One contains a quaternary ammonium cation which acts as an electron acceptor. The other one has two tertiary amino groups acting as electron donor. The described "push-pull" arrangement strongly polarizes the conjugated π system of the polyene bridge between both rings. Therefore, the monomer already absorbs at 500 nm (2.5 eV) even though the π system of the polyene chain consists of only five carbon atoms. Upon addition of an ammonium salt, the sharp J-band appears at 590nm (2.1 eV) which is extensively discussed in the analysis of the experimental results (see Figure 4.1b).

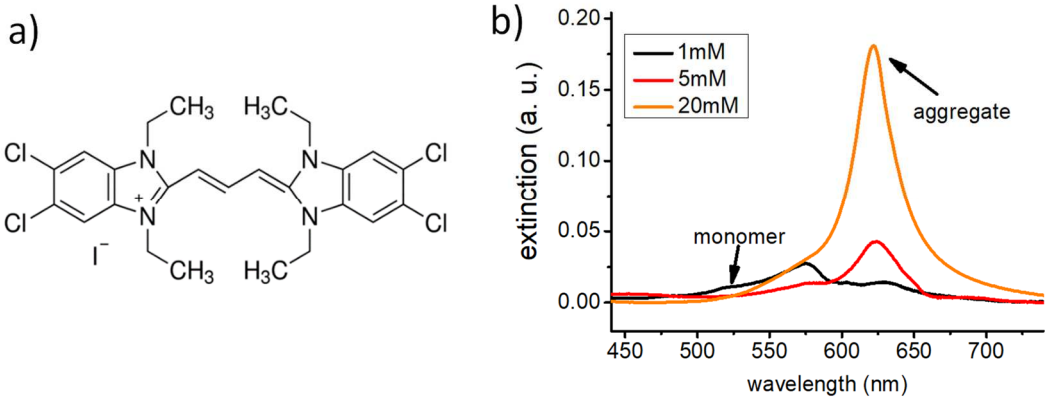

Figure 2.6: J-aggregation a) Chemical structure [69] of the cyanine dye *5,5',6,6'-Tetrachloro-1,1',3,3'-tetraethyl-imidacarbocyanine iodide* which was used in this work. b) Extinction spectra for similar dye upon aggregation.

The influence of J-aggregation on the extinction spectrum can be seen in Figure 2.6b for a very similar dye: Upon addition of sodium chloride, the J-band forms at 630 nm in addition to the transition band of the free monomers at 520-570 nm. The absorption coefficient of the band increases and the linewidth reduces with increasing salt concentration. The characteristic narrowing of the linewidth is attributed to the delocalization of the exciton over several monomer units. This averages over local

inhomogeneities. Similar to motional narrowing for spins in a non-static environment [70], the linewidth decreases proportional to $N^{-\frac{1}{2}}$ according to the central limit theorem, where N is the number of monomer units [71].

2.1.3 Strong light-matter interaction

When an emitter is placed in an electromagnetic resonator such as a cavity (see Figure 2.7a), the electromagnetic field interacts with its dipole moment. In case of weak coupling, the spontaneous emission rates are influenced by vacuum fluctuations. Depending on whether the emitter is in or off resonance with the electromagnetic mode, the emission is enhanced [72, 73] or suppressed [74]. The enhancement is also known as "Purcell effect".

Mode-emitter hybridization

If the interaction gets stronger, optical modes "mix" with the eigenstates of the emitter. Two new states at different energy are formed. The simplest model to describe these phenomena is to regard the emitter as a two-state quantum system. The ground state $|g\rangle$ should then have the energy $-E_{\mathrm{ex}}/2$, whereas the excited state $|e\rangle$ has $E_{\mathrm{ex}}/2$. The transition frequency is $\omega_{\mathrm{ex}} = \frac{E_{\mathrm{ex}}}{\hbar}$. If an electromagnetic mode $|n\rangle$ inside the cavity is comprised of n photons with the frequency ω_{c}, the system can be described with product states $\{|e,n\rangle, |g,n\rangle\}$ [75].

Due to the dipole moment $\boldsymbol{\mu}$ of the emitter, the electric field $\boldsymbol{E}$ inside the resonator can interact and cause a perturbation. The Hamiltonian of the interaction is a scalar product of the respective operators: $\hat{H}_{\mathrm{int}} = \hat{\boldsymbol{\mu}}\hat{\boldsymbol{E}}$ [76]. To determine its matrix elements in the basis of the emitter and the cavity, the rotating wave approximation has to be applied: Since

$$\hat{\boldsymbol{\mu}}(t) \sim (e^{i\omega_{\mathrm{ex}}t} + e^{-i\omega_{\mathrm{ex}}t}) \text{ and } \hat{\boldsymbol{E}}(t) \sim (e^{i\omega_{\mathrm{c}}t} + e^{-i\omega_{\mathrm{c}}t}), \tag{2.13}$$

the product of both has terms oscillating with $\omega_{\mathrm{ex}} + \omega_{\mathrm{c}}$ and $\omega_{\mathrm{ex}} - \omega_{\mathrm{c}}$. If the spectral detuning between the cavity mode and the emitter

$$\delta = \omega_{\mathrm{ex}} - \omega_{\mathrm{c}}, \tag{2.14}$$

is small, oscillations of $\hat{H}_{\mathrm{int}}$ with the sum frequency are on a much faster time scale. They therefore average to zero within an oscillation period of the difference frequency [77].

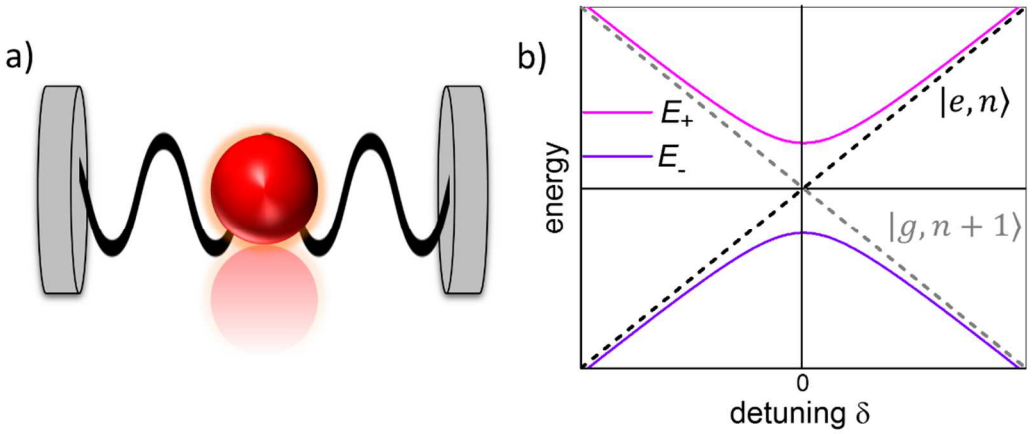

Figure 2.7: Strong coupling versus weak coupling a) An emitter is placed in an electromagnetic resonator. In case of strong coupling, hybrid states between the mode and the emitter are formed. b) These new states (solid curves) spectrally differ from the resonator mode and the transition of the emitter (dotted lines). When the spectral detuning δ between resonator and emitter is varied, both would cross at δ = 0 where they have the same energy (weak coupling regime). In the strong coupling regime, the hybrid states are always separated by a spectral gap (anticrossing).

The total Hamiltonian can then be represented with the base vectors $\{|e,n\rangle, |g,n+1\rangle\}$. They account only single photon absorption processes, i.e. the emitter in the ground state annihilates one photon and gets excited or relaxes back to the ground state by emitting one photon. Their eigenenergies are given by $\hbar(\frac{\omega_{\mathrm{ex}}}{2} + n\omega_{\mathrm{c}})$ and $\hbar(-\frac{\omega_{\mathrm{ex}}}{2} + (n+1)\omega_{\mathrm{c}})$, respectively. The Hamiltonian of the system can then be written as [78]

$$\hat{H} = \hat{H}_0 + \hat{H}_{\mathrm{int}} = \hbar \begin{pmatrix} (n+1)\omega_{\mathrm{c}} - \dfrac{\omega_{\mathrm{ex}}}{2} & \hbar\boldsymbol{\mu}\boldsymbol{E}\sqrt{n+1} \\ \hbar\boldsymbol{\mu}\boldsymbol{E}\sqrt{n+1} & nE_{\mathrm{c}} + \dfrac{\omega_{\mathrm{ex}}}{2} \end{pmatrix}, \tag{2.15}$$

which is also known as the Jaynes-Cummings Hamiltonian.

Rabi splitting and Rabi oscillations

The coupling constant in the off-diagonal elements is also expressed with the n-photon Rabi frequency Ω_n:

$$\frac{\Omega_n}{2} = \boldsymbol{\mu E}\sqrt{n+1}. \tag{2.16}$$

The eigenergies of the Hamiltonian in (2.15) are then:

$$E_{\pm} = \hbar(n+\frac{1}{2})\omega_c \pm \frac{\hbar}{2}\sqrt{\delta^2+\Omega_n^2}. \tag{2.17}$$

In Figure 2.7b, $E_{\pm}$ and the eigenergies of the system without any interaction are plotted versus the detuning δ. If no interaction is involved, the states $|g,n+1\rangle$ and $|e,n\rangle$ would energetically cross at $\delta = 0$ which means that mode and emitter have the same energy. However, the coupled states show a spectral repulsion from the uncoupled system: Instead of crossing at $\delta = 0$, they are separated by a spectral gap which is called "Rabi splitting". Its value can be easily calculated from equation (2.17):

$$E_+(\delta = 0) - E_-(\delta = 0) = \hbar\Omega_n. \tag{2.18}$$

This so-called "anticrossing" behaviour is typical for strongly coupled systems. If the detuning is large, the coupled states approach the energies of the uncoupled system [75]. The eigenvectors of $\hat{H}$ to the eigenenergies $E_{\pm}$ are:

$$\begin{pmatrix}|+\rangle\\|-\rangle\end{pmatrix} = \begin{pmatrix}\cos\frac{\alpha}{2} & \sin\frac{\alpha}{2}\\ -\sin\frac{\alpha}{2} & \cos\frac{\alpha}{2}\end{pmatrix}\begin{pmatrix}|e,n\rangle\\|g,n+1\rangle\end{pmatrix}, \tag{2.19}$$

with $\tan\alpha = \frac{\Omega_n}{\delta}$ and $\alpha \geq 0$ [78]. They are therefore a superposition of the excited state $|e,n\rangle$ and the ground state $|g,n+1\rangle$. Ground and excited state can be distinguished as different states in the absence of mutual coupling, whereas hybridization occurs in the strong coupling regime. In case of resonant coupling conditions (i. e. $\delta = 0$), the hybrid states are equally comprising both uncoupled states:

$$|\pm\rangle = \frac{1}{\sqrt{2}}|e,n\rangle \pm \frac{1}{\sqrt{2}}|g,n+1\rangle. \tag{2.20}$$

In presence of detuning, the superposition gets asymmetric, because one coefficient increases whereas the other one decreases which is explicitly shown for $|\langle e,n|\pm\rangle|^2$ in Figure 2.8a. The respective state vectors approach to the bare subsystems, likewise the eigenenergies $E_\pm$ (see Figure 2.7b).

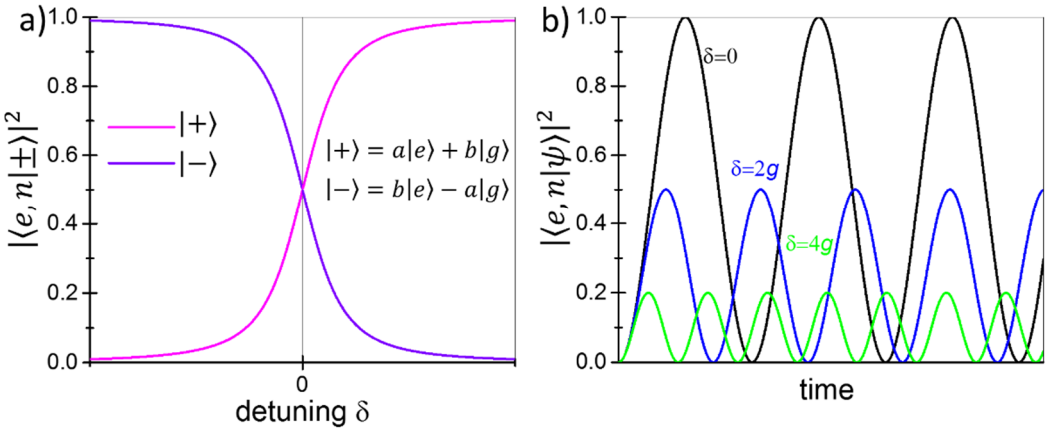

Figure 2.8: Strong coupling and spectral detuning a) The eigenstates *|+⟩* and *|-⟩* of a strongly coupled system can be expressed as a linear combination of the excited emitter *|e,n⟩* and the resonator mode *|g,n+1⟩* according to equation (2.19). The squared coefficient *⟨e,n|±⟩* is plotted versus the detuning. b) In the strong coupling regime, the emitter periodically oscillates between ground and excited state (Rabi oscillations). The amplitude and oscillation period are maximal when the cavity mode matches the transition resonance ($\delta = 0$).

The time evolution of an arbitrary state $|\psi(t)\rangle$ can be calculated by solving the time dependent Schrödinger equation. When the system is initially in the ground state the occupation probabilities are [79]:

$$\begin{pmatrix} |\langle e,n|\psi\rangle|^2 \\ |\langle g,n+1|\psi\rangle|^2 \end{pmatrix} = \begin{pmatrix} \frac{\Omega_n^2}{\delta^2+\Omega_n^2}\sin^2\left(\sqrt{\delta^2+\Omega_n^2}\cdot t\right) \\ 1-\frac{\Omega_n^2}{\delta^2+\Omega_n^2}\sin^2\left(\sqrt{\delta^2+\Omega_n^2}\cdot t\right) \end{pmatrix}. \tag{2.21}$$

The system oscillates between the ground and the excited state while emitting and reabsorbing a photon. Within these “Rabi oscillations”, the energy is coherently

exchanged between the cavity and the emitter, which is plotted in Figure 2.8b for different spectral detunings. When the cavity mode is in resonance with the transition, full population inversion can be periodically achieved, i. e. the probability of the exited state is 1. When the detuning gets larger, the frequency of the Rabi oscillations enhances and the amplitude reduces.

According to equations (2.16) and (2.18), the Rabi splitting is proportional to the electric field and the dipole moment. In this thesis, I worked with a material system where both quantities are very high: As described in the two previous sections, the electric field in the vicinity of metal particles is extremely high when a localized surface plasmon resonance is excited and J-aggregates have an enormous dipole moment. Therefore, the combination of both compounds can exhibit enormous Rabi splitting when the electric field of the plasmon resonance couples to the dipole of J-aggregated dye molecules [80]. I analysed the effects of strong coupling on the nonlinear optical behaviour of the respective hybrid states. The experimental results will be shown in chapter four.

2.2 Dephasing of excitons in semiconductor nanoplatelets

The optical properties of semiconductor nanocrystals strongly depend on their geometry. Spatial confinement can directly affect the electronic properties which is also known as "quantum confinement". The first part of this chapter introduces the fundamentals of low-dimensional semiconductors. The role of excitons and their spectral linewidth are thoroughly discussed. The second part of this chapter focuses on the coherent dynamics of optical excitations in matter according to the optical Bloch equations. Loss mechanisms of microscopic and macroscopic polarizations by dephasing and free induction decay are explained. Furthermore the principle of photon echoes to measure the dephasing time/homogenous linewidth in an ensemble of absorbers is presented. The last section introduces briefly the physics of quantum beats.

This chapter introduces the background to my second project within the scope of this thesis. I measured the dephasing time and the binding energy of excitons in methylammoium lead halide perovskite nanocrystals with degenerate four-wave mixing. Both quantities cannot be determined with linear optical spectroscopy because they are shaded by inhomogeneities within a macroscopic sample. The latter problem is discussed in detail in this section.

2.2.1 Electronic properties of semiconductor crystals

Three-dimensional versus two-dimensional particles

The dimensionality of a semiconductor crystal strongly influences its optical properties when one or more dimensions significantly decrease about ten nanometres. At this size, the spatial confinement affects the wavefunctions of the carriers in the material. In the following section, the consequences of dimensionality are discussed for three and two-dimensional semiconductor crystals.

Valence and conduction bands of semiconductors can be regarded as electron gas. Close to the band gap E_g, the energy of both electron and hole can be approximated with a parabolic dispersion relation:

$$E^{\mathrm{e/h}} = \frac{1}{2}E_\mathrm{g} + \frac{1}{2m_{\mathrm{e/h}}}\hbar^2\boldsymbol{k}^2, \tag{2.22}$$

where $m_{e/h}$ denotes the effective carrier masses of electron and hole, respectively [39]. In case of a direct semiconductor, photons with an energy $\hbar\omega \geq E_\mathrm{g}$ can be absorbed. The absorption coefficient is proportional to the density of states in the interval of the respective photon energy. For a three dimensional crystal, the density of states is given by [39]:

$$D^{\mathrm{3D}}(E) = \frac{(2m)^{3/2}}{2\pi^2\hbar^3}\sqrt{E - E_\mathrm{g}}, \tag{2.23}$$

where $m^{-1} = m_\mathrm{e}^{-1} + m_\mathrm{h}^{-1}$ is the reduced carrier mass. If the size of the semiconductor crystal is confined along one dimension, the carriers experience a potential jump outside the crystal boundaries. Since the wavefunctions of both electron and hole have to be continuous, the Schrödinger equation can only be solved for a discrete energy spectrum. If the potential outside is infinite, the momentum of electron and hole along the confined dimension (e. g. z-direction) changes from continuous values to $k_\mathrm{z}^{\mathrm{e/h}} \rightarrow n_\mathrm{z}^{\mathrm{e/h}}\frac{\pi}{L_\mathrm{z}}$. Here, n_z is a positive integer number and L_z the length of the crystal in z-direction [81]. For optical

transitions $n_z^e = n_z^h$ is valid, since the photon momentum is negligible [82]. The transition energies are:

$$E(n_z) = E_g + \frac{h^2}{8mL_z^2} n_z^2. \tag{2.24}$$

The density of states for electrons and holes in two dimensions is constant for each transition:

$$D^{2D}(E) = \frac{m}{\pi\hbar^2} \sum_{n_z} \theta(E - E_g - E(n_z)), \tag{2.25}$$

where θ denotes the Heaviside step function.

The role of excitons in semiconductors

So far, the Coulomb attraction between electron and hole was not considered. Introducing the Coulomb potential into the Hamiltonian leads to the Wannier equation [39, 83]:

$$-\left(\frac{\hbar^2}{2m}\Delta + \frac{e^2}{4\pi\varepsilon\varepsilon_0 r}\right)\Phi_n(\boldsymbol{r}) = E_n\Phi_n(\boldsymbol{r}). \tag{2.26}$$

The static dielectric constant of the material is ε and r the distance between electron and hole. Φ_n is the radial part of the wavefunction. Since the structure of equation (2.26) is equivalent to the Schrödinger equation of the hydrogen atom, the angular part is solved by spherical harmonics. Figure 2.9a schemes the eigenergies of equation (2.26) in dependence of the centre of mass wave vector $\boldsymbol{K} = \boldsymbol{k}_e + \boldsymbol{k}_h$ for electron and hole. In addition to free carriers in the continuum of states for $E \geq E_g$ or $E \geq E(n_z)$, bound electron-hole pairs (analogous to atomic hydrogen) with lower discrete energy E_n are formed. These states are called excitons. For three dimensional crystals, their total energy is given by:

$$E_n = E_g - \frac{R^*}{n^2} + \frac{\hbar^2 \boldsymbol{K}^2}{2(m_e + m_h)}. \tag{2.27}$$

The constant $R^* = \frac{e^4 m}{8\varepsilon^2 \varepsilon_0^2 h^2}$ can be understood equivalent to the Rydberg constant of the hydrogen atom with a different effective mass and dielectric constant. Since the momentum of the photon $k = \frac{E}{c}$ is nearly zero for optical transitions, excitations can only occur at $\boldsymbol{K} \approx 0$ [82].

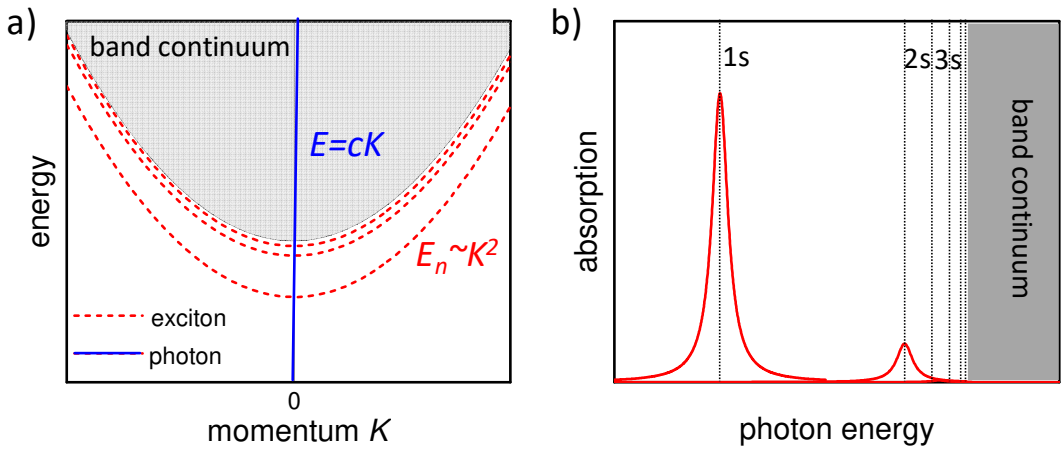

Figure 2.9: Excitons in semiconductors a) Dispersion relation of excitons (red). *K* denotes the centre of mass momentum. The dispersion of a photon (blue) is nearly vertical and can only excite excitons with *K*≈0. b) Excitons appear as distinct resonances in the absorption spectrum. Their energy is lower than the band continuum, where the absorbed light creates free charges. The oscillator strength decreases for excitons at higher energy.

Like atomic hydrogen, each state with the energy E_n is n^2-times degenerated including orbital and magnetic quantum numbers of the corresponding wavefunction [82]. Due to the attractive Coulomb interaction, electron and hole are bound with the exciton binding energy $E_B = \frac{R^*}{n^2}$. This energy has to be applied to create free charges (in the valence and conduction band), equivalent to the ionization energies of hydrogen. By contrast to the Rydberg constant of the hydrogen atom which is 13.6 eV, the constant R^* and the exciton binding energies are typically in the range of few up to several hundreds of meV. The reasons are the screening of the Coulomb force by the material (expressed by its static dielectric constant $\varepsilon > 1$) and the influence of the crystal potential on the carriers. Due

to the latter, the effective masses are lower than the mass m_0 for the free electron in vacuum. For the same reasons, the corresponding exciton Bohr radius $a_{\mathrm{B}} = \frac{4\pi\varepsilon\varepsilon_0\hbar^2}{me^2}$ can be up to several nanometres, in comparison to 0.5 Å for the hydrogen atom.

Absorption of semiconductor crystals

Excitons appear as a spectrum of discrete resonances in an optical absorption spectrum (see Figure 2.9b) at lower energy than the onset of interband transitions. The absorption spectrum of a semiconductor can be described with the Elliott formula [83]. It regards both the generation of excitons and free charges in the continuum by photons. The absorption coefficient is given by:

$$\alpha(E) = \sum_n \mathrm{Im}\left(\frac{f_n}{E_n - E - i\hbar\frac{\Gamma_n}{2}}\right) + \alpha_{\mathrm{cont}}(E). \tag{2.28}$$

Here, f_n and Γ_n are the oscillator strength and homogenous linewidth of each exciton resonance. The oscillator strength is proportional to the probability of finding electron and hole in the same unit volume, i. e. with distance zero: $f_n \sim |\Phi_n(r=0)|^2$. In three dimensions, the square of the radial wave function $|\Phi_n(0)|^2$ is proportional to $\frac{1}{n^3}$ [83]. Therefore, excitons with higher n appear significantly weaker in the absorption spectrum which is schemed in Figure 2.9b. In reality, only the exciton with $n = 1$ can be usually observed as a distinct peak in the absorption spectrum. Therefore, the 1s exciton (s for the only possible angular momentum quantum number) is of particular interest in the discussion of the optical behaviour of semiconductors. If the crystal dimensions are comparable or smaller than the Bohr radius, $|\Phi_n(0)|^2$ enhances because the probability of finding electron and hole at the same place increases. The exciton is “squeezed” which means that the spatial confinement of the crystal influences the distance of electron and hole [82]. Consequently, the absorption coefficient of excitonic transitions increases. If the crystal is surrounded by a medium with a lower dielectric constant (like a transparent matrix or air), the screening of the Coulomb interaction is weaker and the exciton binding energy $\frac{R^*}{n^2}$ gets higher. For a two-dimensional crystal, the excitonic energy levels are given

by $E_{n,n_z}^{2D} = E(n_z) - \frac{R^*}{(n-\frac{1}{2})^2}$ [84]. Consequently, the exciton binding energy of the 1s exciton in 2D is four times the one in 3D under negligence of the just described screening effects: $E_B^{2D} = 4E_B^{3D}$.

The absorption behaviour of the continuum for $E \geq E_g, E(n_z)$ is described by $\alpha_{\mathrm{cont}}(E) \sim D(E)|\Phi_E(0)|^2$ in the Elliott formula (2.28). $D(E)$ is the density of states given in equations (2.23) and (2.25) for the respective particle dimension. The correlation enhancement factor $|\Phi_E(0)|^2$ differs significantly from one only at the continuum onset.

Inhomogeneous broadening

Figure 2.10a shows schematically the absorption spectra of a three- and a two-dimensional semiconductor crystal. The solid curves plot the absorption of the continuum of states, i. e. they are proportional to the respective density of states. In case of three crystal dimensions, it is a square root and in case of two dimensions a constant function which follows from equations (2.23) and (2.25) (the correlation enhancement factor is neglected). The onset of the continuum is equal to the band gap in three dimensions. For two-dimensional crystals, the onset is blue shifted by the confinement energy which can be seen in equation (2.24). At lower energy, excitons appear as Lorentz shaped resonances. They are separated from the continuum onset by the exciton binding energy E_{B}. As discussed above, the binding energy increases for two dimensional crystals. Furthermore, the oscillator strength is higher due to the confinement of electron and hole. However, the scheme only shows single absorbers like a single nanocrystal. A real sample like a colloidal dispersion or a film usually comprises several absorption centres. Due to fluctuations of the environment and deviations in the crystal shape, the transition energy of each absorber slightly differs. These so-called inhomogeneous effects have significant consequences on the respective absorption spectrum [85] and are exemplary sketched in Figure 2.10b for two-dimensional crystals:

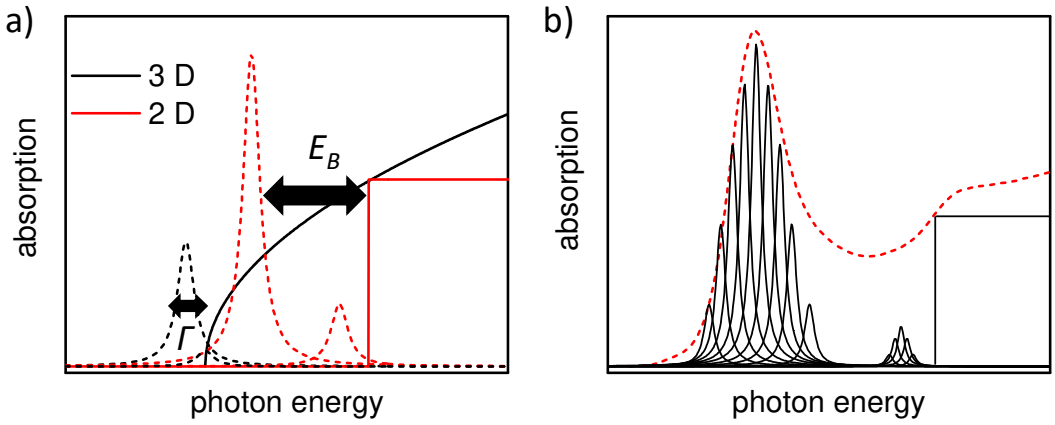

Figure 2.10: Absorption of semiconductors a) Absorption of three- (black) and two-dimensional (red) single crystals. The dashed curves represent the exciton resonances with binding energy E_B and homogenous linewidth Γ. b) Absorption spectrum of an ensemble of different two-dimensional crystals (dashed red curve). Since the spectrum is comprised by various single absorbers at slightly different energies (black), the exciton resonance broadens (inhomogeneous broadening).

Since the resonance energy of each exciton (black solid curves) varies statistically, the linewidth of the ensemble (dashed red graph) increases. This is also called “inhomogeneous broadening”. By contrast to this, the FWHM value of each single exciton resonance is called “homogenous linewidth”. Obviously, the homogenous linewidth gets shaded in the absorption spectrum of an ensemble of particles. In addition to this, the exciton binding energy can no longer be determined as the difference between the continuum onset and the exciton peak like in case of single particles (shown in Figure 2.10a). Because of the inhomogeneous broadening, no sharp onset of the continuum can be observed in the absorption spectrum of the multi-particle system (see dashed red graph in Figure 2.10b). This makes any estimation of the exciton binding energy unreliable.

The homogenous linewidth and the binding energy of excitons can be determined from the absorption/emission of single excitons [86, 87]. However, such approaches are not suitable for every sample since they require single particle resolution. There is an experimental technique which allows the determination of both in an ensemble of particles which will be introduced in the next section.

2.2.2 Dephasing of optical excitations in matter

The homogenous linewidth Γ of an optical transition, like an exciton in a semiconductor, is inversely proportional to the dephasing time T_2 by $\Gamma = \frac{2\hbar}{T_2}$. As already described in the introductory chapter, the coherence of a quantum mechanical state decays with the dephasing time. This will be thoroughly regarded for optical excitations in the following.

Optical Bloch equations

When a material interacts with an oscillating electromagnetic field $\boldsymbol{E}(t) = \boldsymbol{E}_0 \cos \omega t$, the dynamics of the respective absorbers (atoms, molecules, semiconductors,..) can be described by the optical Bloch equations [88]. Each absorber is regarded as a two-state quantum system in the dipole approximation, i. e. the Hamiltonian is given by: $H = H_0 + \hat{\boldsymbol{\mu}}\boldsymbol{E}$.

The dipole moment between ground and excited state along the projection of the electric field is denoted as μ_{12}. A macroscopic sample with $n_1(t)$ atoms per unit volume in the ground state and $n_2(t)$ atoms in the excited state at time t is considered. The dynamics of this sample can be described by defining the Bloch-vector:

$$\boldsymbol{B} = \begin{pmatrix} B_x \\ B_y \\ B_z \end{pmatrix} := \frac{1}{|\mu_{12}| n_0} \begin{pmatrix} \mathrm{Re}(\boldsymbol{P}) \\ -\mathrm{Im}(\boldsymbol{P}) \\ |\mu_{12}| \Delta n \end{pmatrix}, \tag{2.29}$$

with the complex polarization $\boldsymbol{P}$ of the sample, the number of atoms per unit volume $n_0 = n_1(t) + n_2(t) = const$ and the population inversion $\Delta n(t) = n_2(t) - n_1(t)$. Due to $|\boldsymbol{P}|^2 = |\mu_{12}|^2 n_0^2 - \Delta n^2$ [89], the Bloch-vector can be normalized to unity. The time-dependent Schrödinger equation gives the temporal evolution of the Bloch-vector in the rotating frame of the electric field [90]:

$$\frac{d}{dt}\boldsymbol{B} := \begin{pmatrix} -\Omega_R \\ 0 \\ -\delta \end{pmatrix} \times \boldsymbol{B} - \begin{pmatrix} B_x/T_2 \\ B_y/T_2 \\ (B_z + B_z^0)/T_1 \end{pmatrix}. \tag{2.30}$$

Here, $\Omega_{\mathrm{R}} = |\boldsymbol{\mu}_{12}||\boldsymbol{E}|$ is the Rabi frequency and $\delta = \omega - \omega_{12}$ the detuning between the frequency of the electromagnetic wave and the transition resonance ω_{12}. B_z^0 denotes the equilibrium value of the population inversion without any external electromagnetic field. The equation system (2.30) is known as optical Bloch equations. They describe an inverse precession of the Bloch vector around $\begin{pmatrix} \Omega_{\mathrm{R}} \\ 0 \\ \delta \end{pmatrix}$, where the polarization decays with the dephasing time T_2 and the population inversion with T_1.

If the electromagnetic field is in resonance with the transition (i. e. $\delta = 0$) and the sample is initially in the ground state, the dynamics of the Bloch vector are $\boldsymbol{B} = \begin{pmatrix} 0 \\ \sin \Omega_{\mathrm{R}} T \\ \cos \Omega_{\mathrm{R}} T \end{pmatrix}$. Here, the damping term of equation (2.30) was neglected since the time interval T of the exposure of the electric field is considered to be much shorter like in case of short light pulses. Maximum polarization can be achieved for a pulse duration $\Omega_{\mathrm{R}} T = \frac{\pi}{2}$ ("$\frac{\pi}{2}$ – pulse"). After the pulse, the Bloch vector is parallel to the y-axis, meaning that all microscopic polarizations constructively interfere [91].

Dephasing of optical excitations

The dephasing time T_2 and the population recombination T_1 are related to each other by:

$$\frac{1}{T_2} = \frac{1}{2T_1} + \frac{1}{T^*}. \tag{2.31}$$

T^* is called "pure dephasing time" [92] and is explained in the following: Figure 2.11a shows schematically the polarization of a group of six different excitations. Each ellipse represents one absorber, i. e. a single exciton, atom, molecule, etc. Since each single optical excitation behaves like an oscillating dipole, the blue/red colour denote an excess of negative/positive charge. Initially, all excitations have the same phase and the polarization of the microscopic volume which contains this six different absorbers is maximal. The dipoles oscillate with the respective transition frequency. The polarization of the volume can be diminished after excitation by two different processes.

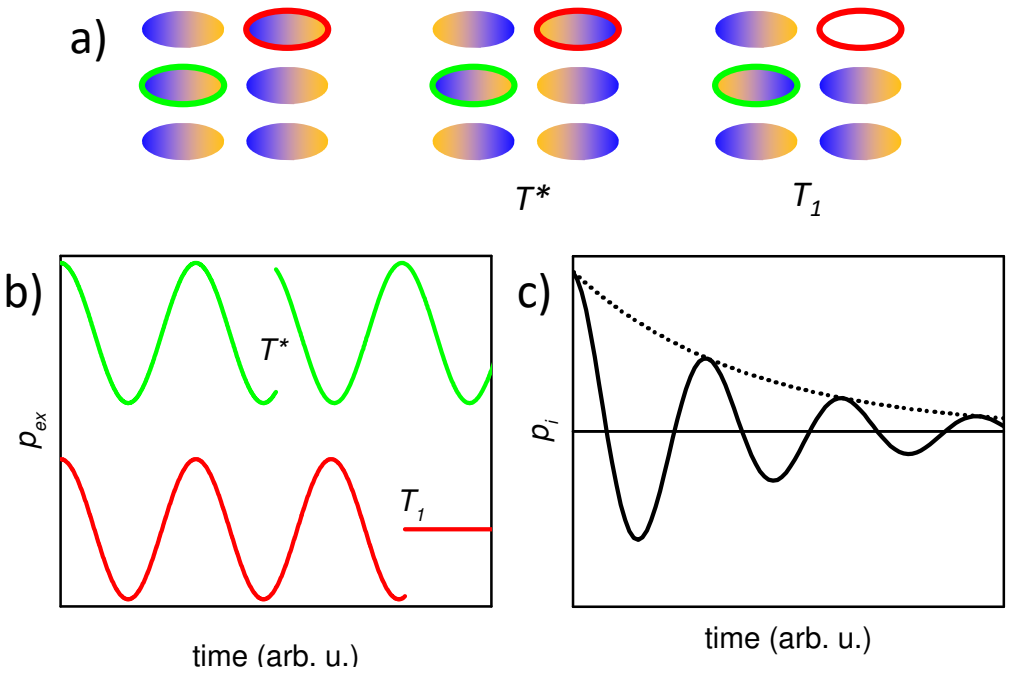

Figure 2.11: Dephasing mechanisms a) Single dipoles p_{ex} (like excitons, atoms, molecules, etc.) induce a microscopic polarization p_i which gets lost by b) pure dephasing T^* (green) and recombination T_1 (red). c) The overall polarization of the volume diminishes.

1. Recombination (red ellipse): If the excitation relaxes back into the ground state (described by the time T_1), the entire polarization of the dipole is lost. This can occur radiatively (coherent light scattering, fluorescence, phosphorescence) or non-radiatively by dissipation.
2. Phase breaking (green ellipse): Due to temporal fluctuations of the environment, each single dipole can spontaneously change its phase, so that it no longer constructively interferes with the ensemble. Elastic collisions with phonons, defects or other excitations typically influence the phase in a solid crystal [93]. These processes are denoted as "pure dephasing" with the time T^*.

Figure 2.11b shows the oscillations of the two different dipole moments in Figure 2.11a where the red one relaxes into the ground state after the time T_1 (i. e. zero dipole moment afterwards) and the green one instantly changes its phase after T^*. Both processes diminish the total polarization of the volume over time. The amplitude of the polarization of the total microscopic volume decays with a factor of e^{-t/T_2}. Since the optical Bloch

equations (2.30) are in the rotating frame of reference of the electric field, the polarization of the microscopic sample volume oscillates in the rest frame with decaying amplitude (see Figure 2.11c).

Inhomogeneous broadening

However, a typical macroscopic sample volume contains different absorbers with different transition frequencies $\omega_i = \omega + \delta_i$ due to local variations of the environment (see Figure 2.12a) [94, 95]. Consequently, the microscopic polarizations oscillate with various different frequencies. This also diminishes the macroscopic polarization in addition to dephasing [93] and is depicted in Figure 2.12b. In the rotating frame of the electromagnetic field, the Bloch vectors of each microscopic sample volume are first aligned parallel to the y-axis which describes the state of maximal macroscopic polarization (time zero in Figure 2.12b). This can be achieved by an initial $\frac{\pi}{2}$-pulse (see Figure 2.12c-i). Since the resonance frequencies are different, the Bloch vectors spin around $\begin{pmatrix} 0 \\ 0 \\ \delta_i \end{pmatrix}$ with individual angular frequency δ_i after excitation.

Therefore, the phase of each individual microscopic polarization differs from the mean by $\delta_i \cdot \tau$ after the time τ which is called “free induction decay” (see Figure 2.12b and c-ii). The overall macroscopic polarization of the ensemble decays with the rate $\frac{1}{T_2^*} > \frac{1}{T_2}$ and depends on the spectral spread δ of the different resonance frequencies (“inhomogeneous linewidth”, see Figure 2.12a and detailed discussion in 2.2.1). Although T_2^* is usually much smaller than T_2, it is possible to obtain the dephasing time. In other words, the homogenous linewidth $\Gamma = \frac{2\hbar}{T_2}$ of an atom, exciton, molecule, etc. can be determined even if the inhomogeneous linewidth of the ensemble is much larger and the experimental setup does not permit the isolation of single species.

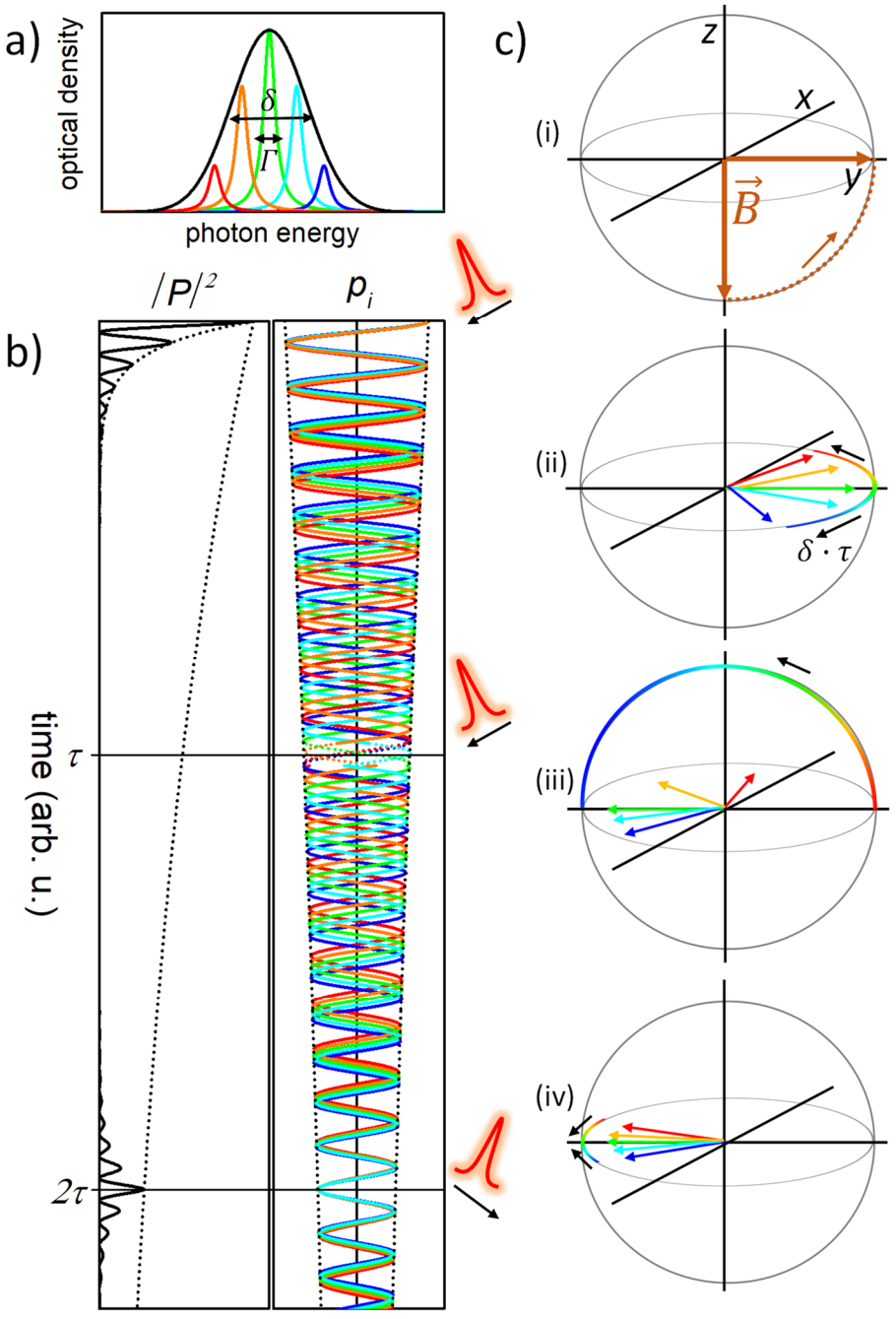

Figure 2.12: Effects of inhomogenous broadening and photon echo: a) Single absorbers at different resonances broaden the linewidth of a transition. b) The individual microscopic polarizations $\boldsymbol{p_i}$ oscillate with different frequencies after excitation which diminishes the overall macroscopic polarization $\boldsymbol{P}$ in addition to the dephasing. A second laser pulse at the time τ allows a "revival" at 2τ (photon echo). c) Bloch vectors shown for: excitation with $\frac{\pi}{2}$ –pulse i), free induction decay (in the rotating frame) ii), π–pulse iii) and rephasing iv).

The experimental technique is called “photon echo spectroscopy” [96] and is shown in Figure 2.12c: i) Analogously to spin echoes [97], first a macroscopic polarization is created on the sample by excitation with a coherent light pulse. As mentioned above, maximum polarization can be achieved with a $\frac{\pi}{2}$ – pulse where all Bloch vectors are aligned parallel to the y-axis. ii) Due to different resonance frequencies, each individual polarization rotates in the xy-plane and their Bloch vectors diverge (free induction decay) in the rotating frame of the electromagnetic field. iii) After the time τ, the sample is illuminated with a second light pulse in resonance to the absorbers. The Bloch vectors of each microscopic polarization coherently precess around $\begin{pmatrix} \Omega_\mathrm{R} \\ 0 \\ 0 \end{pmatrix}$.

If the duration T of the second pulse fulfils $\Omega_\mathrm{R} T = \pi$, the y-components invert: $B_y \sim \cos(\delta_i \cdot \tau) \rightarrow \cos(\pi - \delta_i \cdot \tau)$. After the second pulse, the precession around $\begin{pmatrix} 0 \\ 0 \\ \delta_i \end{pmatrix}$ continues again, with a phase shift: $B_y \sim \cos(\delta_i(t-\tau) + \pi - \delta_i \tau)$. iv) Consequently *all* Bloch vectors are aligned along the y-axis again after $t = 2\tau$ for *any* detuning δ_i. The macroscopic polarization $\boldsymbol{P}$ of the sample “rephases” and emits radiation which is called “photon echo”. The intensity I of the emitted radiation is proportional to $|\boldsymbol{P}|^2$ and decays exponentially versus the delay time τ of both pulses:

$$I(\tau) = I_0 e^{\tau/\tau_{ph}} \sim |P(2\tau)|^2 = |P_0|^2 e^{4\tau/T_2}. \tag{2.32}$$

Therefore, the decay constant τ_{ph} allows to determine the dephasing time: $\tau_{ph} = T_2/4$. If inhomogeneous effects are negligible, the polarization is not diminished by the free induction decay. In this case, no “rephasing” upon the second pulse is necessary to emit radiation. Consequently, the intensity of the emission versus delay time is proportional to $|P(\tau)|^2 = |P_0|^2 e^{2\tau/T_2}$. I. e. in this case, the decay constant is: $\tau_{ph} = T_2/2$ [96]. To determine the dephasing time, it is therefore essential to know which of both regimes (dominating inhomogeneous or homogenous linewidth) is valid for the analysed sample.

In this thesis, the homogenous linewidth of excitons in semiconductor nanocrystals was measured with degenerate four-wave mixing. The experimental technique allows the observation of photon echoes and is explained in 3.2.2.

2.2.3 Quantum beat spectroscopy

The previous chapter showed that the homogenous linewidth of a resonance can be resolved by measuring the dephasing time in the time domain. A similar method can be applied to resolve discrete energy spacings within a sample (like two adjacent transitions within an atom). If the energetic gap is small, inhomogeneous broadening can smear out energy levels so that they cannot be resolved in linear optical spectra (see 2.2.1). In the following, a system with two excited states $|1\rangle$ and $|2\rangle$ at the energies E and $E + \Delta E$ is considered (see Figure 2.13a). According to the time-dependent Schrödinger equation, their dynamics evolve proportional to $e^{i\frac{E}{\hbar}t} + cc$ and $e^{i\frac{E+\Delta E}{\hbar}t} + cc$ (Figure 2.13c).

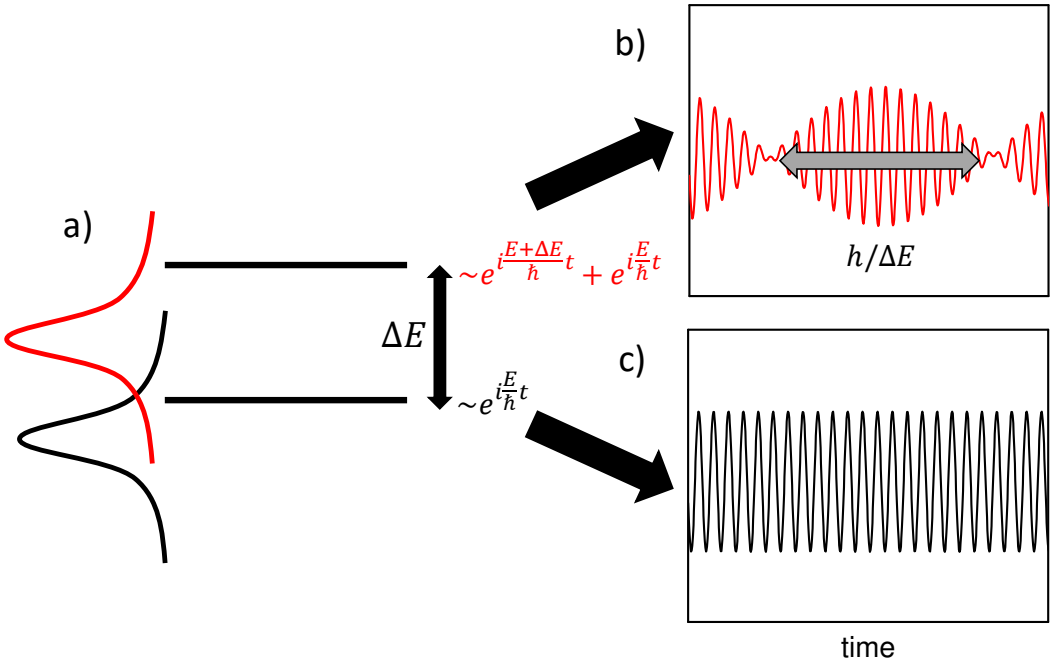

Figure 2.13: Quantum beats for two adjacent excited states a) If the energy difference ΔE between both states is small they can be coherently excited and the time dynamics of the system b) are modulated with a beat in comparison to c) the excitation of only one transition.

When both of them are coherently excited (for example by a laser with a sufficient spectral bandwidth), the respective excited state is a superposition of $|1\rangle$ and $|2\rangle$. The

time dynamics are then proportional to $e^{i\frac{E}{\hbar}t} + e^{i\frac{E+\Delta E}{\hbar}t} + cc = e^{i\frac{E}{\hbar}t}\left(1 + e^{i\frac{\Delta E}{\hbar}t}\right) + cc$. Under the condition that the energetic gap between both states is very small (i. e. $E \gg \Delta E$), the oscillations of the polarizations with the angular frequency $E/\hbar$ is modulated with a slow beat $\Delta E/\hbar$ (see Figure 2.13b) [98, 99]. Periodic minima are obtained at multiples of $\frac{h}{\Delta E}$. The beat also affects the photon echo and the emission periodically goes through minima. This allows to determine the energy difference ΔE in the time domain. Since the time domain is inverse to the frequency space, small energetic gaps can be resolved better in case of inhomogeneous broadening.

The described technique of quantum beat spectroscopy has been used to measure the binding energy of excitons in InGaAs/GaAs quantum wells with four-wave mixing [100]. In this thesis, similar experiments are conducted with methylammonium lead iodide nanoplatelets.

3 Experimental Setups

A commercial femtosecond titanium sapphire (Ti:Sa) amplifier with an optical parametric amplification unit was implemented as a part of this thesis. The laser system was used as light source for a transient absorption spectrometer and degenerate four-wave mixing. Figure 3.1 shows the basic scheme of the beam geometry for the experiments. In the following chapter, all components will be described. The focus will be on the technical specifications and limits with respect of the measured observables.

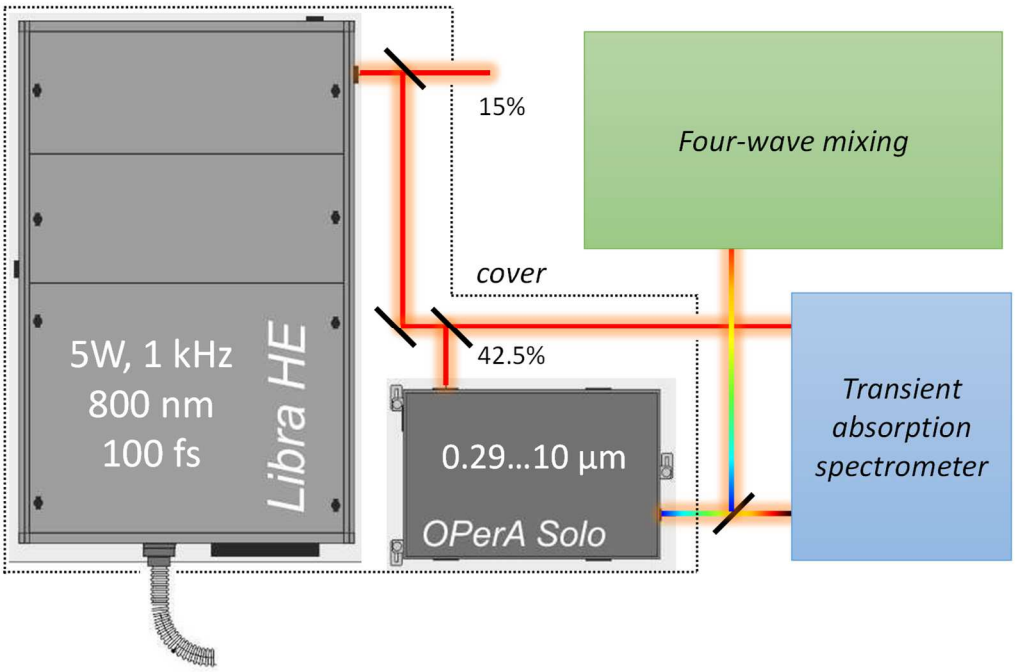

Figure 3.1: Experimental setups with light source Laser pulses with a duration shorter than 100 fs were generated with a Ti:Sa amplifier system. Two beam splitters are used to couple 42.7 % of the output power into an optical parametric amplifier to convert the 800 nm pulses into a wide spectral range. The experimental setups of transient absorption spectroscopy and four-wave mixing were used in this thesis.

3.1 Ultrashort laser pulse generation

For all performed experiments, a sub-picosecond time resolution is required. Since current electronic devices cannot achieve such a resolution, ultrashort laser pulses are to date the only way to get insight to such short dynamics. In addition to <100 fs pulses, the whole laser system used for the experiments allows a gap-free tunability of the emission wavelength between 10 µm and 290 nm. This facilitates a precise analysis of the nonlinear signatures of different samples over a wide spectrum.

3.1.1 Femtosecond titanium sapphire laser amplifier

The core of the laser system is a *Libra HE* Ti:Sa amplifier purchased from *Coherent Inc*. The pulse duration at the output was measured by autocorrelation. Under the assumption of a Gaussian pulse shape, the FWHM was 90 fs. The spectrum is centred around 800 nm. The maximum repetition frequency is 1 kHz with 5 mJ of pulse energy.

Figure 3.2a shows the basic optical geometry of the amplifier. In principle, it consists of the following five units: The pump (i) and seed lasers (ii), the regenerative amplifier unit (iii) (depicted in Figure 3.2b), the pulse stretcher (iv) and compressor (v). The Ti:Sa crystal of the amplifier is pumped by a Q-switched, frequency doubled Nd:YLF laser (*Evolution*) [101]. Its wavelength of 532 nm matches the absorption band of titanium doped sapphire. Pump powers up to 24 W can be achieved with a repetition rate of 1 kHz.

The seed laser is a mode-locked Ti:Sa oscillator pumped by a continuous wave (cw) diode laser (*Vitesse*). Passive mode-locking is achieved with a Kerr-lens [102] and spontaneously starts at a pump power of about 1.3 W. The repetition rate is 80 MHz with an average power of 300 mW. The amplification of the seed pulse follows the principle of chirped pulse amplification [103]: Since the pulse length of the seed is in the range of few picoseconds, extraordinary high pulse powers would be achieved within the regenerative amplifier. To prevent damage of the respective optics, the pulse is initially stretched in time by multiple reflections on a gold grating. Different spectral components disperse due

to different path lengths within the stretcher unit. After the pulse is coupled out of the amplifier unit, the latter process is reversed with a second grating in the compressor unit a pulse duration shorter than 100 fs is achieved.

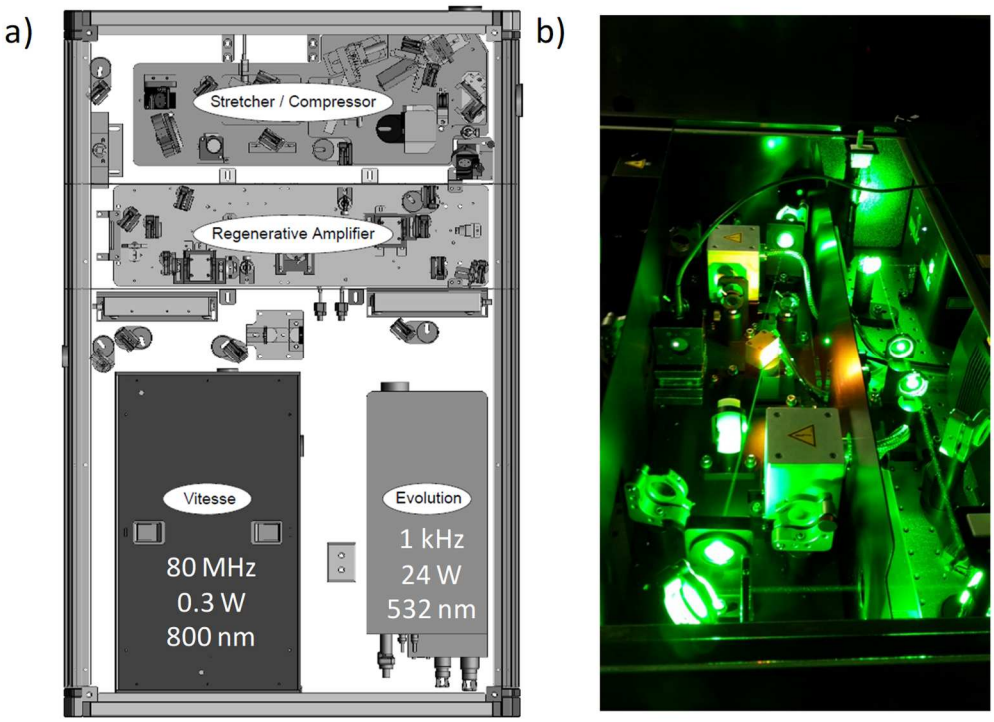

Figure 3.2: Amplifier layout a) Scheme of *Libra HE* [104]. The seed pulses are generated with a mode-locked Ti:Sa laser (*Vitesse*). The regenerative amplifier is pumped by a Q-switched laser (*Evolution*). The pulses are stretched in time before entering the amplifier unit and compressed afterwards. b) Image of regenerative amplifier under operation.

Two Pockels cells with subsequent thin film polarizers and $\lambda/2$-waveplates control the in- and outcoupling of the stretched seed pulses in the amplifier unit to achieve optimal gain and recovery [104]. The geometry allows best performance for a repetition rate of 1 kHz, i. e. one of 80.000 pulses is amplified. It takes about 15 round trips inside the cavity until saturation of the pulse energy is achieved. A Faraday insulator before the pulse stretcher unit prevents back reflections into the seed laser which could disturb the operation. The band width of the seed pulse is permanently observed with a photodiode alerting instabilities of the mode-locking.

A water heat exchanger fabricated by *Polyscience* is used to cool the Ti:Sa crystal, pump and seed laser to 19°C. The accuracy is less than 0.1 °C. All components are mounted on a monolithic breadboard with a cover to protect the system from any external influences.

A 0.85:0.15 semi-transparent mirror is used to split about 0.75 W from the laser output for various experimental purposes. The remaining 4.25 W is halved with another beam splitter: One part is used to pump the optical parametric amplifier whereas the other delivers the probe pulse for the transient absorption spectrometer (see 3.2.1 and Figure 3.1).

3.1.2 Optical parametric amplifier

Optical parametric amplification (OPA) is used to tune the wavelength of the Ti:Sa output from 800 nm to any arbitrary value between 10 µm and 290 nm. Various additional configurations are necessary to ensure a spectral manipulation over more than five octaves:

The basic principle is the down conversion of one photon with $\omega_\mathrm{p} = \frac{2\pi c}{800\,\mathrm{nm}}$ into two photons by second-order nonlinear optical interaction on a β-barium borate (BBO) crystal: $\omega_\mathrm{p} = \omega_\mathrm{s} + \omega_\mathrm{i}$. The generated photon at higher frequency ω_s is denoted as “signal” whereas the one at ω_i is called “idler” [105]. This process is achieved in two steps inside a commercial optical parametric amplifier (*OPerA Solo* from *Coherent Inc.*) and is schemed in Figure 3.3a: Few percent of the incoming beam #1 is split at BS1 to generate spontaneous parametric down-conversion (pre-amplification path #3). To seed the pre-amplification, beam #3 is split at BS2 where one part propagates through a sapphire plate (WLG) and generates a white light continuum (#5). The white light pulse non-collinearly overlaps with the other part #4 on a BBO crystal (NC1 depicted in Figure 3.3b). To separate spectral components in time, the continuum propagates through a highly dispersive medium (TD). The temporal overlap can be controlled with a delay line on which the mirrors M1 and M2 are mounted. The signal (800 nm$\leq \omega_\mathrm{s} \leq$ 1600 nm) of the

spontaneous parametric down conversion #6 seeds the actual optical parametric amplification.

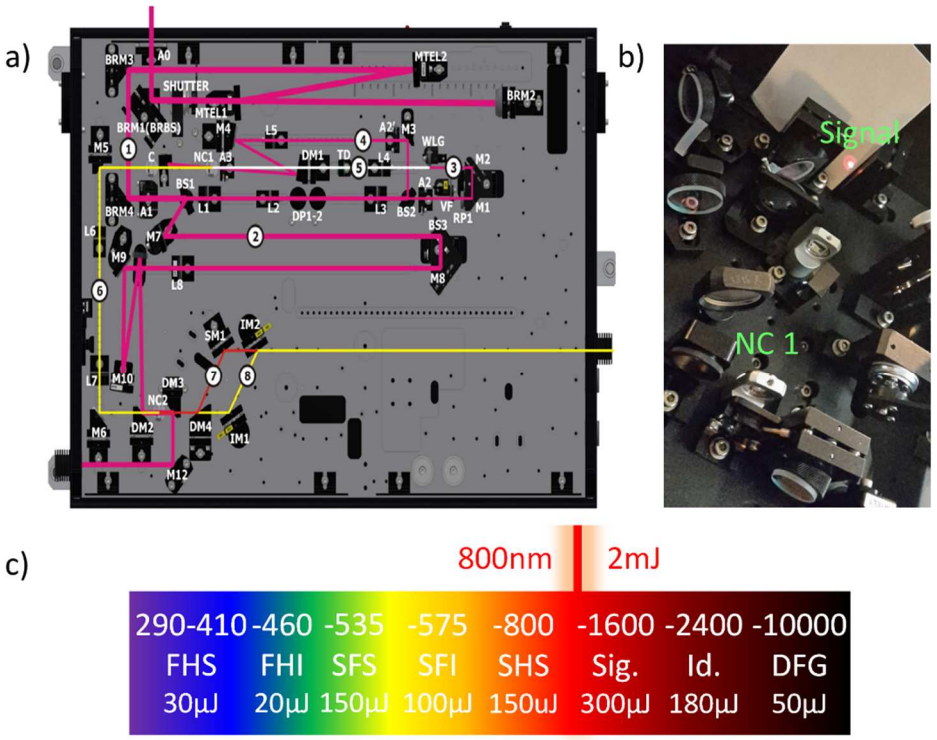

Figure 3.3: Optical parametric amplifier: a) Scheme of beam geometry [106] with b) image of nonlinear crystal (NC 1) and pre-amplified signal beam. c) OPA configurations with respective spectral range in nanometres. FHS/FHI: Fourth harmonic signal/idler. SFS/SFI: Sum frequency signal/idler. DFG: Difference frequency generation.

The amplification is achieved by collinearly overlapping the pre-amplified signal with the residual Ti:Sa output (#2) on another BBO crystal (NC2). Temporal coincidence is achieved by rotating two Brewster angled plates (DP1 and DP2) in opposite directions. The down-conversion makes the pump pulse #2 at ω_p weaker and amplifies ω_s (#7) while generating the corresponding idler (#8) [106]. Up to 20% conversion efficiency is achievable with the presented configuration. The signal and corresponding idler wavelength are $\omega_s \approx$ 1300 nm and $\omega_i \approx$ 2080 nm for optimal conversion. The pulse energies are approximately 0.3 mJ and 0.18 mJ for signal and idler respectively. The conversion efficiency strongly decreases close to the fundamentals, i. e. $\omega_s \rightarrow$ 800 nm, 1600 nm.

Two subsequent second harmonic generators can optionally be used to tune the wavelength into the visible or even ultra violet regime. Furthermore, the signal pulse can be overlapped with a part of the amplifier output to generate sum- and difference frequency: $\omega = \omega_{\mathrm{p}} \pm \omega_{\mathrm{s}}$. Figure 3.3c schematically shows the respective (recommended) configurations for different wavelength ranges with typical pulse powers. In principle, a low-noise output is only possible for maximal pulse compression inside the Ti:Sa amplifier. To shield any potential influences of the laboratory environment, an aluminium cover was built around the entire system.

3.2 Optical setups

3.2.1 Transient absorption spectrometer

Transient absorption spectroscopy is a method to detect changes in the absorption spectrum of a sample which occur upon irradiation with light. Basically, two beams are overlapped and the spectrum of one is detected behind the sample. A custom-built transient absorption spectrometer from *Newport Inc*. was set up to perform the experiments of this thesis. The beam geometry and the detection unit is shown in Figure 3.4a and b. The output of the OPA was used to excite the sample (pump pulse) and the amplifier output which is transmitted through the beam splitter in front of the OPA (see Figure 3.1) for probing. Since the pump pulse propagates about 3.6 m inside the OPA, an additional delay on the optical table is required for the probe pulse.

Temporal resolution of the transient absorption is realized by a lag time between pump and probe pulse. This is achieved by manipulating the pathway of the probe pulse with a double-pass optical delay line (see Figure 3.4a). It consists of a retroreflector (RR) mounted on a linear translation stage. Since the beam propagates through the delay line twice, the overall delay is $\tau = \frac{4\Delta x}{c}$. Δx is the displacement of the stepping motor. Its minimum repetable incremental motion is $\Delta x = 1$ µm [107] which corresponds to a delay time of 13 fs. Therefore, the temporal resolution is only limited by the pulse duration (≈100 fs). A maximum delay of 3.3 ns is given by the overall length (250 mm) of the translation stage.

To obtain maximal spectral information, a continuous white light pulse is generated by focusing the probe beam into a dispersive material (white light generation – WLG in Figure 3.4). Different spectra can be obtained for different crystal materials: CaF_2 was used to probe in the visible and ultraviolet regime up to 360 nm. Stable near-infrared spectra were achieved with an yttrium aluminium garnet (YAG) crystal. The spectra can be controlled by adjusting the intensity, waist and focus of the probe beam in the crystal. To minimize the pulse length, the white light is generated directly in front of the sample.

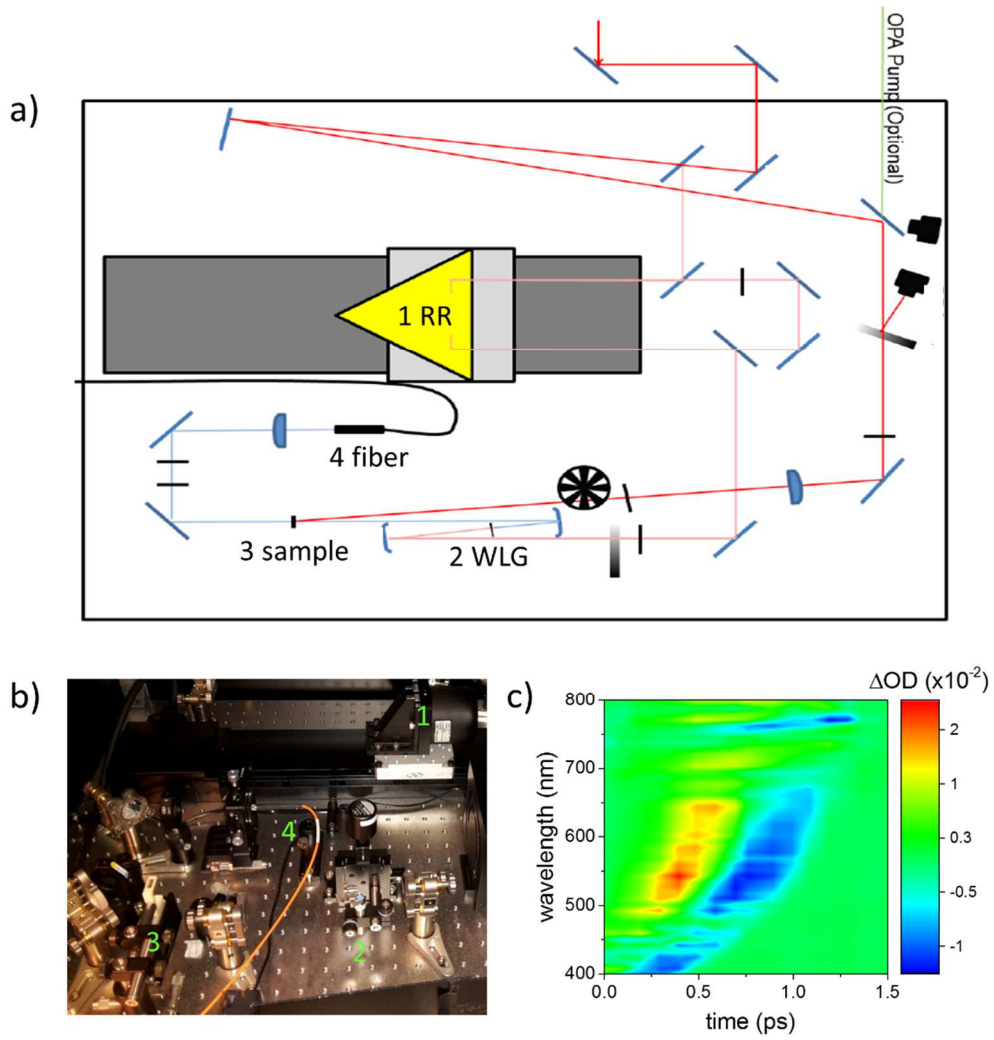

Figure 3.4: Transient absorption spectrometer a) Scheme of beam geometry with real image [108] b) of the detection unit. Numbers are labelled in a). c) A transient absorption spectrum of water shows the spectral chirp which is due to the dispersion of the white within light pulse.

The diameter of the pump beam (FWHM) on the sample is approximately 200 µm and significantly larger than the probe beam which is ≈50 µm. This ensures stability of the overlap since fluctuations can occur for different delay positions ("walk-off"). A filter diminishes the fundamental wavelength at 800 nm before the probe beam is coupled into a CCD-spectrograph with a fibre. An optical chopper synchronized to the repetition rate of the amplifier is used to block every second pump pulse. The camera of the spectrograph is triggered to the chopper frequency and records differential spectra with blocked and unblocked pump beam:

$$\Delta OD(\lambda) = \log(I_{\text{off}}(\lambda)) - \log(I_{\text{on}}(\lambda)). \tag{3.1}$$

$I_{\text{off/on}}(\lambda)$ are the counts on the pixels for the respective wavelength λ with blocked/unblocked pump pulse. If $\Delta OD < 0$, the transmission through the sample has increased upon excitation. Every spectrum was averaged for two seconds, i. e. an average of 1000 single differential absorption spectra was taken. In this configuration, a resolution of $\Delta OD(\lambda) < 0.1\ \%$ can be achieved.

Due to dispersion effects, higher frequencies propagate slower within the envelope of the probe continuum, so the overlap with the excitation pulse occurs at smaller delay times. Consequently, the condition $\tau = 0$ is wavelength-dependent. Figure 3.4c shows the transient absorption spectra of water versus the time delay τ. Since water has no absorption band in the observed spectral region, changes in the absorption spectrum are due to polarizations induced by the electric field of the pump pulse (at 330 nm) [82]. The effect that the onset is obviously not occurring at the same delay for every wavelength is called “chirp”. Therefore, a chirp correction was essential for any measurements acquired in the presented thesis because sub-picosecond dynamics were analysed. To exclude any influences of the setup parameters (like different beam waist, focus, intensity, etc.) the chirp was corrected individually for each measurement. A free open-source program (“PyTrA”) [109] was used to model the chirp with a second-order polynomial function and modify the data matrix such that the delay τ is constant for every wavelength.

3.2.2 Degenerate transient four-wave mixing

As described in 2.2.2, the coherent interaction of two sequential coherent electromagnetic pulses can lead to the emission of a photon echo which allows a direct observation of the dephasing time. A suitable experimental technique to observe photon echoes is degenerate transient four-wave mixing. The experimental setup is shown in Figure 3.5a: The OPA output was split into two beams, #1 and #2. To achieve a tuneable time delay τ, #1 propagated through an optical translation stage. Both were focused on

the sample (green bar) with a thin lens. The wave vectors of both beams in front of the sample are denoted as $\boldsymbol{k}_1$ and $\boldsymbol{k}_2$.

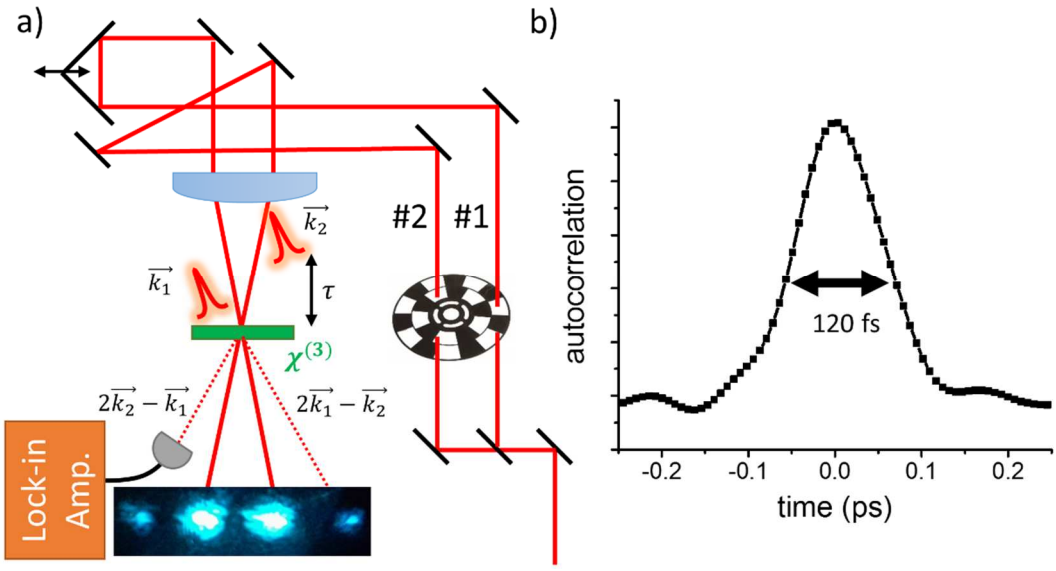

Figure 3.5: Degenerate four-wave mixing: a) Beam geometry of experiment. Two symmetric beams are focused on the sample (green). The detector is placed along $\boldsymbol{2k_2 - k_1}$. At high intensities and temporal overlap of both pulses, the beams along $\boldsymbol{2k_2 - k_1}$ and $\boldsymbol{2k_1 - k_2}$ can be observed by eye on a screen behind the sample. The detection unit is based on the lock-in technique synchronized to an optical chopper. b) Auto correlation function of pulses before the sample.

A macroscopic first-order polarization is created in the sample by the first pulse. The electric field of the second pulse interferes with it and generates a real population of (in case of a semiconductor) bound or unbound electron-hole pairs in the material. Due to the interference, the population density of the excited states are spatially modulated along the sample. A “transient” grating with a periodically alternating refractive index is formed [110]. Now, a third laser beam can be diffracted from the grating to generate a “new” fourth electromagnetic wave behind the sample (*four*-wave mixing). However, a third beam is not necessary since the delayed pulse itself can be diffracted. The latter approach is called degenerate four-wave mixing and is the experimental setup shown in Figure 3.5a. Depending on whether pulse #1 or #2 arrives first, self-diffracted beams can be observed along $2\boldsymbol{k}_2 - \boldsymbol{k}_1$ or $2\boldsymbol{k}_1 - \boldsymbol{k}_2$.

The transient grating is a descriptive model to understand the interaction of the electric field of the second laser pulse with the first-order polarization in the sample. Higher-order polarizations are generated. The third-order polarization $\boldsymbol{P}^{(3)}$ (induced by the third-order electric susceptibility $\chi^{(3)}$ of the sample and the electric fields of #1 and #2) is equivalent to the self-diffraction because it is emitted along $2\boldsymbol{k}_2 - \boldsymbol{k}_1$ and $2\boldsymbol{k}_1 - \boldsymbol{k}_2$ [105]. Since $\boldsymbol{P}^{(3)}$ is irradiated after the second laser pulse, it can be understood analogously to the emission of the photon echo (see 2.2.2). It can be shown, that the diffracted pulses are emitted at the time 2τ [111].

In the present experimental setup of Figure 3.5a, the third-order polarization along $2\boldsymbol{k}_2 - \boldsymbol{k}_1$ was detected with a fast photodiode. To minimize noise effects, both incident beams were modulated with an optical chopper equipped with a 42/30-slot wheel: Beam #1 was modulated with 500 Hz, beam #2 with 357 Hz. Therefore, the irradiated third-order polarization was found at 143 or 857 Hz. A lock-in amplifier synchronized to 143 Hz was used to read out the signal of the photodiode. For each delay τ, the output of the diode was integrated over 30 ms with a subsequent recovery time of 300 ms to avoid any artefacts of previous measurements. The intensity of the signal $I(\tau) = \frac{1}{30\ \mathrm{ms}} \int_0^{30\ \mathrm{ms}} \left|\boldsymbol{P}^{(3)}(\tau, t)\right|^2 dt$ ("time-integrated photon echo") is plotted versus the delay position. According to equation (2.32), $I(\tau)$ allows the determination of the dephasing time.

Every measurement was repeated 10-150 times (depending on the noise level) and finally averaged. It was found that longer integration times but with less averages do not optimize the signal to noise ratio. An optimum of both was achieved with the mentioned parameters to minimize the measurement time. Scattered light from the sample is the most important noise source, since it also has a component which is modulated with the difference frequency of both beams. Apertures after the sample and before the detector were used to minimize scattered light on the diode.

The samples were placed in a cryostat cooled with liquid helium. Due to optimal heat conductivity, only sapphire substrates were used. The material was deposited by drop

casting before each single measurement cycle to avoid any degrading effects of the material. To protect the sample from moisture, a layer of *poly(methyl methacrylate)*, PMMA, was deposited on top of the material.

Figure 3.5b shows the autocorrelation of the laser pulse after the sample. The FWHM is 120 fs and gives the time resolution of the setup. All transparent optics in front of the sample (beam splitter, attenuator and lens) were kept as thin as possible. Various pinholes ensured parallel beam alignment before the focusing lens. The diameter of both beams (FWHM) was 150 µm in the focal plane.

4 Optical Nonlinearities of Plexcitons

As described in 2.1.3, strong coupling between an electromagnetic mode and an emitter leads to "hybrid" excitations. Such phenomena have been observed for various emitters in optical cavities [112-114] even on the single particle level [115, 116]. Efforts have been made to develop systems with exceptional high coupling constants. Since the interaction strength is the product of the electric field and the dipole moment of the emitting material, an enhancement of both parameters is the approach to achieve strong interaction. On the one hand, dyes of molecular J-aggregates exhibit a large dipole moment because of internal alignment of each individual molecule within the aggregate (see 2.1.2). When they are embedded in an optical micro cavity, a Rabi splitting up to several hundreds of meV is achievable [117, 118] in comparison to only a few meV with gallium arsenide quantum wells [114, 119].

On the other hand, localized surface plasmon resonances in metal structures exhibit strong polarizations with a great enhancement of the local electromagnetic field [40, 120]. Therefore, extraordinary strong coupling between molecular J-aggregates and numerous metal nanoparticles have been realized [80, 121-126]. Similar to an emitter in a cavity (see 2.1.3), hybrid states of plasmons in the metal and excitons in the dye, the so-called plexcitons, are formed [127-129]. Despite of big interest, it has not been addressed whether a plexciton can show both plasmonic and/or excitonic behaviour. The following chapter is devoted to answer this question with transient absorption spectroscopy for a model system comprising gold nanorods coated with a J-aggregated cyanine dye. A very simple model based on two coupled Lorentz oscillators was set up to explain the linear and nonlinear optical properties of plexcitons in the pico- and sub-picosecond range. It was

found that plexcitons have a tunable plasmonic and excitonic optical behaviour depending on the spectral offset between plasmon and exciton.

The work was done within the scope of a collaboration with professor Luis Liz-Marzan and professor Yury Rakovich from the Centro de Física de Materiales and the CIC biomaGUNE in San Sebastion. Dimitry Melinikau and Ana Sánchez-Iglesias synthesized the particles. The synthesis and any respective chemical mechanisms are beyond the scope of this thesis. The focus of the research was set to investigate the structures with optical spectroscopy and understand the effects of the coupling mechanism.

4.1 Linear optical extinction of plexcitons

In the first part of this subchapter, the linear extinction spectra of gold nanorods, J-aggregated cyanine dye molecules and composite particles of both materials are described and discussed. The second part focuses on a quantitative analysis utilizing a simple coupled Lorentz oscillator model. Phenomena of strong coupling between the plasmon polarization of the gold nanorods and the excitons in the dye molecules are observed. These experimental findings can be modelled exclusively on the basis of the respective coupling constant.

4.1.1 Sample preparation and characterisation

Gold nanorods

Colloidal gold nanorods with different aspect ratios were synthesized in two steps: First, relatively long rods (66 nm x 15 nm) were fabricated by a method based on silver-assisted seeded growth [130]. Second, rods with various aspect ratios (length/width) were extracted by partial oxidation with different amounts of Au^{3+}-CTAB complexes [131]. The dimensions were determined by TEM imaging.

Sample	Length	Width	Aspect ratio	Resonance
1	66 ± 3 nm	15 ± 3 nm	4.4	1.43 eV
2	60 ± 4 nm	16 ± 2 nm	3.8	1.53 eV
3	56 ± 4 nm	15 ± 1 nm	3.7	1.60 eV
4	51 ± 4 nm	15 ± 1 nm	3.4	1.70 eV
5	48 ± 4 nm	16 ± 1 nm	3.0	1.78 eV
6	38 ± 3 nm	15 ± 1 nm	2.5	1.91 eV
7	34 ± 6 nm	18 ± 2 nm	1.9	2.1 eV

Table 4.1: Gold nanorods with different morphologies and longitudinal plasmon resonances.

The sample characteristics are summarized in Table 4.1. The extinction spectra of all samples with the aspect ratios ranging from 4.4 to 1.9 are shown in Figure 4.1a. Due to the elongated shape of the nanorods, two plasmon resonances appear.

As discussed in section 2.1.1, plasmon resonances depend on the morphology of the respective particle. In case of gold nanorods, oscillations of the free electron cloud can occur in longitudinal and transverse direction. By increasing the aspect ratio, the longitudinal plasmon resonance shifts to lower energy and the transverse one to higher energy [40]. However, the latter cannot be shifted beyond about 2.4 eV, since the onset of the interband transition is at 2.38 eV. Therefore, the respective peak flattens because of enhanced interband damping of the plasmon oscillation. The longitudinal plasmon resonance shows versatile tunability with nearly equal steps between 1.4 and 2.1 eV.

Importantly, the observed FWHM γ_{pl} of each plasmon resonance in the absorption spectrum is not equal to its homogenous linewidth. Statistic variations of the aspect ratios cause differences of the plasmon resonance energy between individual gold nanorods within the sample. Consequently, each particle has a plasmon resonance E_i with a spectral offset δ_i from the average value which is the resonance maximum E_{pl} in Figure 4.1a: $E_i = E_{\mathrm{pl}} \pm \delta_i$. Therefore, the observed linewidth is a convolution between the homogenous linewidth $\Gamma_{\mathrm{pl}} = \frac{2\hbar}{T_2}$ (resulting from the dephasing time T_2) and the overall spectral variance δ of all nanorods within the dispersion, so $\gamma_{\mathrm{pl}} > \Gamma_{\mathrm{pl}}$. To estimate the homogenous linewidth, the extinction cross section of single gold nanorods was calculated by Mie scattering with parameters according to [47]. The dimensions of the particles were estimated from TEM images for the calculations. Such computations have been shown to match perfectly with the corresponding experimental data of single particles (see 2.1.1). The simulated extinction spectra of sample 2 and 7 give a homogenous linewidth of Γ_2 =100 meV and Γ_7 =160 meV. Under the assumption that the plasmon energy of each individual gold nanorod E_i is distributed around E_{pl} with a Gauss profile, it can be estimated that each plasmon resonance is inhomogeneously broadened by $E_{\mathrm{pl}} \pm$ 100 meV for every sample. This relation will be used for calculations in the next chapter.

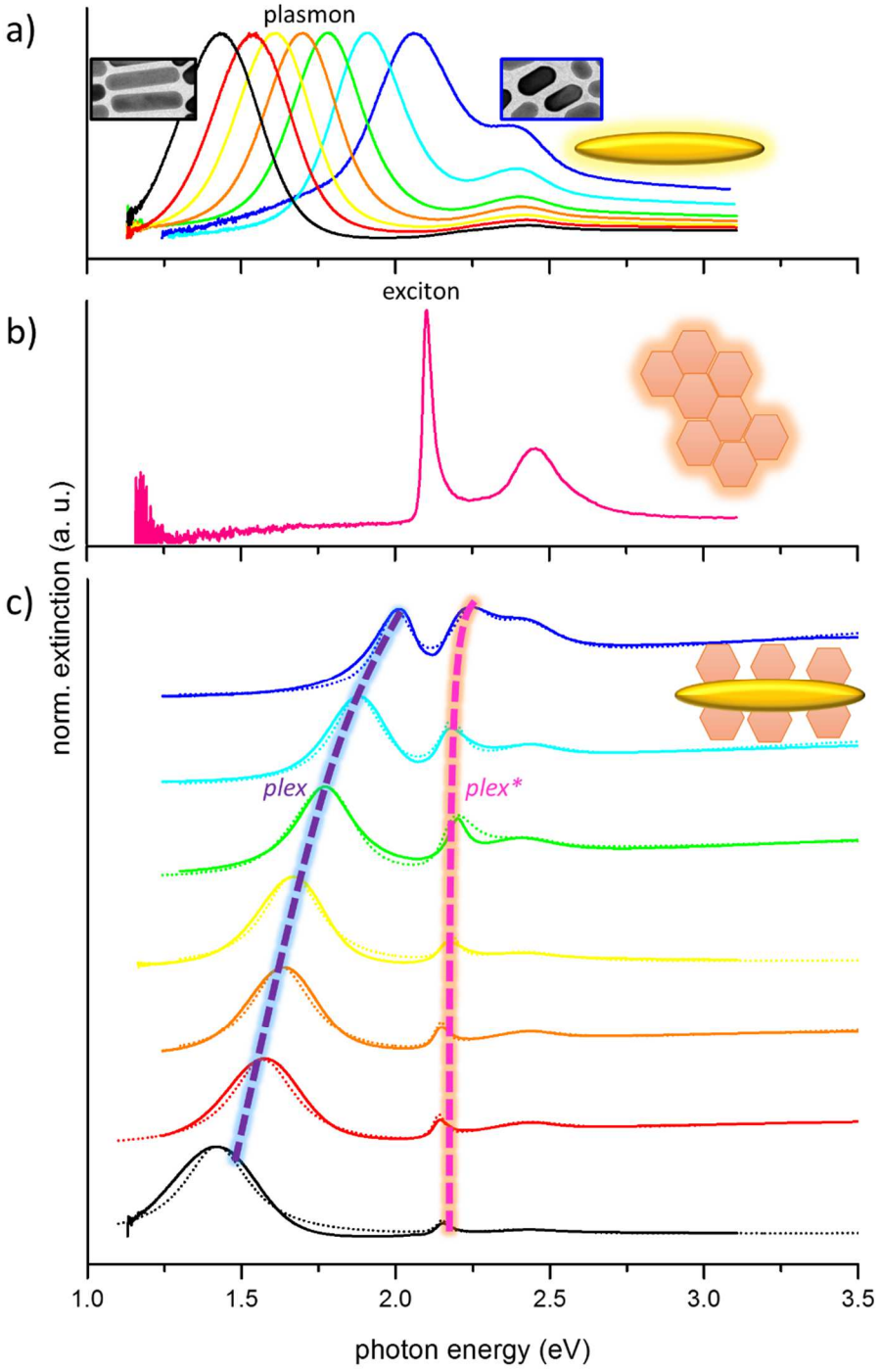

Figure 4.1: Linear extinction spectra a) Gold nanorods with variable aspect ratios. The longitudinal and transverse plasmon appear as resonance maxima. b) J-aggregated cyanine dye molecules. The J-band is located at 2.1 eV. b) Hybrid structures of both components. The longitudinal plasmon resonance couples to the J-band and two new resonances *plex* and *plex** occur. The spectral overlap between J-band and longitudinal plasmon decreases with increasing aspect ratio.

Cyanine dye

Figure 4.1b shows the extinction spectrum of the J-aggregated dye molecules (technical name and chemical structure is shown in section 2.1.2) in water. J-aggregation spontaneously occurs when the pH value is slightly increased. This was achieved by adding ammonia. The sharp and strong resonance of the J-band can be clearly observed at 2.1 eV, as well as the non-aggregated monomers absorbing around 2.5 eV.

Hybrid structures of the dye and the gold nanorods were synthesized by adding few µl of concentrated dye solution (in ethanol) into each colloidal dispersion of gold nanorods. Upon addition of ammonia (to increase the pH value), the dye molecules attach to the surface of the gold nanorods. Since not all molecules bind to it, a subsequent centrifugation step was carried out to remove the excess dye.

Gold nanorod – dye hybrid structure

The difference in the extinction spectrum between the hybrid structures and the bare components is most striking for the shortest rods in Figure 4.1c. Here, the longitudinal plasmon resonance spectrally matches with the J-band. Although both have an extinction maximum at 2.1 eV, the composite system has a minimum there. Two maxima are located symmetrically around it: One at 1.97 eV and the other one at 2.23 eV. These “new” resonances are caused by the strong coupling of the plasmon polarization and the exciton on the dye. Analogous to an emitter inside an electromagnetic resonator (discussed in 2.1.3), the electric field of the plasmon polarization couples to the dipole moment of the dye molecules. The energy is coherently exchanged between the excitons and the gold nanorods by Rabi oscillations. Consequently, the plasmonic and excitonic modes “mix” and form two new states which will be denoted as *plexcitons* in the following. This process can be understood schematically as the hybridization of two atomic orbitals in a molecule where a bonding and an antibonding orbital are created at lower and higher energy, respectively [127]. Figure 4.4 can be considered here for a better understanding.

Furthermore, the extinction spectra of the other hybrid samples appear clearly different to a spectral superposition of bare rods and dye molecules. The extinction maximum of the plexciton at lower energy (*plex*) is always redshifted in comparison to the longitudinal plasmon, whereas the one at higher energy (*plex**) is blueshifted versus the dye. These deviations indicate strong mutual coupling. For all samples, the resonance of the transverse plasmon remains almost unaffected at about 2.4 eV. The radius of the transverse fringe of the gold nanorods is much larger than the longitudinal one. Therefore, the electric field on the surface is weaker when the transverse plasmon oscillation is excited. In addition to this, its quality factor is very low because of strong interband damping (see 2.1.1) and collective Rabi oscillations would rapidly dephase.

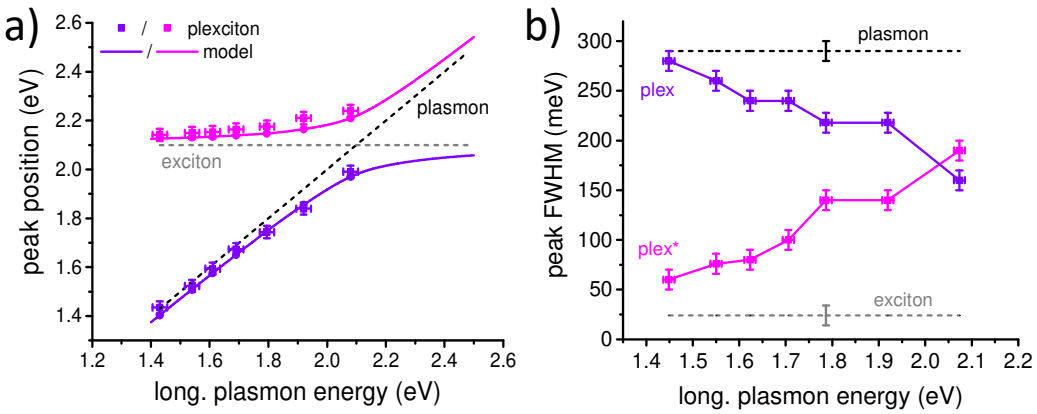

Figure 4.2: Analysis of linear absorption spectra a) Plexciton resonances versus longitudinal plasmon energy. Plexcitons are always separated by a spectral gap which is minimal when the plasmon energy is equal to the exciton transition of the dye at 2.1 eV. They spectrally repel from the uncoupled plasmon and dye (dotted curves). b) Resonance widths versus plasmon energy. Both plexcitons approach the linewidth of plasmon and exciton when the plasmon energy does not match with the exciton transition.

To analyse spectral effects of the coupling between the exciton in the dye and the longitudinal plasmon polarization of the gold nanorod, the resonance positions of both plexcitons (obtained from Figure 4.1c) are plotted versus the plasmon energy in Figure 4.2a. The error bars account that each resonance position can be determined only with non-zero uncertainty by taking the respective extinction maximum. Additionally, the resonance positions of the uncoupled plasmon and J-band resonance are plotted. The plasmon resonance (black, dashed graph) is a straight line through the origin, since it is

plotted versus itself. The uncoupled exciton in the dye (grey, dashed graph) is always located at 2.1 eV, the spectral position of the J-band independently of the plasmon energy and therefore gives a horizontal line.

The plot in Figure 4.2a can be understood similar to a dispersion relation for weak (dashed lines) and strong coupling (solid lines) like for an emitter in a cavity (see Figure 2.7b). In the weak coupling regime, the graphs of plasmon and dye would cross at 2.1 eV where they have the same energy. The interaction is too weak to have any spectral influences because the internal damping of the systems by spontaneous emission prevails (see 4.1.2). In this case, only the emission rates of the dye would be influenced by the electric field of the gold nanorods which act like antennas for the incoming electromagnetic field [36, 132].

In the present case, dye and plasmon polarization are in the strong coupling regime and the dispersion relations of the plexcitons in Figure 4.2a do not cross: Both branches spectrally "repel" from the uncoupled graphs. They reproduce the anticrossing behaviour discussed in 2.1.3. At 2.1 eV (i. e. plasmon resonance spectrally matches with exciton) the spectral gap between the plexcitons is minimal and corresponds to the extinction spectrum of the composite system with the gold nanorods of sample 7 (blue graph in Figure 4.1c). Here, the energy difference between *plex* and *plex** is about 260 meV and is equal to the Rabi splitting in equation (2.18). When the plasmon is spectrally detuned from the exciton, the influence of the coupling gets weaker. The energy of *plex** approaches to the exciton whereas *plex* converges to the plasmon dispersion relation. The corresponding extinction spectra in Figure 4.1c become clearly more and more similar to a superposition of the respective gold nanorods with the dye.

Since exciton and plasmon have rather different spectral linewidths (25 and ≈300 meV), the width of the plexcitons gives further insight to the coupling process. In Figure 4.2b, the FWHM of *plex* and *plex** are plotted versus the longitudinal plasmon resonance energy. In case of resonant coupling conditions (i. e. plasmon at 2.1 eV), their values are close to the arithmetic average of 160 meV. This is intuitively expected in analogy to the

emitter-cavity problem in 2.1.3: According to equation (2.20), plexcitons can be written as hybrid states comprised by a superposition of plasmonic $|pl\rangle$ and excitonic $|ex\rangle$ modes

$$\begin{aligned} |plex\rangle &= a|pl\rangle + b|ex\rangle, \\ |plex^*\rangle &= b|pl\rangle - a|ex\rangle, \end{aligned} \tag{4.1}$$

with $a^2 + b^2 = 1$. Both coefficients are equal if plasmon and exciton have the same energy (i. e. zero detuning) and consequently both plexcitonic states equally comprise plasmonic and excitonic modes [127]. When the longitudinal plasmon shifts to lower energies, the composition changes by $a > b$ and *plex/plex** get composed by more plasmonic/excitonic modes. Therefore, both the resonance positon (Figure 4.2a) and the FWHM (Figure 4.2b) of *plex/plex** approach to the uncoupled gold nanorod/dye transition.

4.1.2 Plexcitons as coupled Lorentz oscillators

The easy model based on equation (4.1) can qualitatively explain the dispersion relation of the plexcitons depicted in Figure 4.2. In the following section, a more compact model will be developed to understand and reproduce the optical behaviour quantitatively.

Hamiltonian of hybrid gold-dye particles

In the strong coupling regime, plasmon and exciton coherently exchange energy: The gold nanoparticle acts as resonator for the emitted radiation, until the radiation is subsequently reabsorbed by the dye molecules. The energy of the system oscillates periodically between the plasmon of the gold nanorod and the excitation of the dye with the Rabi frequency Ω_R. From the Rabi splitting of 260 meV, the oscillation period can be estimated according to equation (2.18): $T \approx \frac{h}{260\ \mathrm{meV}} = 16$ fs. Figure 4.3 sketches the Rabi oscillations: The polarizations of the gold nanorods and the dye are modulated with the Rabi frequency. The maximum of the envelope alternates between plasmon and exciton which resembles to classical coupled harmonic oscillators.

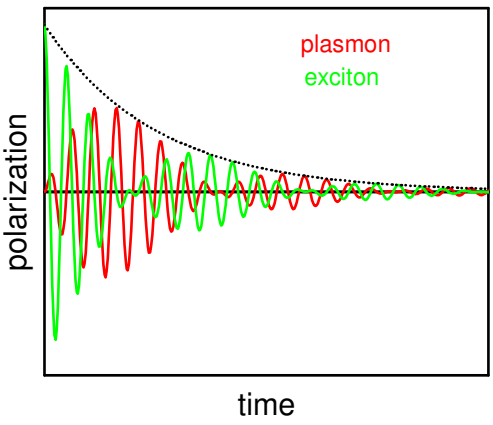

Figure 4.3: Rabi oscillations Polarizations are coherently exchanged between excitons in the dye molecules and the plasmon polarization of the gold nanorods.

To model the extinction spectra in Figure 4.1c, both plasmon and exciton were regarded as coupled Lorentz oscillators. With the plasmon resonance E_{pl} and the exciton transition E_{ex}, the Hamiltonian of a coupled system is given by:

$$H_0 = H_{\mathrm{pl}} + H_{\mathrm{ex}} + H_{\mathrm{int}} = \begin{pmatrix} E_{\mathrm{pl}} & 0 \\ 0 & E_{\mathrm{ex}} \end{pmatrix} + \begin{pmatrix} 0 & \hbar g \\ \hbar g & 0 \end{pmatrix}. \tag{4.2}$$

The coupling constant g which originates from the interaction H_{int} changes the eigenvalues of $H_{\mathrm{pl}} + H_{\mathrm{ex}}$ like a spring between two classical pendula. Although the motivation of two coupled harmonic oscillators seems rather trivial to describe plexciton resonances, equation (4.2) can be also obtained from the Jaynes-Cummings Hamiltonian in equation (2.15): The coupling constant is proportional to the n-photon Rabi frequency

$$2g = \Omega_n. \tag{4.3}$$

Since the plasmon polarization is comparable to an electromagnetic mode in a cavity, the resonance E_{pl} is equivalent to the photon energy E_{c} inside the cavity. However, the diagonal elements are still different to equation (2.15) because the definition of the energy scale is not the same: The state with zero energy in the model above is defined as the exciton in the ground state coexisting with all n non-absorbed photons in the cavity. If the corresponding baseline $(nE_{\mathrm{c}} - \frac{E_{\mathrm{ex}}}{2}) \cdot \mathbb{1}$ is subtracted from the Jaynes-Cummings

Hamiltonian (2.15), it coincides with the Hamiltonian of equation (4.2). The baseline of the Lorentz oscillator model was defined differently because absorption resonances correspond to energy differences of distinct states rather than absolute energy values.

Dephasing mechanisms of plexcitons

Additionally, the damping of the system has to be considered. In this thesis, the damping was regarded analogous to classical coupled harmonic oscillators, where an imaginary damping term is added to the Hamiltonian:

$$H = H_0 - i\frac{1}{2}\Gamma = \begin{pmatrix} E_{\mathrm{pl}} & \hbar g \\ \hbar g & E_{\mathrm{ex}} \end{pmatrix} - i\frac{1}{2}\begin{pmatrix} \Gamma_{\mathrm{pl}} & \Gamma_{\mathrm{XP}} \\ \Gamma_{\mathrm{XP}} & \Gamma_{\mathrm{ex}} \end{pmatrix}. \tag{4.4}$$

The damping comprises all processes which destroy coherent polarizations and their periodic exchange. These are on the one hand the dephasing of plasmon and exciton (equivalent to the respective homogenous linewidths Γ_{pl} and Γ_{ex}). On the other hand, additional losses can occur by non-perfect reabsorption of the emitted radiation which is expressed with the parameter Γ_{XP}. In the classical case of two coupled pendula, it is equivalent to the friction of the coupling string.

The by far fastest dephasing occurs for the plasmon polarization which can be estimated from the Mie calculations for the homogenous linewidth (see 4.1.1): $T_{2,\mathrm{pl}} = \frac{2\hbar}{\Gamma_{\mathrm{pl}}} =$ 8…13 fs. Contributions from the dye molecules are much slower. Even if the FWHM γ_{ex} in the extinction spectrum (see Figure 4.1b) is assumed as upper boundary for the homogenous linewidth, a significant longer dephasing time is obtained: $T_{2,\mathrm{ex}} \geq \frac{2\hbar}{\gamma_{\mathrm{ex}}} =$110 fs. Hence, errors on the estimation of Γ_{ex} has negligible effects. Furthermore, it is not unsubstantiated that $\gamma_{ex} \approx \Gamma_{\mathrm{ex}}$ because J-aggregation diminishes inhomogeneous broadening (see 2.1.2). The eigenenergies of the Hamiltonian in equation (4.4) are:

$$\grave{E}_{\mathrm{plex/plex^*}} = \frac{1}{2}\left(\grave{E}_{\mathrm{pl}} + \grave{E}_{\mathrm{ex}} \pm \sqrt{\left(\grave{E}_{\mathrm{pl}} - \grave{E}_{\mathrm{ex}}\right)^2 + 4\grave{g}^2}\right). \tag{4.5}$$

Here, the complex energy $\grave{E} = E - i\frac{1}{2}\Gamma$ is comprised of the resonance position E and the homogenous linewidth Γ.

Modelling of the linear extinction spectra

The homogenous linewidth Γ_{pl} of the plasmon is estimated from the FWHM γ_{pl} in the extinction spectra (Figure 4.1a) and the Mie calculations. Even though Γ_{pl} was not calculated for every sample, the inhomogeneous broadening by E_{pl} ±100 meV was assumed to be constant for every sample which is supported by the calculations in 4.1.1. This allows an estimation of Γ_{pl} from γ_{pl} according to [133] when a Gauss profile is assumed for the inhomogeneous broadening. Since $\grave{E}_{\mathrm{pl}}$ and $\grave{E}_{\mathrm{ex}}$ are obtained as fixed parameters, only the coupling strength $\grave{g} = \hbar g - i\frac{1}{2}\Gamma_{\mathrm{XP}}$ is fitted to reproduce the extinction spectra of all samples. An overview of the coupling model with the respective parameters is shown in Figure 4.4.

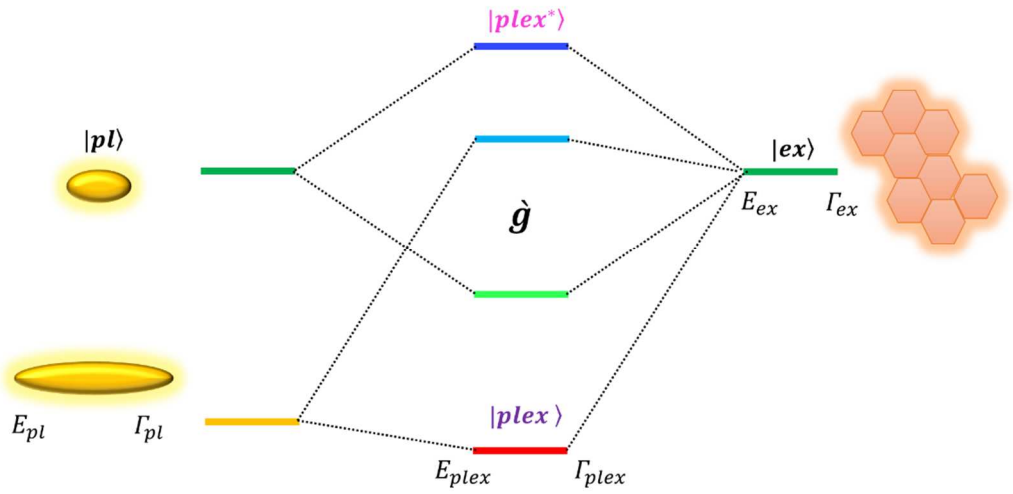

Figure 4.4: Hybridisation model of plexcitons: The longitudinal plasmon resonance of the gold nanorods couples with excitons in the dye. $\grave{g}$ is the coupling constant, *E* and *Γ* the spectral position and damping of the respective resonances. The plexcitons are the coupled resonances and can be understood as hybrid states between plasmon and exciton, similar to bonding and antibonding molecular orbitals.

The real part of $\grave{E}_{\mathrm{plex}}$ in equation (4.5) gives the resonance position E_{plex} and the imaginary part is half of the homogenous linewidth Γ_{plex} of each plexciton. However, the

inhomogeneous broadening δ_{plex} has to be accounted to reproduce the FWHM γ_{plex} which is actually observed in the extinction spectra of Figure 4.1c. Since the mechanism of J-aggregation reduces inhomogeneous effects of the dye molecules, only fluctuations of the plasmon resonance were regarded by $E_{\mathrm{pl}} \pm 100$ meV (see 4.1.1). Due to the statistic variations of the plasmon energy, plexciton resonances occur at $E_{\mathrm{plex}} \pm \delta_{\mathrm{plex}}$. The inhomogeneous spread δ_{plex} was estimated by: $\delta_{\mathrm{plex}} \approx E_{\mathrm{plex}}\left(E_{\mathrm{pl}} + 100\ \mathrm{meV}\right) - E_{\mathrm{plex}}(E_{\mathrm{pl}})$. Under the assumption of a Gaussian distribution for the inhomogenous broadening, the total FWHM of each plexciton γ_{plex} can be calculated by using the approximation in [133].

Even though Voight profiles with a homogenous width Γ_{plex} and an inhomogeneous width $2\delta_{plex}$ would be the exact mathematical description, Lorentz profiles were chosen to model the contribution of the plexcitons in the optical density OD of the gold-dye composite systems in Figure 4.1c:

$$OD(E) = \mathrm{Im}\left(\frac{f_{\mathrm{plex}}}{E - E_{\mathrm{plex}} - i\frac{\gamma_{\mathrm{plex}}}{2}}\right) + \mathrm{Im}\left(\frac{f_{\mathrm{plex}^*}}{E - E_{\mathrm{plex}^*} - i\frac{\gamma_{\mathrm{plex}^*}}{2}}\right) + \mathrm{baseline}. \qquad (4.6)$$

The deviations of both functions are marginal when the FWHM γ_{plex} is calculated according to the above procedure. The baseline only accounts the transverse plasmon resonance and the interband absorption of the gold nanorods for $E > 2.38$ eV. A Lorentz profile and a function proportional to $\sqrt{E - 2.38}$ (because of three-dimensional particles, see 2.2.1) was chosen to simulate the baseline. Importantly, the spectral region of both plexcitons is nearly unaffected by the baseline which allows a very good comparison between the experimental data and the model. The ratio of the oscillator strengths $f_{\mathrm{plex}}/f_{\mathrm{plex}^*}$ is estimated from the eigenstates of the Hamiltonian in equation (4.4). The parameter $\dot{g}$ was fitted until best agreement with all curves was achieved. The optimal value was found to be: $\dot{g} = 0.14\ \mathrm{eV} - i \cdot 0.012\ \mathrm{eV}$.

Even though the coupled Lorentz oscillator model is very simple, the experimental data are in very good agreement to the simulated curves (dashed in Figure 4.1c) for every single

sample. This is remarkable because only two parameters (the real and imaginary part of $\grave{g}$) are necessary to reproduce the spectral shape of all 14 plexciton resonances. Since every resonance has a width, centre and height $14 \cdot 3 = 42$ individual parameters can be explained on the basis of only two. The result shows that despite of different morphologies, $\grave{g}$ is similar for all samples. Physically, this might be correlated to the fact that the lateral dimensions of the gold nanorods are very similar. Therefore, it is realistic to consider equal amount of dye molecules in the vicinity of both tips where the electric field of the plasmon polarization is strongest.

The dispersion relations for $E_{\mathrm{plex}}/E_{\mathrm{plex}^*}$ (obtained from the model) are plotted in Figure 4.2a as solid curves. All experimental values are within the measurement error. In Figure 4.2b, it was found experimentally that the FWHM γ_{plex^*} is slightly larger than γ_{plex} when the plasmon resonance is at 2.1 eV. This observation is a direct evidence for the damping term Γ_{XP} in equation (4.4). In this case the plasmon is in resonance to the exciton, i. e. $E_{\mathrm{pl}} = E_{\mathrm{ex}}$ and the homogenous linewidth of both plexcitons is equal to:

$$\Gamma_{\mathrm{plex/plex}^*} = \frac{1}{2}\left(\Gamma_{\mathrm{pl}} + \Gamma_{\mathrm{ex}}\right) \pm \mathrm{Im}\left(\sqrt{-\left(\Gamma_{\mathrm{pl}} - \Gamma_{\mathrm{ex}}\right)^2 + 4\grave{g}^2}\right). \tag{4.7}$$

The respective values of $\Gamma_{\mathrm{pl}} = 160$ meV and $\Gamma_{\mathrm{ex}} = 25$ meV give: $\Gamma_{\mathrm{plex/plex}^*} = 92.5\ \mathrm{meV} \pm \mathrm{Im}\left(\sqrt{-(135\ \mathrm{meV})^2 + 4\grave{g}^2}\right)$. If $\grave{g}$ would be a real number the expression under the square root wold be positive, since the real part of $\grave{g}$ is in the range of 130 meV (according to the Rabi splitting of 260 meV). Consequently, the linewidth of both plexcitons would be equal which is in contradiction to the experimental finding. Due to Γ_{XP}, the imaginary part of the square root is different from zero. Therefore, the homogenous linewidth of both plexcitons is different in agreement to the experimental finding. A similar result has been obtained and explained similarly for a gold grating coated with a J-aggregated dye [134].

The chapter has shown that a simple coupled Lorentz oscillator model can precisely reproduce the linear extinction spectra of gold nanorods coated with J-aggregated dye molecules. In the next chapter, it will be addressed in how far it is also applicable to describe the nonlinear optical behaviour.

4.2 Nonlinear optical behaviour of plasmons and excitons

Nonlinear spectroscopy is a versatile tool to investigate spectral changes and relaxation dynamics upon excitation. This will be used to obtain more experimental evidence that plexcitons are hybrid states comprising plasmonic and excitonic modes. The first approach is an experimental differentiation between plasmonic and excitonic behaviour which is done in this section. Femtosecond transient absorption spectroscopy was found to be a suitable method to distinguish both: Upon excitation, the homogenous linewidth of plasmons in gold nanorods enhances and relaxes within three to five picoseconds. By contrast to this, the J-band of the dye molecules bleaches and decays on a femtosecond timescale. These understandings are essential to discriminate plasmons and excitons in the hybrid material (see 4.3).

4.2.1 Nonlinear optical behaviour of gold nanorods

Figure 4.5a shows transient absorption spectra of bare gold nanorods with an aspect ratio of 2.5 (sample 6) for various delay times after excitation. The excitation pulse was in resonance with the transverse plasmon (at 2.4 eV). For any delay time, the differential absorption is negative in the spectral range of both plasmon resonances. Both are merged into regions with $\Delta OD > 0$. In Figure 4.5b, the time traces at two different spectral positions (marked in Figure 4.5a with a sphere and a circle) are plotted. All of them show the same trend: The signal rises to a maximum within about 500 fs (i). The subsequent decay can be distinguished in a fast initial (ii) and a slow final regime (iii). After 8 ps the signal has dropped down to 40 % of its maximum. However, 5% still remain after 300 ps.

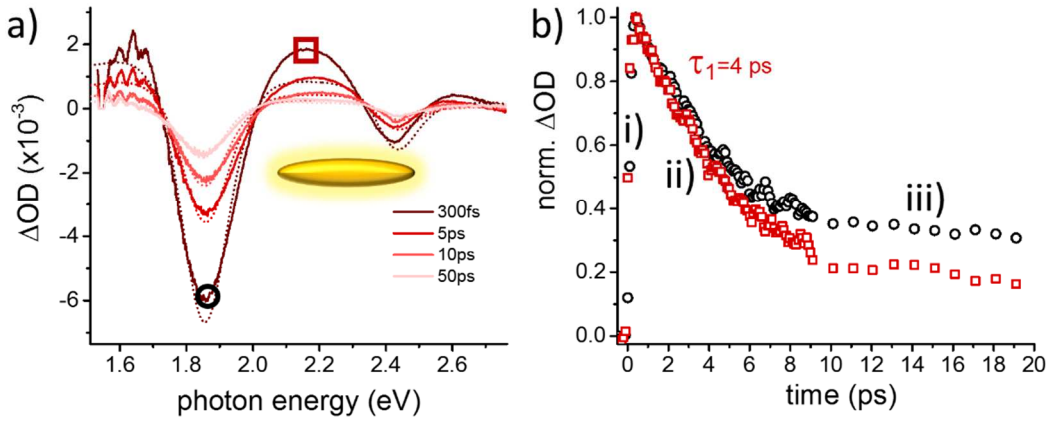

Figure 4.5: Transient absorption of bare gold nanorods a) The experimental/modelled spectra are plotted as solid/dotted graphs for different delay times between pump and probe pulse. Circle and square mark the spectral positions of the normalized transients shown in b). After an initial rise i) the relaxation occurs in a fast ii) and slow step iii) which is associated with the temperature of the gold nanorods.

The dynamics of both curves in Figure 4.5b are rather similar which suggests that all differential changes are caused by one single process. According to equation (2.11), each plasmon resonance can be approximated with a Lorentz profile. Upon excitation, three different changes ("nonlinearities") can occur: As schemed in Figure 4.6a, the oscillator strength f_i, the resonance position E_i and the homogenous linewidth Γ_i can change. All the mentioned parameters were used to reproduce the experimental transient absorption spectra in Figure 4.5a by the difference of two Lorentz functions with the spectral linewidth γ_i (comprising homogeneous and inhomogeneous broadening as described in 4.1.1):

$$\Delta OD(E) = \sum_{i\in\{LO,TA\}} \mathrm{Im}\left(\frac{f_i}{E - E_i - i\left(\frac{\gamma_i}{2}\right)} - \frac{f_{i_0}}{E - E_{i_0} - i\left(\frac{\gamma_{i_0}}{2}\right)}\right). \tag{4.8}$$

The index i labels the respective parameters for the longitudinal (LO) and transverse (TA) plasmon resonance. The stationary values obtained from the linear extinction spectrum in Figure 4.1a (green curve) have the index i_0. The fitting was done with *Mathematica 10.2*. A detailed description of the procedure with the script code is given in the appendix of this thesis.

The experimental data can be reproduced by almost exclusively increasing the FWHM of both plasmon resonances as schemed in Figure 4.6b. Changes to both other fitting parameters are negligible: $\frac{\Delta f/f}{\Delta\gamma/\gamma} < 1\ \%$, $\frac{\Delta E/E}{\Delta\gamma/\gamma} < 0.5\ \%$. The fits are plotted in Figure 4.5a as dotted curves. Deviations from the experimental data in the regions with $\Delta OD > 0$ occur because of the inhomogeneous broadening.

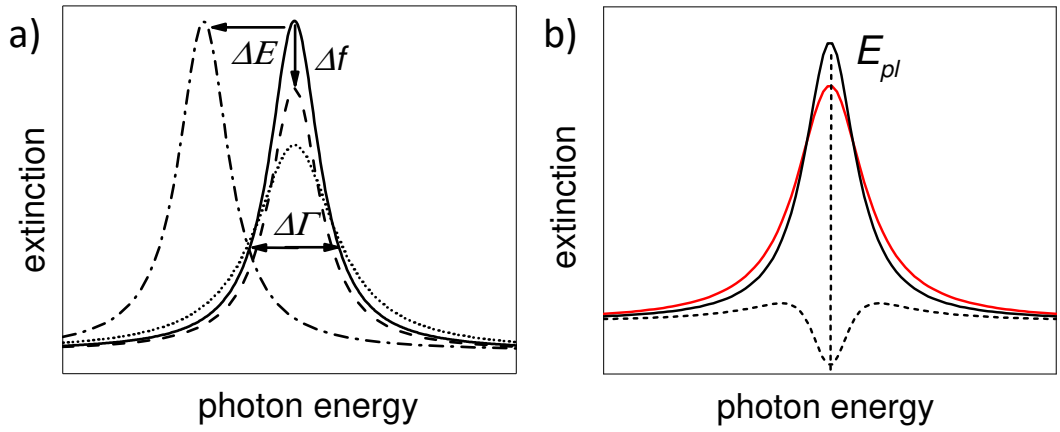

Figure 4.6: Model for nonlinear optical behaviour a) Amplitude, central energy and width of a Lorentz resonance can change upon excitation. b) The lindewidth of plasmon resonances in gold nanorods enhances upon excitation which gives the characteristic differential absorption spectrum (dashed curve).

The results are attributed to an increase of the homogeneous linewidth: The excitation pulse excites the transverse plasmon resonance. As explained in 2.1.1, the non-radiative decay strongly heats up the electron gas. The electron-electron scattering rate enhances and plasmons which are excited by the probe pulse after a delay time dephase faster. The rise time of the nonlinear signal (Figure 4.5b-i) reflects the initial dissipation of the excitation energy into the electron gas. Subsequently, the misbalance with the lattice temperature is levelled by cooling (ii). The electron-electron scattering rate diminishes and the homogenous linewidth of the plasmon relaxes from its peak value. Finally, the entire crystal exchanges internal energy with the surrounding medium (iii). From the experimental data, the time scales of both dissipation processes (ii) and (iii) can be estimated. Since the temperature of an object decreases exponentially in a colder environment [135], a biexponential decay model was applied. The time constants are 4 and 230 ps.

4.2.2 Nonlinear optical behaviour of dye molecules

The transient absorption spectra of the J-aggregated dye molecules are quite different as depicted in Figure 4.7a for an excitation pulse at 2.1 eV (resonant to the J-band) and a photon flux of $5 \cdot 10^{13}$ cm^{-2}: A negative signal occurs for energies <2.14 eV with a minimum around 2.1 eV, the spectral position of the J-band. For higher photon energies, the signal is positive with a maximum at 2.17 eV. The transients are very similar for minimum and maximum (see Figure 4.7b): The differential absorption rises within 300 fs and then decays to 50% of its maximal amplitude within 1 ps.

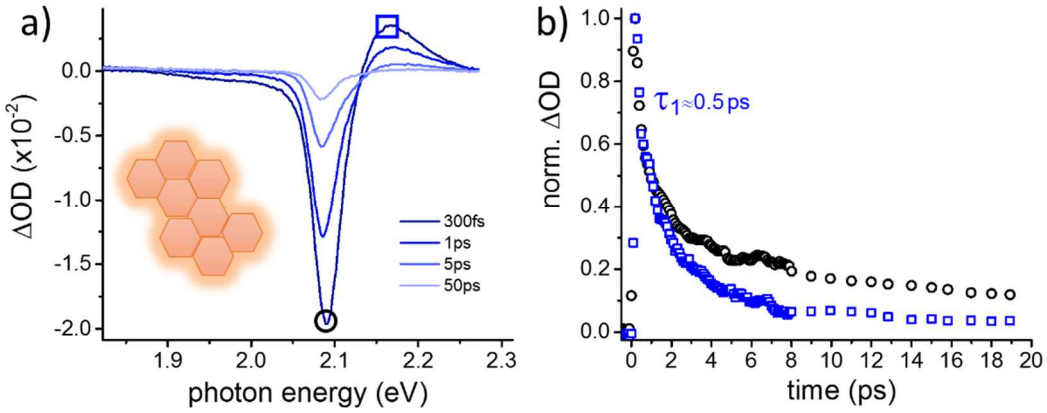

Figure 4.7: Transient absorption of bare dye molecules a) Differential absorption spectra for different delay times. Circle and sphere illustrate the spectral positions of the respective normalized transients in b).

The equivalent time dynamics of both spectral signatures approve that they are caused by the same nonlinear effect. Photons of the excitation pulse create excitons in individual dye molecules. I. e. an electron and a hole occupy the first excited state and fill the phase space. Because of the Pauli principle for fermions, further excitations (generated by the probe pulse) must have different quantum numbers ("Pauli blocking"). Therefore, the transition probability for the first excited state reduces and the transmission in the corresponding spectral region increases ("bleaching") [93]. Additionally, a two-exciton state can be created in J-aggregated cyanine dyes: A second exciton is excited by the probe pulse at higher energy within the lifetime of the first one (created by the pump pulse). Consequently, the differential absorption is enhanced for photon energies larger

than 2.14 eV [136]. The relaxation of the differential absorption allows an observation of the exciton lifetime: The initial subpicosecond decay is very striking in comparison to the cooling dynamics of the gold nanorods which are four to five times slower (compare to Figure 4.5b). Exciton-exciton annihilation for similar J-aggregates was found to be responsible for the fast initial dynamics [137].

Both the spectral and transient signatures enable a clear distinction between plasmonic and excitonic behaviour under nonlinear excitation. The homogenous linewidth of plasmon resonances in gold nanorods enhances, whereas the transition band of the dye bleaches. For gold nanorods, the initial recovery of the transient absorption is due to thermalisation of the hot electron gas with the lattice within 4 ps. By contrast to that, the initial relaxation of the dye due to exciton recombination is faster than 1 ps.

4.3 Nonlinear optical behaviour of plexcitons

With the knowledge about the nonlinear signatures of the bare subsystems it is possible to analyse the plexcitons in the gold-dye hybrid particles. To differentiate between purely plasmonic and excitonic modes, two experiments were conducted: First, mainly plasmonic modes were excited by the pump pulse to analyse the influence of respective signatures. In the second experiment, the plexcitons were directly excited. All experimental data can be reproduced and explained on the basis of the coupled Lorentz oscillator model which was developed in 4.1.2.

4.3.1 Plasmonic influences in the strong coupling regime

In the first experiment, the excitation laser pulse was tuned in resonance with the transverse plasmon which is at ≈ 2.44 eV for every sample (sketched in Figure 4.8a). A photon flux of 10^{13}–10^{14} cm^{-2} comparable to the previous experiments was adjusted. The differential absorption spectra of all samples are shown in Figure 4.8b for a delay of 300 fs between pump and probe pulse. Minima with negative differential absorption are observed at the spectral positions of both plexciton resonances and the transverse plasmon. A positive signal is found for photon energies lower than both plexcitons or higher than the transverse plasmon. For samples with significant spectral detuning between plasmon and exciton, an interval with $\Delta OD > 0$ appears within the gap between *plex* and *plex**.

Results and analysis of experiment

To model the experimental data, the difference of two absorption spectra according to equation (4.6) is applied:

$$\Delta OD(E) = \sum_{i\in\{plex,plex^*,TA\}} \mathrm{Im}\left(\frac{f_i}{E - E_i - i\left(\frac{\gamma_i}{2}\right)} - \frac{f_{i_0}}{E - E_{i_0} - i\left(\frac{\gamma_{i_0}}{2}\right)}\right). \qquad (4.9)$$

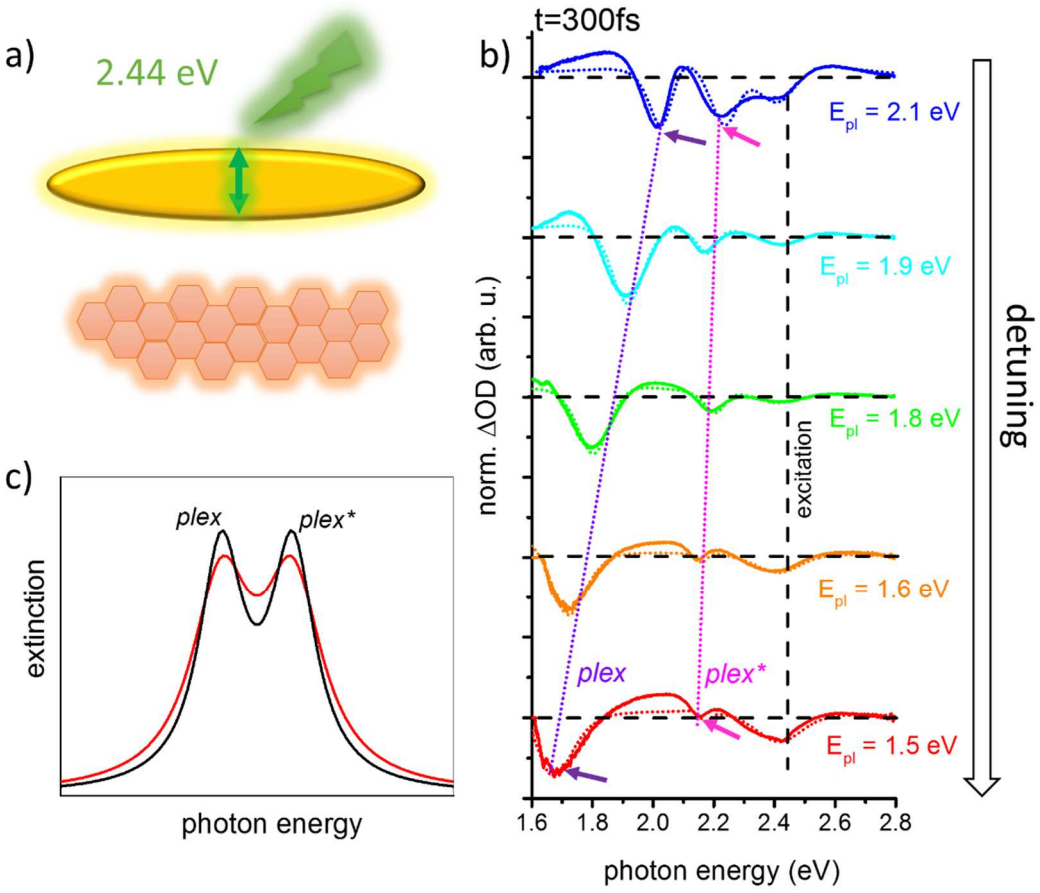

Figure 4.8: Nonlinear optical behaviour of plexcitons upon excitation at 2.44 eV a) The excitation laser pulse is in resonance with the transverse plasmon. b) Experimental (solid) and modelled (dotted) transient absorption spectra with a delay of 300 fs between pump and probe pulse for different samples. Arrows indicate spectral positions of the transients in Figure 4.9. c) Scheme of nonlinear process: The linewidth of both plexcitons increases upon excitation.

The stationary values for f_{i_0}, E_{i_0} and γ_{i_0} were taken from the linear absorption spectra in Figure 4.1c. With this easy model it is possible to reproduce all curves for any delay time between pump and probe pulse by increasing the linewidth γ_i of all three resonances (see dotted graphs in Figure 4.8b). Negligible bleaching/induced absorption or spectral shifts are required as additional parameters: $\frac{\Delta f/f}{\Delta\gamma/\gamma} < 4\,\%$, $\frac{\Delta E/E}{\Delta\gamma/\gamma} < 2\,\%$. These observations strongly resemble the nonlinear optical behaviour of the uncoupled gold nanorods (see section 4.2.1). Some mismatch between the modelled curves and the experimental data occurs in the regions with positive differential absorption. This can be attributed to the inhomogeneous broadening of all resonances.

Although the structures are in the strong coupling regime (with plasmon/exciton hybridization), the experiment manipulates solely the plasmonic modes. Since the transverse plasmon resonance (which has been excited by the pump pulse) does not play a role in the coupling process, it remains unaffected from hybridisation effects. Therefore, the excited transverse plasmon decays and subsequently heats up the electron gas of the entire gold nanorod. Even though the longitudinal plasmon resonance is not (or only marginally) excited, its dephasing rate still enhances mainly due to electron-electron collisions in the hot electron gas (see 2.1.1 and 4.2). Consequently, the exciton in the dye couples with a spectrally broader plasmon resonance (red graph in Figure 4.8c) as long as the crystal temperature is out of its thermal equilibrium. Because of the enhanced dephasing rate of the longitudinal plasmon, the Rabi oscillations with the dye molecules (which are excited by the probe pulse after the delay τ) are stronger damped. Therefore, the homogenous linewidth of both plexcitons enhances by $\Delta\Gamma_{\mathrm{plex/plex^*}}(\tau)$ and the respective FWHM $\Delta\gamma_{\mathrm{plex/plex^*}}(\tau)$ increases. Here, it should be mentioned that a coherent effect is measured although the dephasing time and the oscillation period are in the range of about 16 fs and cannot be resolved with the experimental setup.

Quantitative analysis

Effects of the nonlinear signatures of plasmonic modes can be described on the basis of the coupled oscillator model in 4.1.2: After excitation, the complex eigenenergy of the plasmon changes: $\grave{E}_{\mathrm{pl}} \rightarrow \grave{E}^*_{\mathrm{pl}} = \grave{E}_{\mathrm{pl}} - i\frac{1}{2}\Delta\Gamma_{\mathrm{pl}}(\tau)$. Here, $\Delta\Gamma_{\mathrm{pl}}(\tau)$ is the increase of the homogenous linewidth of the longitudinal plasmon resonance (see 4.2.1). According to equation (4.5), the eigenenergies of both plexcitons are affected by:

$$\grave{E}^*_{\mathrm{plex/plex^*}} = \frac{1}{2}\left(\grave{E}_{\mathrm{pl}} - \frac{i\Delta\Gamma_{\mathrm{pl}}(\tau)}{2} + \grave{E}_{\mathrm{ex}} \pm \sqrt{\left(\grave{E}_{\mathrm{pl}} - \frac{i\Delta\Gamma_{\mathrm{pl}}(\tau)}{2} - \grave{E}_{\mathrm{ex}}\right)^2 + 4\grave{g}^2}\right). \qquad (4.10)$$

The increase of the homogenous linewidth of both plexcitons can be calculated by $\Delta\Gamma_{\mathrm{plex/plex^*}} = -2\mathrm{Im}\left(\grave{E}^*_{\mathrm{plex/plex^*}} - \grave{E}_{\mathrm{plex/plex^*}}\right) > 0$. Here, it follows that:

$$\Delta\Gamma_{\mathrm{plex}}(\tau) + \Delta\Gamma_{\mathrm{plex}^*}(\tau) = \Delta\Gamma_{\mathrm{pl}}\,(\tau). \tag{4.11}$$

In other words, the homogenous broadening of the plasmon $\Delta\Gamma_{\mathrm{pl}}(\tau)$ upon excitation causes a spectral broadening $\Delta\Gamma_{\mathrm{plex/plex}^*}(\tau)$ of both plexcitons. In case of resonant coupling conditions, it can be calculated that $\Delta\Gamma_{\mathrm{plex}} \approx \Delta\Gamma_{\mathrm{plex}^*}$. Consequently, both hybrid resonances are equally influenced by the nonlinearity of the plasmon. This can be also seen in the transient traces (see Figure 4.9a) taken at the respective minima of the differential absorption (marked with arrows on the blue graph in Figure 4.8b).

Both curves are nearly similar: Initially the signals rise within 500 fs and relax to 50% of the maximal value within 3-4 ps. Along with the subsequent decay on a time scale of hundreds of picoseconds, the dynamics resemble to the transient absorption of bare gold nanorods (compare to Figure 4.5b). This proves that the non-linear optical behaviour is dominated by $\Delta\Gamma_{\mathrm{plex/plex}^*}(\tau)$ according to equations (4.10) and (4.11). In presence of spectral detuning between the plasmon and the exciton, the transients of both plexcitons start to differ. This is exemplary shown for a detuning of 600 meV (red graph in Figure 4.8b and spectral positions of the respective transients are marked with arrows) in Figure 4.9b: While *plex* underlies similar dynamics as discussed before, the nonlinearity of *plex** rises within 200 fs and recovers to 50 % within only 1 ps which is similar to the relaxation of the pure dye molecules (compare Figure 4.7b). A biexponential decay model is used to reproduce quantitatively the dynamics not only for the two present samples in Figure 4.9a and b, but also for intermediate spectral detunings. The initial decay time is plotted for various plasmon energies in Figure 4.9c. The arrows mark the samples which are shown in Figure 4.9a and b.

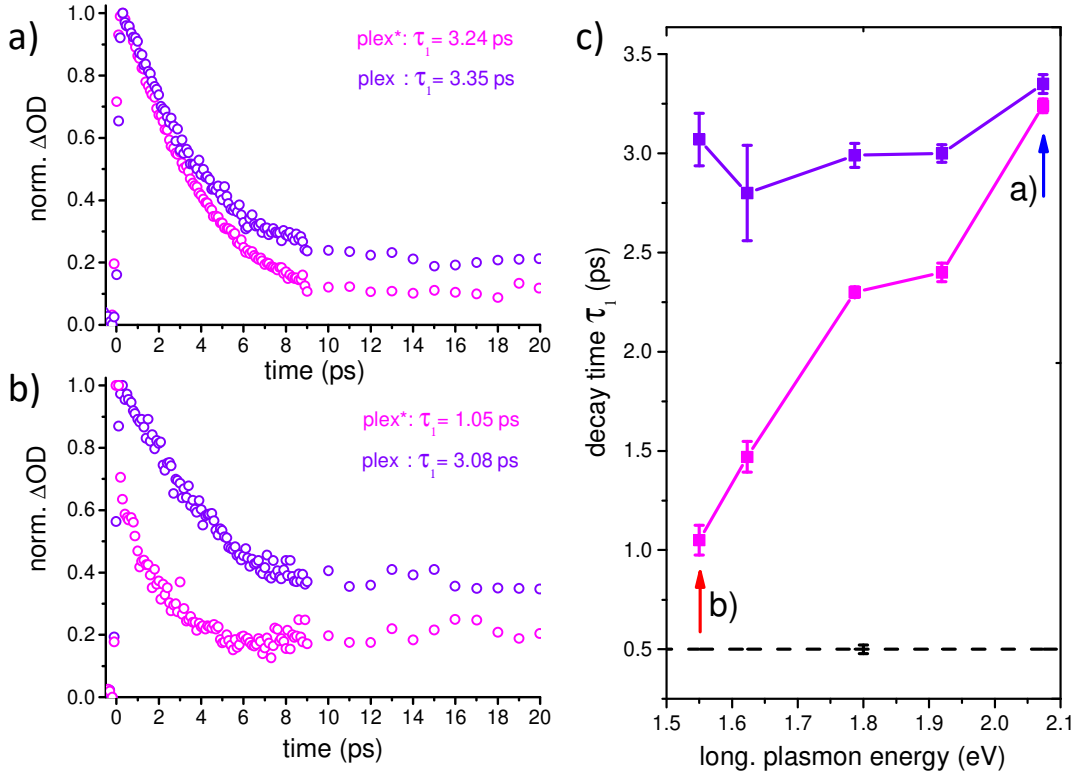

Figure 4.9: Transients of plexcitons a) Resonantly coupled case: both plexcitons relax within a similar time scale like gold nanorods. b) Non-resonantly coupled case: *plex** recovers faster which resembles the exciton dynamics. c) Initial decay time of both plexcitons (obtained from biexponential fitting) for different plasmon energies. The arrows show the data which is presented in a) and b).

The relaxation of *plex* always remains at approximately 3 ps which corresponds to the initial thermalisation of the electron gas in gold nanorods. By contrast to that, *plex** recovers the faster the lower the plasmon energy gets and approaches the time scale of the exciton recombination on the dye (dashed curve). This result is a very interesting experimental finding about the nonlinear optical behaviour of plexcitons. Qualitatively, at least the decay dynamics of *plex** can be understood on the basis of exciton-plasmon hybridization according to equation (4.1): Both plexcitons equally consist of plasmonic and excitonic modes if the plasmon resonance matches with the dye transition at 2.1 eV. Therefore, similar optical behaviour is expected. However, *plex** comprises more excitonic modes when the plasmon shifts to lower energies and relaxation dynamics

similar to the dye are expected. Although these claims are in agreement with the experimental observations, this simplified picture cannot explain the full findings.

With the coupled oscillator model, it is possible to explain the observations in Figure 4.9c quantitatively. According to equation (4.10), the nonlinearity of plexcitons is mainly an increase of the homogenous linewidth which is induced and governed by the hot gold nanorods. From the same equation, it follows that $\Delta\Gamma_{\mathrm{plex}} > \Delta\Gamma_{\mathrm{plex}^*}$ when $E_{\mathrm{ex}} > E_{\mathrm{pl}}$. According to equation (4.11), the nonlinearity $\Delta\Gamma_{\mathrm{pl}}\ (\tau)$ has less influences on *plex** when the plasmon resonance is tuned to lower energies. However, the excitation pulse at 2.44 eV does not only excite the transverse plasmon but also has some little overlap with *plex** itself. When $\Delta\Gamma_{\mathrm{plex}^*}$ becomes smaller, other nonlinearities with a shorter lifetime can be observed even though they are too weak for proper modelling. To address their nature, a second set of experiments was done.

4.3.2 Excitonic influences in the strong coupling regime

In the following experiment, *plex** was directly excited by tuning the pump pulse to 2.18 eV (570 nm). Figure 4.10a shows the differential absorption spectra for a time delay of 200 fs and 1 ps between pump and probe pulse for the resonantly coupled gold-dye composite system (i. e. plasmon resonance at 2.1 eV). The spectrum after 1 ps looks similar to the one obtained in Figure 4.8b (blue graph), where the excitation pulse coincided with the transverse plasmon. Indeed, the respective spectrum can be reproduced by solely increasing the homogenous linewidth of all three resonances similar to the procedure described in 4.3.1. The modelled graph (dotted bright blue curve in Figure 4.10a) agrees well with the experimental data. This shows, that the non-linear optical behaviour in this time range is governed by the hot gold nanords.

However, for short delay times the shape of the differential absorption spectrum changes completely (dark blue solid curve): A sharp peak with positive differential absorption arises at 2.1 eV. This was found to be the centre of the spectral gap between both plexcitons (see 4.1.1). The transients at 2.0 and 2.2 eV (arrows in Figure 4.10a) are plotted

in Figure 4.10b. Subpicosecond dynamics can be observed. To identify the nonlinearity which is causing this effect, the previous model of equation (4.9) is applied. In addition to broadening $\Delta\gamma_{\mathrm{plex/plex^*}}$, both plexcitons show a spectral shift within the first picosecond, i. e. $E_{\mathrm{plex/plex^*}} \rightarrow E_{\mathrm{plex/plex^*}} + \Delta E_{\mathrm{plex/plex^*}}$.

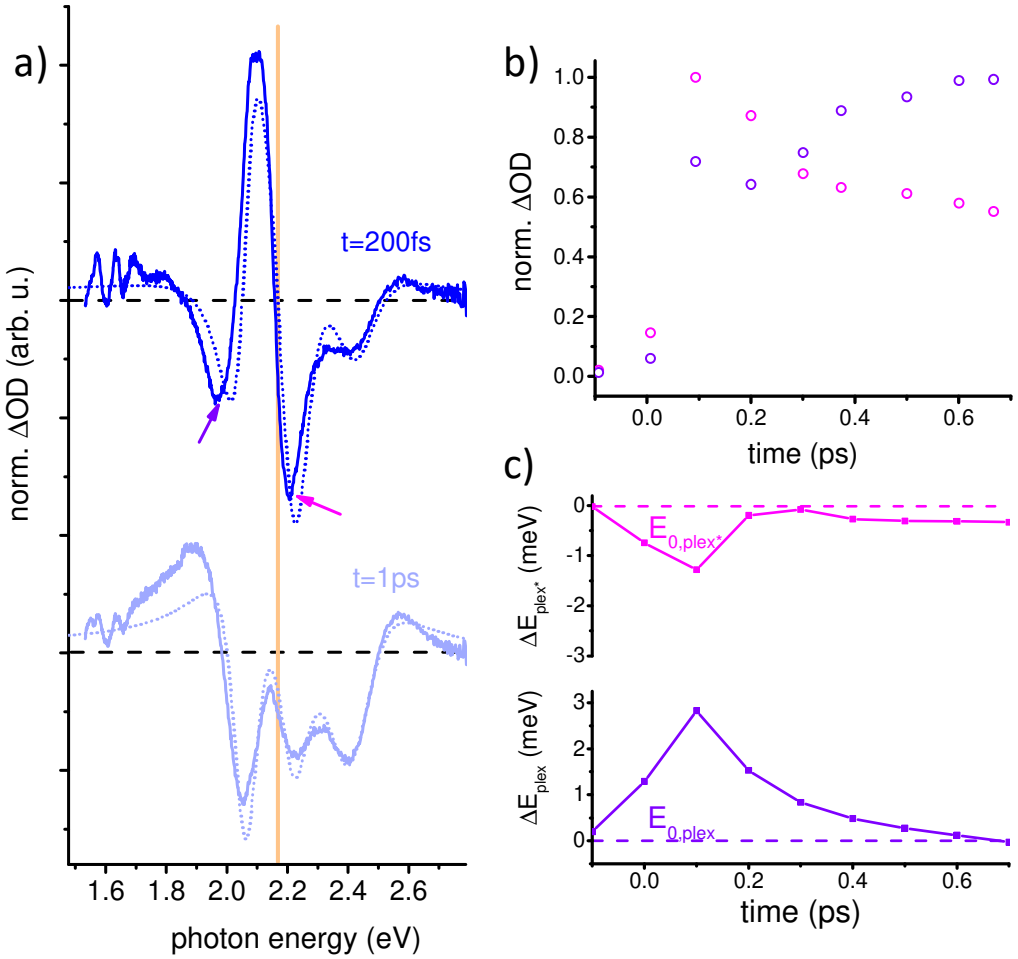

Figure 4.10: Nonlinear optical behaviour of plexcitons upon excitation at 2.18 eV a) Differential absorption spectra for sample with plasmon in resonance to the exciton at two different delay times. Arrows mark the spectral position of the transients in b). c) Nonlinearity *ΔE* versus delay time.

The modelled values of ΔE_{plex} and $\Delta E_{\mathrm{plex^*}}$ are plotted in Figure 4.10c for different delay times. *plex* shifts to higher energies and vice versa for *plex**. All in all, the Rabi splitting reduces by up to 4 meV within the first picosecond after excitation. This is sketched in Figure 4.11a: Since both plexciton resonances shift inside the spectral gap, a positive

differential absorption with two peaks is observed in this region. Both peaks can be observed more clearly for the other samples, where the plasmon resonance is at lower energy (see Figure 4.11b). However, the effect gets weaker for increased detuning between plasmon and exciton.

From equation (4.5), it follows that the spectral gap between both plexcitons $E_{\mathrm{plex}^*} - E_{\mathrm{plex}}$ is influenced by the real part of the coupling constant $\dot{g}$. In the following, a mechanism leading to a reduction of the latter is suggested: When plexcitons are excited by the pump pulse, coherent Rabi oscillations occur as described in 4.1.2. Although the coherence dephases within about 20 fs, an (incoherent) exciton population remains in the dye molecules. It was found that the nonlinear response of excitons (see 4.2) is a reduced absorption of the J-band due to phase space filling.

Consequently, less excitons in the dye molecules can coherently emit and reabsorb energy for any further excitations created by the probe pulse within the exciton lifetime. According to equation (2.16), the Rabi frequency Ω_n depends on the number of photons in an electromagnetic resonator by $\sim\sqrt{n+1}$. Since every exciton exchanges one photon with the gold nanorod, n is equivalent to the number of excitons participating in the coupling process. As long as an incoherent exciton population $N(\tau)$ is present in the dye, any further Rabi oscillations (excited by the probe pulse after the delay τ) occur only with $n - N(\tau)$ emitters. Therefore, the respective frequency diminishes and the Rabi splitting reduces according to equation (2.18). From equation (4.3), it follows that the Rabi frequency is proportional to the coupling constant. When the coupling constant reduces, both plexciton resonances E_{plex} and E_{plex^*} shift closer to E_{pl} and E_{ex}, respectively. The effect is present as long as incoherent excitons N populate the dye. Since excitons in the dye relax within about one picosecond (compare with Figure 4.7b), the coupling constant reduces for a comparable lifetime and gives the observed non-linear signatures. Similar phenomena have been found for a gold grating coated with a J-aggregated dye [138].

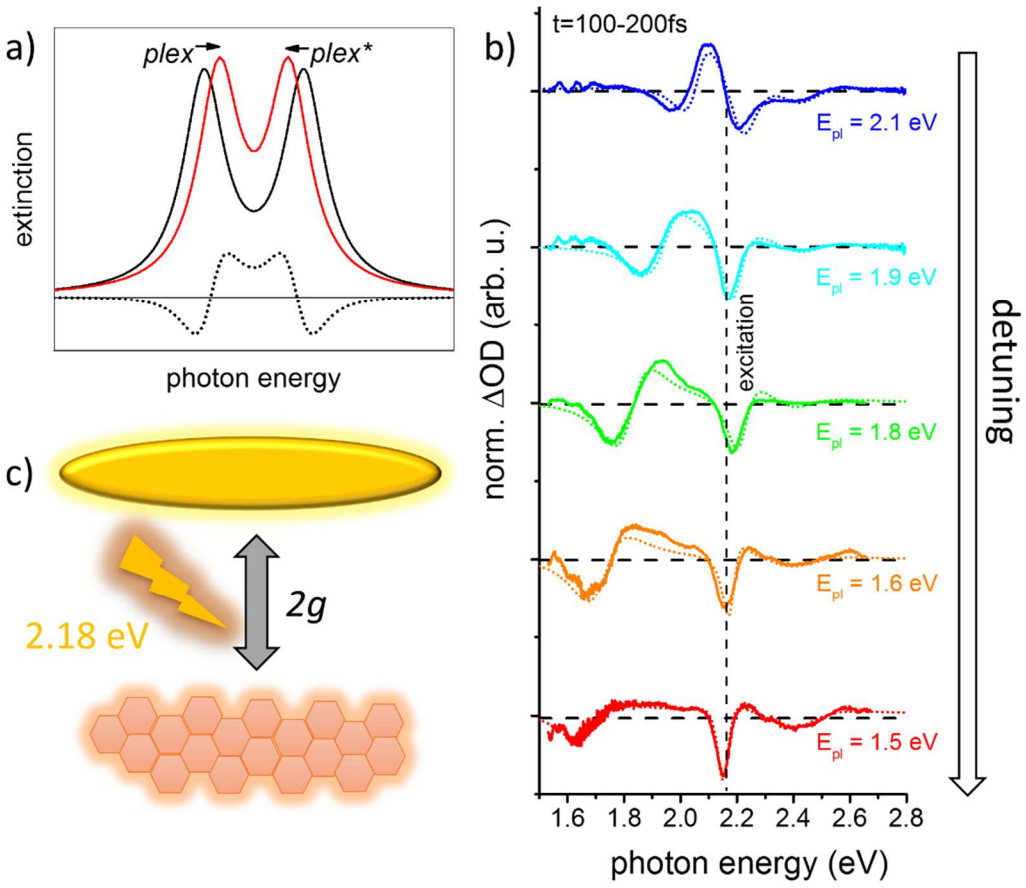

Figure 4.11: Manipulation of the coupling strength a) The Rabi splitting between both plexcitons reduces. A positive signal within the spectral gap can be observed in the b) differential absorption spectra of samples with variable spectral detuning between plasmon and exciton. c) The excitation pulse at 2.18 eV excites Rabi oscillations between plasmon and exciton. The coupling strength reduces because an exciton population is created in the dye.

For increased spectral detuning between plasmon resonance and dye transition, the spectral positions of both plexcitons are less affected by the coupling process (see Figure 4.2a). Therefore, any manipulation of the coupling strength (by the pump pulse) has less influence and the distinct positive differential absorption within the spectral gap of both plexcitons becomes weaker (see Figure 4.11b). Only a bleaching of *plex** can be found. For longer delay times, the plasmonic signatures $\Delta\Gamma_{\mathrm{plex}}$ and $\Delta\Gamma_{\mathrm{plex}^*}$ remain in the spectra. They originate from the dissipation of the plasmon oscillation of the gold nanorod analogous to the previous experiment in section 4.3.1.

4.4 Summary and discussion

The linear and nonlinear optical properties of hybrid nanoparticles consisting of gold nanorods coated with J-aggregated cyanine dye molecules were investigated with (transient) absorption spectroscopy. The structure can be understood analogously to an emitter which are the excitons of the dye molecules inside an electromagnetic resonator. The resonator mode is substituted by the plasmon polarization of the gold nanorods. Strong polarizations lead to an enhancement of the electric field on the surface of the gold particles where the dye is attached. Therefore, a feedback can be achieved likewise in an optical cavity. Since the dipole moment of the dye is enormous due to intramolecular assembly by J-aggregation, strong coupling between exciton and plasmon is observed. I. e. the dye can be periodically re-excited by the plasmon itself and polarizations are coherently exchanged between exciton and dye. The phenomenon is known as Rabi oscillation in the time domain and appears as two new resonance energies in the frequency domain. These hybrid excitations between plasmonic and excitonic modes are called *plexcitons*.

The plasmon oscillation along the longitudinal axis of the gold nanorods was used as coupling agent for the experiments in this work. By changing the aspect ratio of the gold nanorods from about 1.9 to 4.4, the resonance energy was varied in a spectral range from 2.1 to 1.4 eV. Effects on the coupling process were investigated in dependence of the spectral overlap between dye and plasmon. Both plexcitons appear as “new” resonance bands and the magnitude of the Rabi splitting was 260 meV. Similar values have been found for comparable material systems [80, 122, 124].

All experimental findings could be explained on the basis of a simple coupled Lorentz oscillator model. Both the plasmon and the exciton resonance were regarded as harmonic oscillators. The entire linear absorption behaviour of all composite particles could be accurately reproduced with one fixed value for the coupling constant. Furthermore, the same model can also explain the transient absorption in the pico- and subpicosecond time range. The goal of this study was to distinguish between plasmonic and excitonic behaviour. Transient absorption spectroscopy was found as a technique where the

plasmon resonance of the gold nanorods has a different experimental signature than the exciton transition of the dye: Upon excitation, the dephasing time of the plasmon decreases which can be observed as an increase of the respective homogenous linewidth. The relaxation occurs within a couple of picoseconds and is attributed to the heat exchange between the electron gas (to which the excitation energy first dissipates) and the crystal lattice. The hot electron gas is responsible for an increased electron-electron scattering rate which diminishes the dephasing time of the plasmon [56]. By contrast to that, the exciton transition on the dye bleaches due to occupation of the excited states and the subsequent Pauli blocking. The relaxation is one order of magnitude faster than for gold nanorods which allows an experimental distinction between plasmons and excitons.

The experiments on the composite gold-dye particles were carried out in two steps: In the first approach, the pump laser excited the transverse plasmon resonance which is not involved in the coupling. Here, an increase of the homogenous linewidth of all involved resonances (i.e. both plexcitons and the transverse plasmon) was observed. With the coupled oscillator model, it was possible to explain the behaviour: The excitation pulse heats up the electron gas, which enhances the dephasing rate of both plasmons. The Rabi oscillations (excited by the second probe pulse) are therefore stronger damped which leads to an enhanced homogenous linewidth of both plexcitons. This is equivalent to a reduction of the quality factor of the electromagnetic resonator.

The experimental key finding was that the spectral overlap between plasmon and exciton influences the relaxation dynamics of the coupled plexcitons: With this observation it was possible to show that plexcitons are hybrid states, similar to molecular orbitals with tuneable plasmonic/excitonic content. The coupled Lorentz oscillator model could quantitatively describe the experimental observation.

In the second experiment, plexcitons were directly excited by the pump pulse. Here, it was found that the coupling constant can be reduced on a subpicosecond time scale. This is noticeable by a reduction of the energetic gap between both plexcitons (equivalent to the Rabi splitting for zero spectral detuning). The behaviour could be explained on the

basis of an exciton population in the dye which diminishes the coherent exchange of polarizations with the plasmon on the gold nanorod.

The experiments show, that both the quality factor and the coupling strength can be optically manipulated on an ultrashort timescale. A simple coupled oscillator model was developed to fully explain the linear and nonlinear optical behaviour of the present system. So far similar models have been only applied to reproduce the linear optical properties like the photoluminescence [139, 140] and scattering spectra of various different metal-dye nanoparticles in the strong coupling regime [141-143]. Recently, it was possible to estimate that 70-85 excitons on a cyanine J-aggregate coherently couple to the plasmon resonance of silver nanoprisms [144]. Since the experimental parameters are similar, these numbers might be realistic for the material system used in this thesis.

The Lorentz oscillator model also works for a gold grating coated with a similar dye [145] and can reproduce phenomena related to the Stark effect in the strong coupling regime [146]. The results of this thesis might help to understand transient absorption experiments on similar hybrid particles [147-149]. Although Rabi oscillations could not be observed in the time domain like in other experimental approaches [138], the setup enabled the precise analysis of coherent effects in the strong coupling regime. Excitonic and plasmonic signatures could be successfully distinguished and their respective influences were observed separately. On the one hand, the results support that plexcitons are hybrid states between plasmons and excitons [127]. On the other hand, the present work is an example that a complex structure can be comprehensively described with a very simple model and no ambiguous assumptions. Since strong coupling phenomena are on the focus of current research [150-152], experiments even with different material systems might profit from the conclusions.

5 Four-Wave Mixing with Lead Halide Perovskites

Although the chemical compounds of methylammonium lead trihalides $CH_3NH_3PbX_3$ (X=Br,Cl,I) were already discovered in 1978 [153], solar cells of this material with double-digit efficiencies were not fabricated before 2012 [23, 25, 26, 154]. The conversion efficiency has become close to that of crystalline silicon solar cells [155]. Since the material crystalizes in a perovskite structure where the organic methylammonium cation is encapsulated within a cage spanned by eight, corner-sharing lead halide octahedra, they are frequently referred to as "lead halide perovskites".

Since the material also shows very powerful light emitting [156, 157] and lasing properties [27, 28, 158], it has attained enormous scientific interest [159-161]. The role of excitons and free charges for the optical behaviour has been thoroughly discussed [162]. Lifetimes [163], diffusion [164], mobilities [165] and charge separation [166] have been measured among many other processes. Different fabrication methods allow a morphological control of the crystals down to the nanoscale [167]. Thin platelets with the thickness of only few monolayers can be synthesized with colloidal chemistry. Effects of quantum confinement could be observed and tuned in such particles [168-170]. Materials with similar properties can also be created by replacing the methylammonium cation with, e.g. formamidinium [29, 30] and especially caesium [31-33].

Despite of all the thorough research within the past years, up to now there is an ongoing scientific debate about two important parameters: the exciton binding energy [162, 171-175] and the homogenous linewidth of exciton transitions [176, 177]. So far, measurements on single crystals have been realized only for methylammonium lead bromide [178]. Since only ensembles of particles were investigated for all other systems,

inhomogeneous effects (see 2.2.2) have to be taken into account. Therefore, any measurement of the exciton binding energy or of the homogenous linewidth from linear optical spectra becomes highly unreliable. Under this aspect, it is not surprising that the reported values of the exciton binding energy range from 2 to 50 meV for methylammonium lead iodide [38]. As explained in 2.2.2, there is a possibility to bypass ensemble effects by transient four-wave mixing in a multiparticle system. Such investigations were done extensively with GaAs/AlGaAs, GaAs/InGaAs quantum wells [100, 111, 179, 180] and cadmium chalcogenide [181, 182] structures in the 1990s. Both the homogenous linewidth and the exciton binding energy could be measured in the time domain with resolution limits down to the µeV range without the burden of single particle measurements.

In this thesis, the same techniques were applied to lead halide perovskite nanocrystals. The results are shown in this chapter. The first two sections present the results for methylammonium lead iodide (MAPbI) nanoplatelets, where the homogenous linewidth (see 5.1) and the exciton binding energy (see 5.2) could be measured. The last part of this chapter comprises preliminary results for lead bromide perovskite nanocrystals which were found to behave differently compared to their lead iodides counterparts.

5.1 Homogenous linewidth of excitons in MAPbI nanoplatelets

In this section the homogenous linewidth of excitonic transitions in MAPbI nanoplatelets is measured. Two different platelet types were chosen: thick platelets with an optical behaviour similar to bulk material and thin platelets comprised by only three atomic monolayers. Quantum confinement effects play an important role for the latter system. The homogenous linewidth is found to be a few meV at liquid helium temperature.

5.1.1 Excitons in linear absorption

Figure 5.1 depicts the absorption spectrum of ligand-stabilized MAPbI nanocrystals deposited on a film and measured at 5 K. Their lateral dimensions are on the order of several hundreds of nm. However, the thickness of the platelets shown in the black graph varies between 20 and 100 nm whereas the other crystals (orange graph) consist of three or four atomic monolayers. This is equal to a thickness of only 2 and 2.6 nm, respectively. The platelets were synthesized by Alexander Richter and Verena Hintermayr according to their recent publication [170].

The absorption onset for the thicker platelets is located at about 1.6 eV and corresponds to the band gap of the orthorhombic crystal structure of the bulk material which is present for temperatures below 170 K [162]. Despite of the nanoscale dimensions, quantum confinement effects cannot be observed, since the thickness is still larger than the exciton Bohr radius. The 1s excitonic transition appears as a distinct peak with a maximum at 1.66 eV. An estimation of the FWHM amounts to approximately 22 meV. For higher temperatures (T >170 K), the crystallization occurs in the tetragonal phase with a bandgap which is about 100 meV smaller [162]. Low temperatures (<10 K) are essential for four-wave mixing, as scattering of optical excitations with phonons especially optical phonons are diminished. Such processes shorten the dephasing time significantly and the respective time-integrated photon echo becomes difficult to resolve.

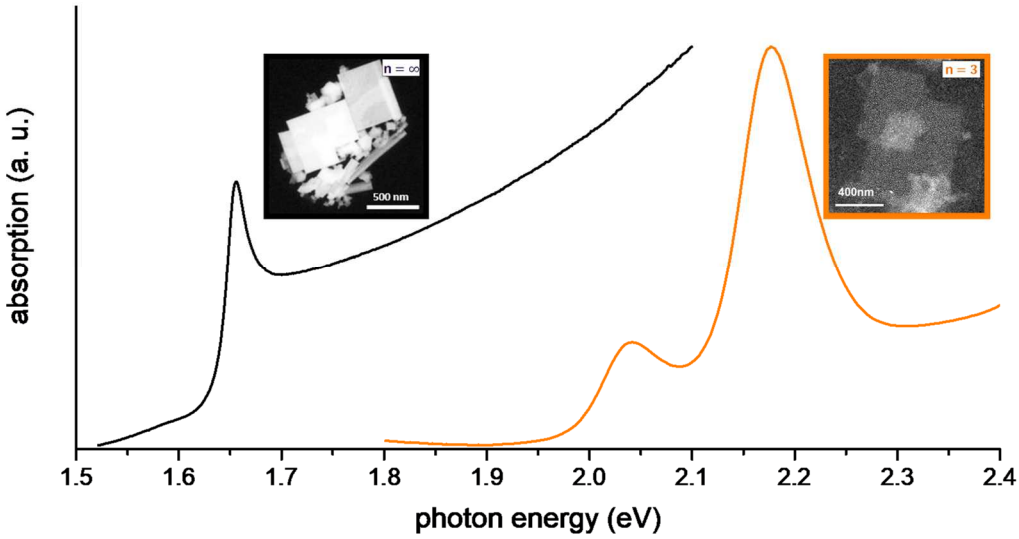

Figure 5.1: Absorption of MAPbI nanoplatelets Black graph: platelets with a thickness up to 100 nm. The absorption resembles to the bulk material. Orange graph: platelets comprised by three and four atomic monolayers. The different contrast in the electron microscopy images (taken from [170]) is due to the thickness.

Two peaks appear in the absorption spectrum of the thin nanoplatelets (orange graph in Figure 5.1): The first at 2.04 eV and the second one at 2.18 eV. They are assigned to the 1s exciton transition of the platelets comprised of four and three monolayers, respectively. An analogous assignment was done with photoluminescence spectroscopy [170]. In contrast to the thicker platelets, quantum confinement effects play a significant role: The absorption onset is blueshifted by more than 400 meV and the extinction coefficient in the spectral range of the exciton is strongly enhanced (compare both graphs in Figure 5.1). Furthermore, the slope of the continuum is clearly lower than for the thicker platelets and is nearly constant between 2.3 and 2.4 eV. This shows that the presented sample confines the carriers in one dimension and the optical behaviour is rather like a two-dimensional semiconductor (see 2.2.1). The linewidth of the exciton peak for the three-layered platelets is 74 meV.

Since the absorption measurements of both samples were carried out in an ensemble of different crystals, the exciton linewidths do not allow a determination of the respective dephasing times. As mentioned in 2.2.2, two approaches are possible to determine the

latter: Optical measurements at the single particle level and photon-echo experiments with transient four-wave mixing.

Single particle measurements are challenging especially for the present samples, since the material is colloidally synthesized. Consequently, the evaporation of the solvent during the sample preparation facilitates the formation of particle aggregates. Isolated particles might only be obtainable at very low crystal concentrations of the respective dispersion. Unfortunately, the ligand affinity to the surface of the nanoparticles is concentration dependent like for other systems [183]. Therefore, the shape of the crystals cannot be maintained at arbitrarily low crystal densities. Even if an experimental procedure can cope with the above adversities, the actual optical measurements are challenging as single crystals are very susceptible to photodegradation under the exposure of light.

5.1.2 Four-wave mixing with MAPbI nanoplatelets

As described in 2.2.2 and 3.2.2, degenerate transient four-wave mixing allows the direct determination of the dephasing time in an ensemble of absorbers. Therefore, all difficulties described above become irrelevant. In the scope of this thesis, such measurements were performed for the first time on lead halide perovskite nanocrystals. In the following section, the homogenous linewidth of the 1s exciton resonance of the MAPbI platelets in 5.1.1 is determined at 5 K. To avoid any effects caused by other transitions like the band continuum, the excitation wavelength (vertical bar in Figure 5.2a) was tuned to the lower energetic side of the exciton transition. Consequently, the optical response is mainly caused by the 1s exciton of the respective material. Two different excitation wavelengths were used to measure the time-integrated photon echo of the thicker platelets (black graph in Figure 5.2a): 785 and 775 nm equivalent to a photon energy of 1.58 and 1.6 eV, respectively. To elucidate influences of the finite length of the laser pulses, the autocorrelation function (dotted graph in Figure 5.2b) is plotted additionally.

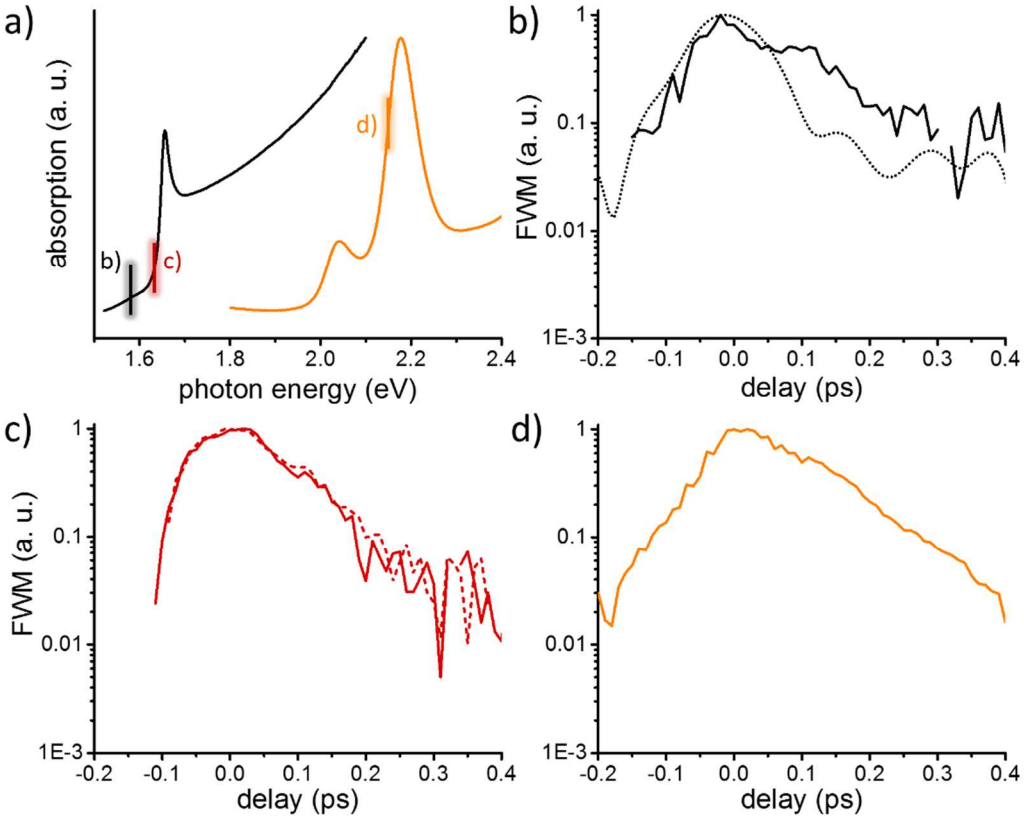

Figure 5.2: Four-wave mixing with MAPbI nanoplates a) The vertical bars in the absorption spectra indicate the excitation wavelength of the respective transient four-wave mixing experiments. For the thick, bulk-like platelets (black), the wavelengths are b) 785 nm and c) 775 nm. The quantum confined platelets (orange) comprised by three atomic monolayers were excited with d) 570 nm.

When the sample is excited at 785 nm (Figure 5.2b), the photon echo rises within 60 fs almost congruently with the autocorrelation function. However, the subsequent relaxation is clearly longer than the autocorrelation and appears approximately linear in the logarithmic plot. This shows that the dephasing time can be well resolved in the described experimental setup although the respective dynamics are very short: The 1/e-decay time (τ_{ph}) of the time-integrated photon echo in Figure 5.2b amounts to 130 fs. To estimate the homogenous linewidth of the 1s exciton, the inhomogeneous effects have to be estimated. As discussed in 2.2.2, the dephasing time is $T_2 = 2\tau_{\mathrm{ph}}$ for homogeneously broadened transitions and $T_2 = 4\tau_{\mathrm{ph}}$ in the other case. The first condition would give a homogenous linewidth of 5 meV. This value significantly deviates from the resonance width of 22 meV in the linear absorption spectrum. Therefore,

inhomogeneous effects are strongly present and cannot be neglected in the evaluation of the photon echo. Consequently, the dephasing time of the 1s exciton in the described experimental environment can be rather calculated by $T_2 = 4 \cdot 130\ \text{fs} = 520\ \text{fs}$ which gives a homogenous linewidth of 2.5 meV.

When the wavelength of the laser pulses is tuned to 775 nm (1.6 eV), the photon echo decays within 120 fs for an excitation density of $3 \cdot 10^{12}$ cm^{-2} (solid curve in Figure 5.2c) which is a similar value like for the previous measurement with 785 nm. Even though the respective dephasing time of 480 fs is only marginally faster in comparison to an excitation at 785 nm (see above) and the experimental significance is arguable, optical excitations at higher energy usually dephase faster in solids. In the present experiment, the laser excites 1s excitons in the crystals which are at slightly higher energy. The excess energy can dissipate by phonon emission and the "hot" exciton relaxes to accessible states at lower energy. This process is sometimes assigned with the rate $1/T_3$ [184] and diminishes the polarization of the material additionally.

The dynamics of the time-integrated photon echo are conserved when the excitation density is doubled (see dashed graph in Figure 5.2c). In comparison to similar experiments with other semiconductors, an acceleration is expected because enhanced exciton-exciton scattering destroys the third-order polarization additionally [185]: Due to mutual interaction mainly caused by Coulomb interaction, the phase of each "single" exciton can be broken. At an excitation density of $3\ldots6 \cdot 10^{12}$ cm^{-2}, the estimated average distance between two excitons is a few nanometres. Therefore, the most dominant scattering processes for excitons occur on a significantly shorter length scale, since no differences in the dynamics are noticeable for higher carrier densities.

The dephasing time remains similarly short when quantum confined nanoplatelets with optical properties similar to a two-dimensional semiconductor (see 5.1.1) are analysed: Figure 5.2d shows the photon echo of excitations at 570 nm (2.16 eV) which is at the lower side of the excitonic peak of platelets comprised by three monolayers. The decay constant gives about 160 fs. Since the exciton linewidth in the linear absorption spectrum is 74 meV, inhomogeneous effects are dominating and the dephasing time gives $4 \cdot 160\ \text{fs} =$

640 fs. Therefore, the homogenous linewidth of 2 meV is only a small fraction of the total exciton width observed in the absorption spectrum at liquid helium temperature. The experiments for both samples show that the exciton resonances of perovskite nanocrystals are dominated by inhomogeneous broadening at low temperatures.

5.1.3 Inhomogeneous effects

Transient four-wave mixing experiments have been extensively performed with epitaxially grown nanocrystals of gallium arsenide [100, 111, 179, 180], cadmium chalcogenides [181, 182] and tungsten molybdenum dichalcogenides [92]. The nanocrystals used in this thesis were synthesized by wet-chemistry methods and stabilized with oleylamine and oleic acid as ligands in colloidal suspension. The nanocrystals were deposited on a glass substrate by drop casting and were encapsulated with a PMMA layer. The previous measurements have shown that the exciton resonances are significantly inhomogeneously broadened at low temperature. In this chapter, some reasons for the inhomogeneous effects are considered.

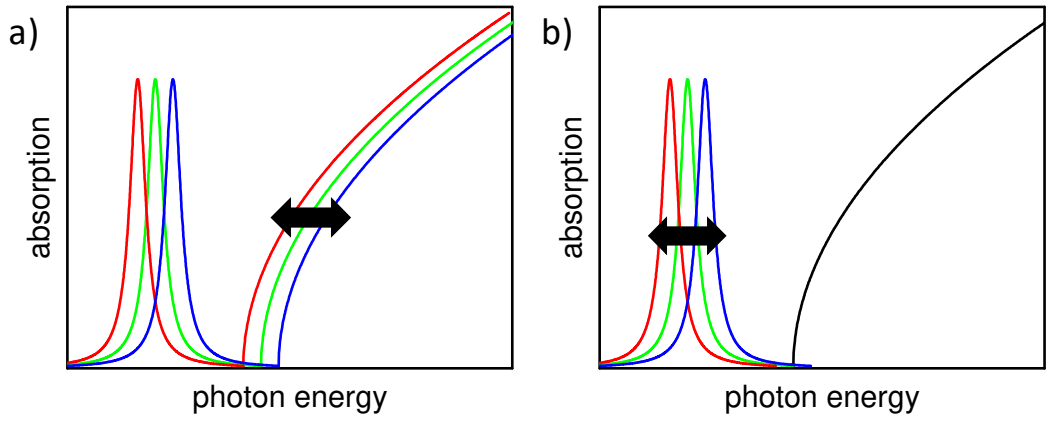

Figure 5.3: Inhomogeneous effects: a) the onset of the band continuum varies but the exciton binding energy remains constant. b) The exciton binding energies varies whereas the band continuum is unchanged. Both scenarios broaden the exciton resonance.

As illustrated in Figure 5.3 for a three-dimensional semiconductor, both the onset of the continuum and the exciton binding energy can differ statistically. Both effects influence the exciton linewidth since the transition energy changes. In every semiconductor, the local environment can change due to numerous reasons. Defects and vacancies in the

crystal structure are not only inevitable in the synthesis procedure; Schottky defects occur spontaneously due to an increase of the system`s entropy [39]. Furthermore, mechanical strain in the crystal lattice (due to defects or cumulative non-prefect crystallization) locally influences the Hamiltonian of the crystal [186]. Describing the influences of the surface is less trivial. Since every real crystal must have finite dimensions, the crystal lattice and the dielectric environment discretely change at the boundaries. Here, the termination of the nanoplatelets with ligands might come into play: Ligands do not conserve the crystal lattice. They only replace the methylammonium cations next to the surface. Vacant ligands leave behind unit cells with methylammonium vacancies. Such surface defects influence the local band structure of many semiconductors [187, 188]. This is for example different to gallium arsenide quantum wells which are embedded within aluminium arsenide capping layers. Here the crystal lattice does not end at the boundaries because both materials have a very similar lattice constant [189].

The most important inhomogeneities for the latter system are thickness variations of each gallium arsenide layer as the confinement energy is changed [190]. In the presented quantum-confined MAPbI perovskite platelets, the thickness of the platelets cannot cause fluctuations of the exciton transition energy in the range of ≈ 70 meV: Since the crystal is comprised of only three monolayers, the spectral shift (due to the confinement energy) by one layer more is already 140 meV. This can be easily verified by comparing the spectral positions of both peaks of the orange graph in Figure 5.1 which are assigned to four- and three-layered platelets.

However, the confinement energy can be influenced by the stabilizing ligands around the crystal: Since the wavefunction can penetrate into them, the crystal thickness does not solely define the confinement length [169]. The ligands are not perfectly distributed around the crystal [191]. Therefore, the confinement length can indeed vary locally and might be responsible that the exciton linewidth of quantum confined platelets (orange graph in Figure 5.1) is about three times larger than for the thicker (non-quantum confined) platelets. By contrast to that, the ligands have marginal effects on the exciton binding energy because the refractive indices of octylamine and PMMA (the

encapsulation around the crystal on the film) are almost identical: $n_{\mathrm{PMMA}} = 1.49$ [192] and $n_{\mathrm{OA}} = 1.43$ [193]. However, ligands might have an influence on the surface charge of the crystal [183] which leads to differences in the dielectric screening of the Coulomb force between electron and hole.

Another important parameter is the deposition of the nanocrystals on the film. Unlike epitaxially grown quantum wells which are grown layer by layer under controllable synthetic conditions, the distance between different crystals on the film is statistical. If they are close to each other (compared with the exciton Bohr radius), dielectric screening effects influence the binding energy of excitons close to the surface. Additionally, the wavefunctions can spill into other crystals and form minibands at different energies [194].

All the present reasons might be responsible that exciton resonances with linewidths on the order of dozens of meV are measured at helium temperature for the colloidally-fabricated samples of this thesis. This is significantly different to epitaxially grown semiconductors which have been thoroughly investigated by four-wave mixing in the past. Here, the exciton linewidth in linear absorption or photoluminescence is often only a few meV [184, 195].

5.2 Quantum beat spectroscopy with MAPbI nanoplatelets

In this section, the exciton binding energy of thick, bulk-like MAPbI platelets (black graph in Figure 5.1) is determined. With the spectral width of the laser pulse, it is possible to simultaneously excite the 1s exciton resonance and higher excited states. The dynamics of this "excitonic wave packet" appear as beats in the time-integrated photon echo which allows a determination of the exciton binding energy in the time domain.

5.2.1 Exciton binding energy determined by linear absorption spectroscopy

In the previous chapter, it was shown that the homogenous linewidth of a single exciton in MAPbI nanocrystals is in the range of only 2-3 meV at low temperature whereas resonance widths of 20-70 meV are observed in the absorption spectrum of a film of drop casted particles. Due to the strong inhomogeneous broadening, it is impossible to make reliable estimations about the exciton binding energy. Figure 5.4 shows the absorption spectrum of the thick, bulk-like nanoplatelets at 5 K again which have been investigated in the last chapter. No spectral gap appears between the exciton peak and the continuum. Consequently, the exciton binding energy E_{B} must be smaller or in the range of the resonance linewidth. This is sketched in the same figure for a realistic value of E_{B}. For the sake of clarity and the low oscillator strength, higher excitonic transitions (2s, 3s, etc.) are not shown in this scheme. Each coloured curve represents the spectrum of a microscopic sample volume with a homogenous environment. Here, exciton and continuum onset appear separated by a spectral gap which diminishes due to inhomogeneities (see 2.2.2 and 5.1.3). In the present sample, these fluctuations are obviously significantly larger and the gap completely vanishes. However, the exciton binding energy is an important parameter to understand various physical processes, especially the role of excitons in solar cells or light-emitting devices at ambient conditions.

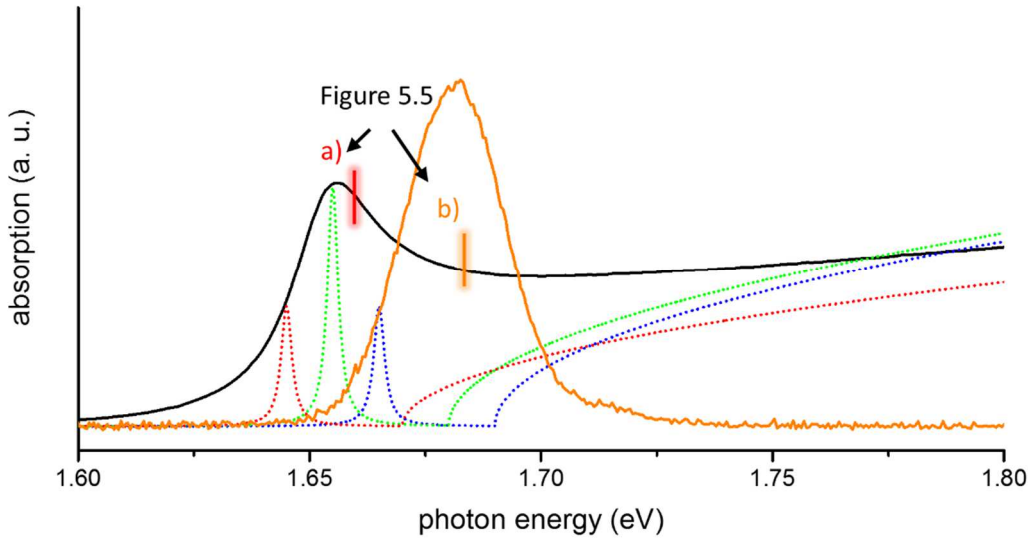

Figure 5.4: Excitons and inhomogeneous broadening The absorption spectrum of the sample (black) comprises various different absorbers (dotted) with statistical distributions of the respective transition energies. Therefore, no spectral gap between exciton resonance and continuum onset appears. The bandwidth of the laser pulse (orange) can simultaneously excite the 1s exciton and higher transitions.

Due to the reasons described above, linear absorption or photoluminescence measurements on an ensemble of particles are inappropriate for determining the exciton binding energy. Therefore, various values of E_B have been reported up to now [38]. In the following, transient four-wave mixing experiments are presented which were used to determine the exciton binding energy despite of an inhomogeneous multi-crystal system. A value of 28 ± 2 meV was determined.

5.2.2 Coherent dynamics of excitonic wave packets

Degenerate transient four-wave mixing experiments with bulk-like MAPbI nanoplatelets were carried out with 750 and 735 nm at 5 K. The respective photon energies are denoted by vertical bars in Figure 5.4, while the respective time-integrated photon echoes are shown in Figure 5.5a and b. In addition to the rise and the subsequent decay similar to the experiments with longer excitation wavelengths (described in 5.1.2), the signal is modulated. For 750 nm, a sharp kink appears at 80 fs followed by a shoulder until 150 fs. These features become more pronounced when the laser is tuned to 735 nm (see Figure 5.5b). Here, the signal is clearly modulated with an oscillation: Minima occur at 80, 250

and 350 fs with the respective maxima located at 150 and 300 fs. The time-zero delay was measured with cross-correlation and is not equivalent to the initial maximum (see explanation in 5.3.2).

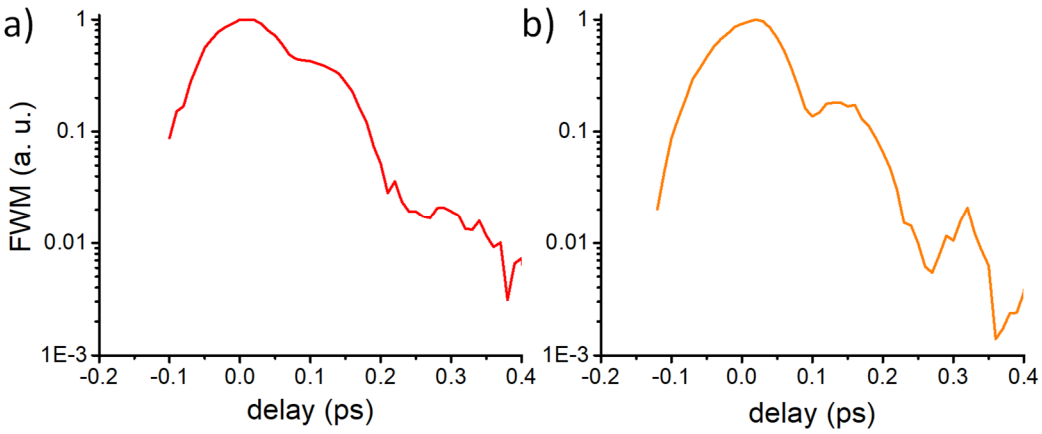

Figure 5.5: Quantum beats of MAPbI platelets Beats resulting from the coherent dynamics of hybrid excitations with different exciton transitions ("excitonic wave packet") appear in the four-wave mixing transients when the laser is tuned to a) 750 nm and b) 735 nm.

The oscillations are quantum beats (see 2.2.3) and have been assigned to the coherent dynamics of an excitonic wave packet for gallium/aluminium arsenide in previous studies [100, 111, 196] and cadmium/manganese chalcogenide [197] heterostructures. Due to the finite pulse length, the laser output has a finite spectral bandwidth, which is shown in Figure 5.4 (orange graph). As described in 2.2.1, every semiconductor has a series of excitonic transitions below the band gap at the energies $E_n = E_G - \frac{R^*}{n^2}$. If R^* is in the range of the spectral bandwidth, all excitonic resonances and the band continuum can be coherently excited when the spectrum is centred appropriately (see Figure 5.6). In this case an "excitonic wave packet" is created which is a coherent superposition of excitations with different excitons and the band continuum. The largest possible energy spacing is the binding energy E_B of the 1s exciton. Since this is equivalent with the shortest oscillation period in the time domain, the delay time of the second maximum in Figure 5.5 coincides well with the corresponding beating period T_B =150 ± 10 fs. The exciton binding energy is then given by:

$$E_{\mathrm{B}} = \frac{h}{T_B} = \frac{h}{150 \pm 10\ \mathrm{fs}} = 28 \pm 2\ \mathrm{meV}. \tag{5.1}$$

The modulations are weaker when the emission wavelength of the laser is slightly different (see Figure 5.5a with 750 nm excitation) because the spectral overlap of the laser pulse with the respective transitions reduces. Therefore, the generation of an excitonic wave packet becomes less efficient and the beating amplitude diminishes. When the laser is tuned to even longer wavelengths, only the 1s exciton can be sufficiently excited (compare with scheme in Figure 5.6) and oscillations are absent in the respective experiments (shown in 5.1.2).

Since E_{B} is inversely proportional to the beating frequency T_B, smaller values of E_B are easier to resolve in the time domain even if they are "shaded" by ensemble inhomogeneities as in the present case. The results show that four-wave mixing is a viable method for determining the exciton binding energy.

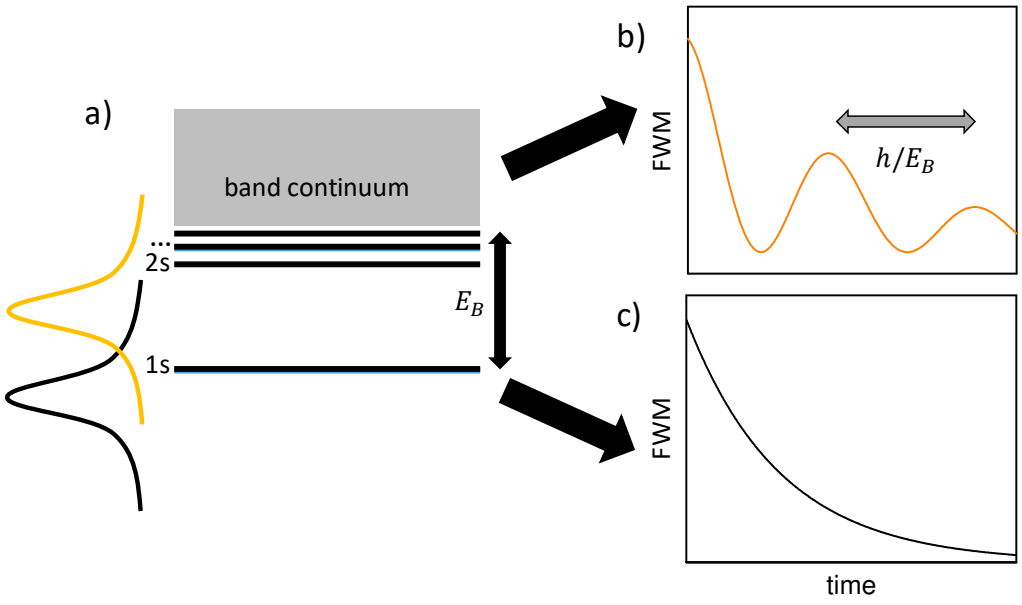

Figure 5.6: Scheme for quantum beats in semiconductors a) When the spectral width of a coherent light source (like an ultrashort laser pulse) is comparable to or larger than the exciton binding energy, an excitonic wave packet can be excited. b) The coherent dynamics can be observed as beats in the time-integrated photon echo. The beating periods are inversely proportional to the energy gaps. c) Beating phenomena are absent when only one transition resonance is excited.

The bandwidth of the laser limits the energy range of coherent excitations. This means that quantum beats cannot be observed for systems with a considerably larger exciton binding energy. This is the reason why the time-integrated photon echo of the monolayered platelets (see 5.1.2) does not exhibit any modulations although they are fabricated of the same material: Since the crystals are comprised by only three atomic monolayers, the exciton binding energy is significantly increased because of reduced dielectric screening of the Coulomb attraction and the different dimensionality (see 2.2.1).

The previous experiment has shown that degenerate four-wave mixing allows measuring the exciton binding energy for bulk-like MAPbI crystals by quantum beat spectroscopy. Since the detection is carried out in the time domain, the resolution is not limited to small values. Any binding energy smaller than the pulse spectrum ($\approx$ 50 meV) can be resolved when the corresponding dephasing time is not too short. For higher energies, other experimental techniques (like linear absorption or photoluminescence) become more reliable because the distortion of the inhomogeneous broadening reduces.

5.3 Anharmonic effects in MAPbBr nanoplatelets

In the following section four-wave mixing experiments are conducted on perovskite crystals containing bromide instead of iodide anions. Significant differences in the dephasing dynamics were found.

5.3.1 Linear absorption

When iodine ions are replaced by bromide ions, the bandgap of the respective methylammonium lead halide perovskites increases from 1.6 eV to about 2.3 eV. Nanoplatelets with the thickness of only a few atomic monolayers can be prepared with the same method as for MAPbI [170]. The sample with a corresponding absorption spectrum at 5 K is shown in Figure 5.7. It was synthesized by Lakshminarayana Polavarapu and contained platelets comprised of three and four monolayers.

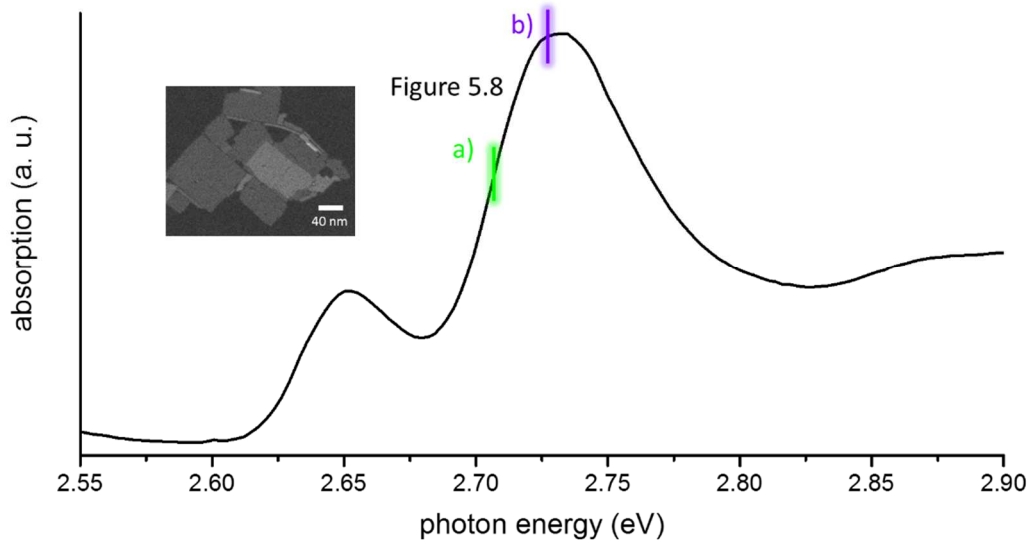

Figure 5.7: Absorption spectrum of MAPbBr nanoplatelets Exciton peaks of platelets comprised of four and three atomic monolayers appear at 2.65 and 2.74 eV, respectively.

The 1s exciton peak of the three-layered platelets is found at 2.73 eV. Due to the different band gaps, the absorption onset is blue shifted by 600 meV in comparison to the same

crystals fabricated with lead iodide anions (compare with the orange curve in Figure 5.1). The width of the exciton resonance amounts to 65 meV and is similar to that of three-layered MAPbI platelets. A shoulder appears at 2.85 eV. This can be attributed to the onset of the respective band continuum of the two-dimensional nanoplatelets. The 1s exciton resonance of the platelets comprised of four monolayers (at 2.65 eV) is at slightly lower energy (2.65 eV) because of the weaker confinement.

5.3.2 Four-wave mixing with MAPbBr nanoplatelets

In the following, time-resolved four-wave mixing experiments on methylammonium lead bromide (MAPbBr) platelets comprised of three atomic monolayers are presented. The vertical bars in Figure 5.7 indicate the excitation wavelengths of 455 and 460 nm with which the respective experiments were conducted. Figure 5.8a and b show the results for different excitation densities. The lowest excitation fluxes of 6 and $8 \cdot 10^{12}$ cm^{-2} are comparable to the experiments conducted in 5.1. However, the dynamics are clearly shorter: Both curves with the lowest excitation density appear symmetric in Figure 5.8a and b, resembling the autocorrelation function of the laser pulse (see Figure 5.2b). Consequently, the respective dynamics must be shorter than about 80 fs which gives an upper boundary of 320 fs for the respective dephasing time. The corresponding homogenous linewidth has to be higher than 4 meV.

When the excitation density is increased, the symmetric shape of the time-integrated photon echo changes: First, a shoulder at negative delay times appears which enhances and forms a second maximum when the excitation density exceeds $3 \cdot 10^{13}$ cm^{-2}. It is found about 120 fs before the initial signal maximum. At higher fluxes, the amplitude of the signal at negative times gets higher than the signal at positive times. The observed behaviour does not resemble oscillations due to quantum beats like in chapter 5.2, since a third peak or shoulder is missing and the described behaviour is dependent on the excitation flux.

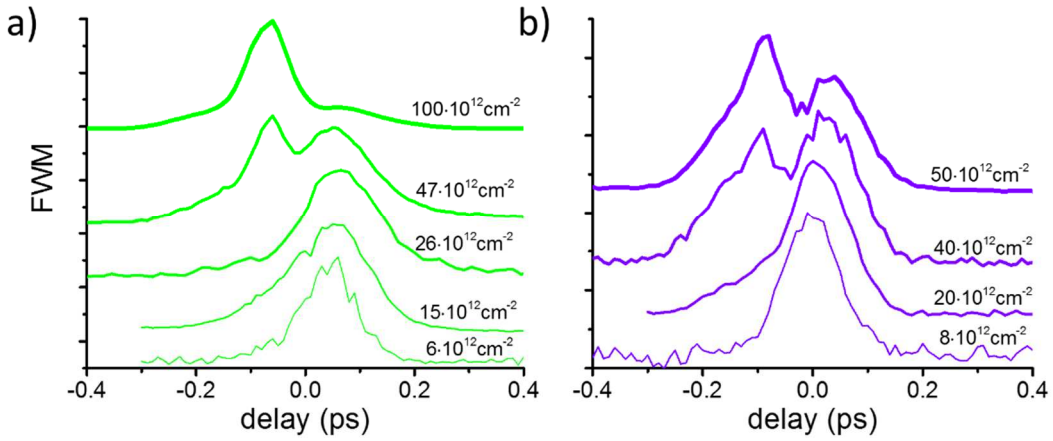

Figure 5.8: Four-wave mixing with MAPbBr nanoplatelets The excitation wavelengths were a) 460 and b) 455 nm. When the excitation flux is increased, signatures at negative delay times enhance and form a second maximum.

To investigate the physical reasons behind the excitation density dependent signal at negative delay times, a thorough theoretical analysis of the experimental data is necessary. This was beyond the scope of this thesis and is certainly an interesting basis for future works. Similar experimental findings have been reported for $In_{1-x}Ga_xAs/In_{1-x}Al_xAs$ multiple quantum wells: With increasing excitation flux, a signal at negative times is observed which passes into a second maximum for sufficiently high densities. The experimental behaviour could be reproduced by solving the semiconductor Bloch equations under the consideration of Coulomb interaction [198]. The results can be understood in a very descriptive way [199] which is illustrated in Figure 5.9 for a detector placed along the phase matched direction $2\boldsymbol{k}_2 - \boldsymbol{k}_1$. Here, $\boldsymbol{k}_1$ is the wave vector of pulse #1 and $\boldsymbol{k}_2$ of pulse #2.

As described in 3.2.2, the third-order polarization which is emitted towards the detector can be understood as the diffraction of #2 from a transient grating. The grating is formed once both pulses have arrived at the sample. If #2 arrives before #1, no electric field (or first-order polarization) of #1 is present and no diffraction along $2\boldsymbol{k}_2 - \boldsymbol{k}_1$ would be possible. However, #2 induces a first-order polarization which decays with the dephasing time T_2 (dotted red curve in Figure 5.9a). This first-order polarization can diffract from the transient grating which is formed after pulse #1 impinges on the sample. In the other case,

where pulse #1 arrives first (positive delay times, sketched in Figure 5.9b), the electric field of #2 is directly diffracted and gives the "normal" photon echo (see 2.2.2 and 3.2.2).

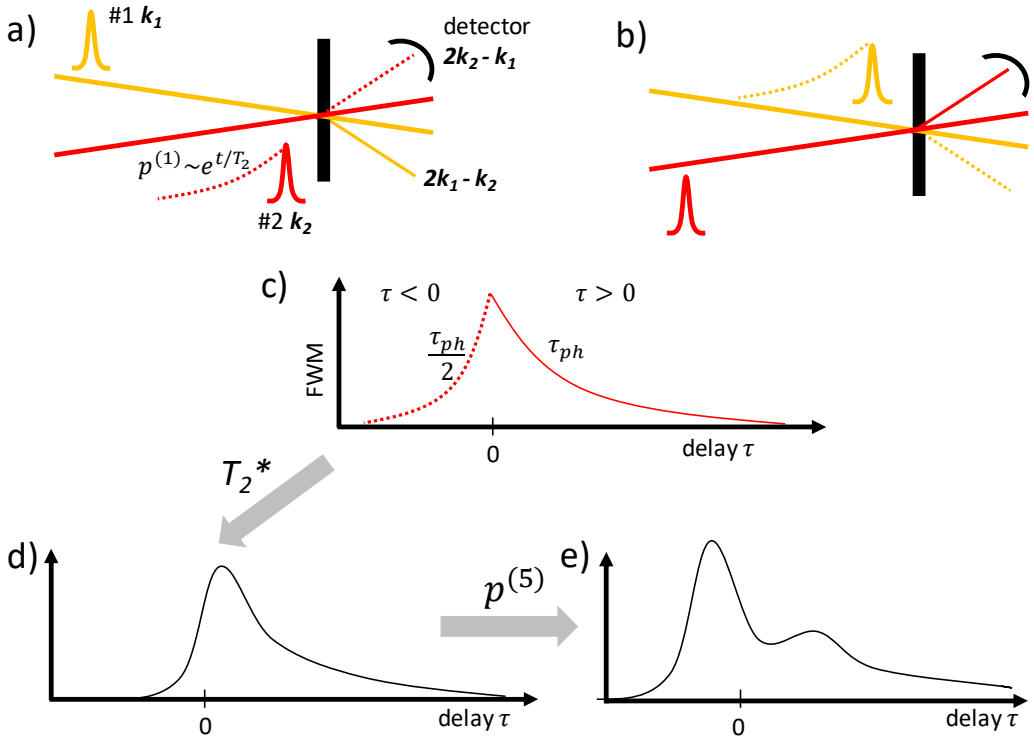

Figure 5.9: Anharmonic effects in the FWM-signal according to [199] a) At negative delay times pulse #2 cannot be deflected because #1 arrives after it. Therefore, the detector does not directly detect the pulse itself like in the case of b) positive delays. c) The signal at negative times of the time-integrated photon echo originates from the first order polarization of #2. d) Inhomogeneous broadening diminishes the signal amplitude at negative times. e) Higher polarization orders destructively interfere with the third-order polarization at the detector and give a signal minimum around the time-zero delay.

Since the process at negative times requires the interaction of two first-order polarizations, the dynamics are twice as fast. I. e. the rise time is $\frac{\tau_{ph}}{2}$ which is shown in Figure 5.9c. In the presence of inhomogeneous broadening (expressed with the decay time T_2^* of the free induction decay in Figure 5.9d), the dynamics at negative times get shorter and can completely vanish.

The minimum around the zero delay position could be also explained for $In_{1-x}Ga_xAs/In_{1-x}Al_xAs$ multiple quantum wells [199]: Not only the third-order polarization is

emitted along $2\boldsymbol{k}_2 - \boldsymbol{k}_1$ but also the fifth-order. The third- and fifth-order polarization destructively interfere at the detector if they are emitted at the same time which is definitely fulfilled close to zero delay. Therefore, the energy density at the detector reduces and the time-integrated photon echo has a local minimum (see Figure 5.9e). An experimental hint for this explanation in the present data set is the observation that both maxima in Figure 5.8b and c are separated by about 120 fs which is equivalent to the pulse length. Since the fifth-order polarization requires the interaction of five first-order polarizations, it cannot be significantly longer than the pulse itself.

The experimental findings show that changing the halide ion from lead iodide to lead bromide has significant impact on the dynamics of the time-integrated photon echo: In MAPbI crystals (see 5.1), longer dephasing times are observed and the spectra do not change to this extent by increasing the excitation flux. To confirm the influence of the lead bromide anion, control experiments are conducted where the methylammonium cation is replaced by a caesium ion. The results are shown in the following section.

5.3.3 Comparison with CsPbBr nanocrystals

In this chapter, results of four-wave mixing experiments with caesium lead bromide perovskite crystals (CsPbBr) are presented and compared with the results on MAPbBr nanocrystals (see 5.3.2). Both three- and two dimensional nanocrystals are investigated. Figure 5.10 shows the absorption spectrum at 5 K of two different CsPbBr samples with different crystal morphologies synthesized by Yu Tong. The black graph corresponds to cube-like samples with a side length of about 20 nm. Since the absorption onset is at about 2.35 eV which corresponds to the band gap of the respective bulk material [31], the optical behaviour is not governed by any quantum confinement effects. The shape of the absorption spectrum is typical for a three dimensional semiconductor: The 1s exciton peak appears at 2.44 eV with the absorption rising monotonously towards higher energies, resembling the $\sim\sqrt{E}$ behaviour (compare to 2.2.1). A linewidth of 110 meV can be estimated for the exciton resonance.

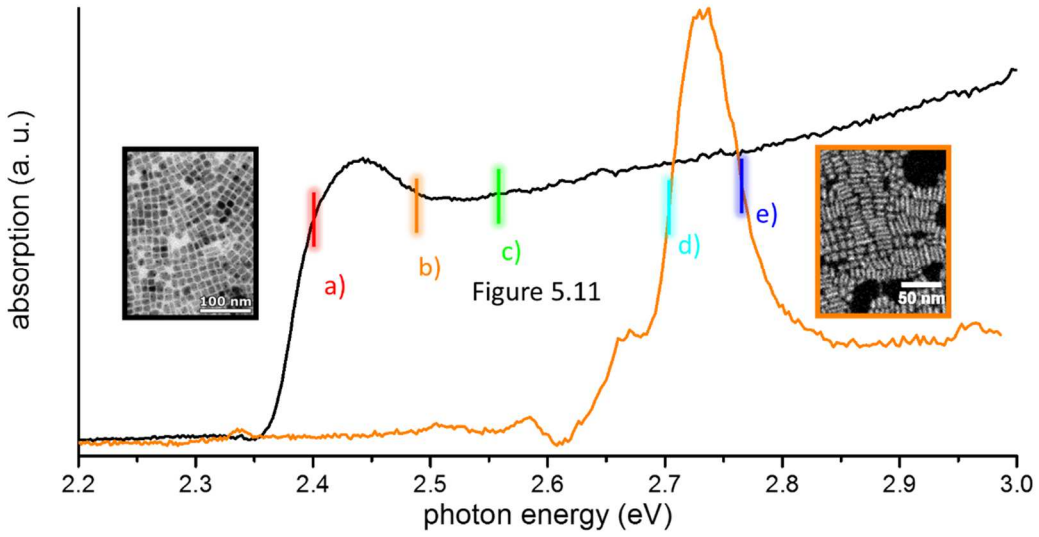

Figure 5.10: Absorption spectra of CsPbBr nanocrystals Black: Three-dimensional nanocubes. Orange: Two-dimensional nanoplatelets comprised by three atomic monolayers. Electron microscopy images (taken from [200]) show the different morphologies.

The orange graph in Figure 5.10 shows the absorption of a sample consisting of nanoplatelets with three atomic monolayers like the previously discussed MAPbI (see 5.1) and MAPbBr (see 5.3.2) nanoplatelets. Due to the confinement in one dimension, the absorption onset is shifted to higher energies by about 400 meV. The 1s exciton peak appears at 2.73 eV. Similar to the monolayered crystals containing methylammonium cations, the absorption of the continuum for energies larger than 2.8 eV is flat which is a clear spectroscopic signature of a two-dimensional crystal.

Transient four-wave mixing was conducted for both samples to determine the dynamics of the time-integrated photon echo. Different excitation wavelengths were chosen in the spectral range of the exciton peak and are marked as vertical lines in Figure 5.10. Figure 5.11a-c shows the time-integrated photon echo of the nanocubes for each excitation wavelength. Every experiment was performed with different excitation densities. All curves at the lowest excitation flux have a symmetric shape which indicates dynamics faster than the pulse duration.

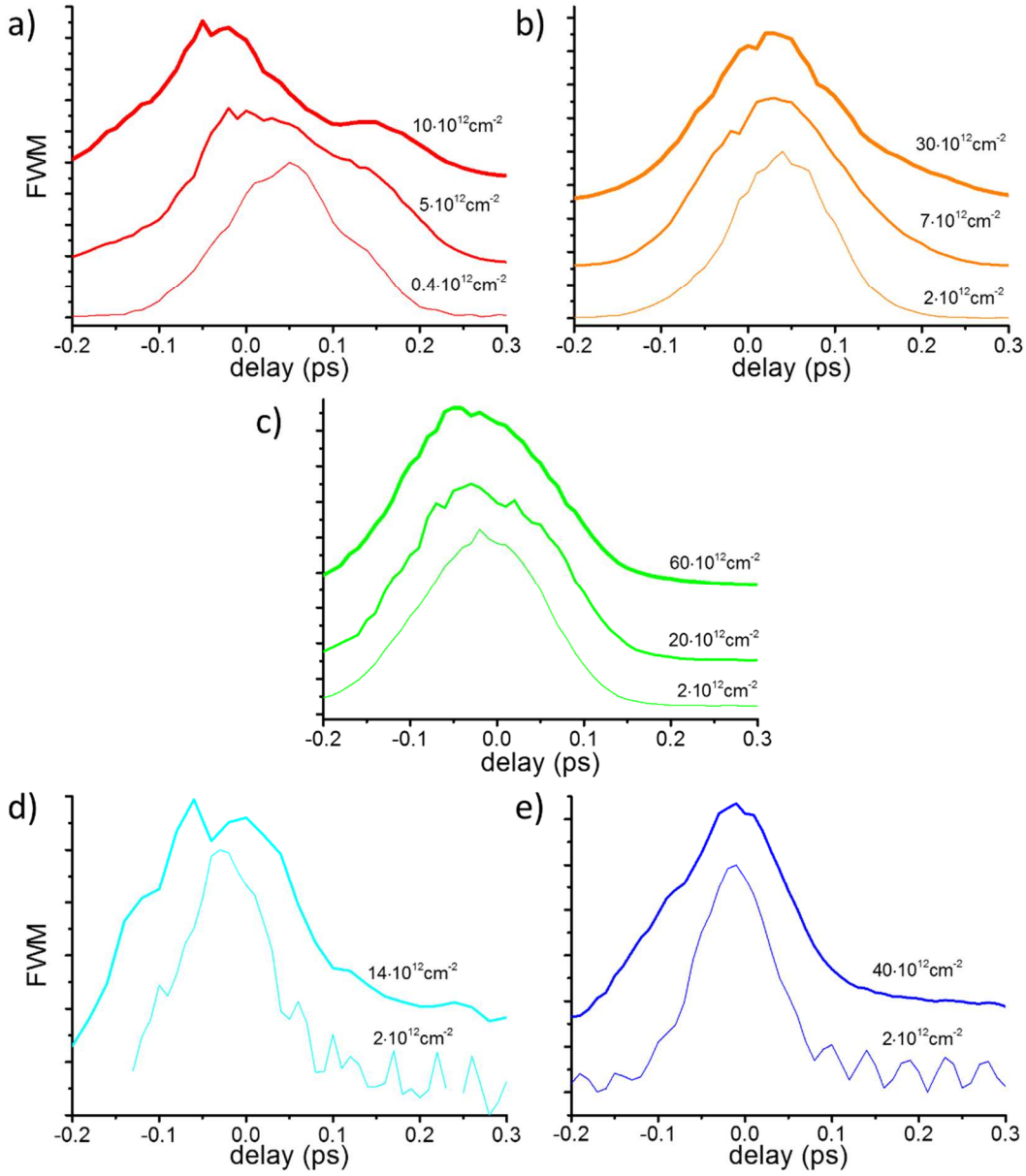

Figure 5.11: Four-wave mixing with CsPbBr nanocrystals The wavelengths are a) 515, b) 500 and c) 485 nm for the nanocubes. d) 460 and e) 450 nm are used for the two-dimensional platelets. Additional signatures at negative delay times appear for higher excitation densities when the excitation wavelength is in the spectral range of the exciton.

At the longest excitation wavelength of 515 nm, the signal at negative times enhances and the maximum shifts to negative times when the excitation flux is increased. A second maximum at 150 fs appears for a density of 10^{13} cm^{-2}. It is unlikely that these observations are related to quantum beats because the noise level would allow the detection of a third

maximum around 300 fs. The behaviour is rather similar to MAPbBr nanoplatelets (see 5.3.2).

The density-dependent effects are absent for shorter excitation wavelengths: Here the curves remain symmetric at higher photon fluxes. It can be speculated that the described effects are related to an exciton population, since the spectral overlap with the 1s exciton resonance diminishes for shorter wavelengths.

Nanoplatelets comprising three atomic monolayers of CsPbBr also show similar effects: Figure 5.11d and e show the time-integrated photon echo for two different excitation wavelengths in the vicinity of the exciton peak. Similar to all samples containing lead bromide, the signal has a symmetric shape with rise and fall times faster than 60 fs at the lowest excitation density which gives a detectable signal. For densities higher than 10^{13} cm^{-2}, the signal amplitude increases and forms a shoulder especially at negative delay times. It is not possible to increase the power further (to densities comparable to the previous measurements) because the sample was found to degrade.

The experimental findings of this and the previous section suggest that the dephasing dynamics of nanocrystals comprised by either MAPbBr or CsPbBr are significantly shorter than similar crystals fabricated of MAPbI. Therefore, the halide anion seems to influence the homogenous linewidth of excitons in lead halide perovskite nanocrystals. In addition to this, effects which are strongly dependent on the excitation density can be observed for crystals containing lead bromide anions.

5.4 Summary and discussion

In the previous chapter, four-wave mixing experiments with lead halide perovskite nanocrystals were presented. The homogenous linewidth and the binding energy of the 1s exciton could be determined for MAPbI nanoplatelets. It was found that inhomogeneous effects strongly broaden the respective resonance at low temperatures. The homogenous linewidth was measured to be in the range of 2-3 meV at 5 K, whereas the linewidth in the absorption spectrum amounts to several dozens of meV. Since an exciton binding energy of 28 ± 2 meV was determined for bulk-like crystals, it is "shaded" by the inhomogeneous effects in any linear optical spectrum. However, it can be measured in the time domain by quantum beat spectroscopy when excitons are simultaneously excited with the band continuum. By contrast to another work [201], the modulations in the time-integrated photon echo were not attributed to a contribution of localized excitons. Similar to gallium arsenide quantum wells, the beats were assigned to the coherent dynamics of excitonic wave packets [100]. The beating period allows a direct evaluation of the spectral gap between the 1s exciton and the continuum onset. Since the analysed material is similar to bulk films which are used in solar cells or light emitting devices, equivalent values for the homogenous linewidth and the exciton binding energy are expected. There has been an ongoing debate about the latter because different values have been measured so far because of the inhomogeneous broadening. Photoluminescence measurements of single crystals have been conducted only for MaPbBr [178] where a binding energy of 15 meV was measured. Since single crystal resolution is not achievable for every material, four-wave mixing is viable for various systems.

Quantum beats couldn't be observed for nanoplatelets comprising only a few atomic monolayers. This is due to a significantly increased exciton binding energy as a consequence of the confinement in one dimension and the reduced dielectric screening of the Coulomb interaction. The observation agrees with reports about the exciton Bohr radius in the range of a few nanometres [169].

The exciton binding energy and homogenous linewidth are important parameters not only for quantifying the dissociation of excitons at non-zero temperature but also for determining their radiative lifetimes [202]. This can give further insight into the operation of devices under ambient conditions. Therefore, the results are an important contribution to obtain an exact value of both quantities for bulk-like MAPbI systems. Future optical investigations might need these numbers to evaluate the respective experimental data.

In comparison to inorganic semiconductors like gallium arsenide or cadmium chalcogenide compounds [184, 203], the dephasing times of lead halide perovskites are much shorter than one picosecond. Although the experiments were performed with a kHz laser system which doesn't allow excitation densities below 10^{12} cm^{-2}, no significant dependency of the dephasing time and the excitation density was found. A linear trend is expected because exciton-exciton scattering diminishes the coherent polarization [185]. The observation that the excitation density has nearly no influence on the dynamics of the time-integrated photon echo, was confirmed by Hall et al. for MAPbI films [204]. The dephasing times calculated from their experimental data are in very good agreement to the ones obtained in this thesis. This suggests that the proportionality constant between the homogenous linewidth and the carrier density is small. More experimental work needs to be done to gain insight into the actual dephasing mechanisms of lead halide perovskites. Short dephasing times in the fs regime have been also measured by two-dimensional electronic spectroscopy for MAPbI films at room temperature [205]. In this context, it should be mentioned that the dephasing time of localized excitons is much longer because they are less sensitive to phase breaking scattering processes [206]. However, carriers in lead halide perovskites have been found to migrate up to one micrometre [164].

The radiative and non-radiative exciton recombination was measured by time resolved fluorescence [170] and transient absorption spectroscopy for the same material systems. This gives a population lifetime T_1 which is much longer than the measured dephasing time. Therefore, the polarization of the analysed crystals is mostly diminished by pure dephasing (see 2.2.2) which is typical for semiconductors [184].

As a preliminary result, it was found further that the halide ion has a significant influence on the dephasing dynamics: The homogenous linewidth of MAPbBr platelets at 5 K was measured to be more than 4 meV which is twice the value of MAPbI platelets. Furthermore, the photon echo of these nanocrystals shows signatures which depend on the excitation density. They are possibly due to higher polarization orders and a mutual interaction of the first order polarizations. Further studies regarding the theoretical description of four-wave mixing experiments with lead halide perovskite nanocrystals has to be done to understand the empirical results.

6 Conclusion

In my thesis, I conducted experiments to observe time resolved coherent dynamics in two different hybrid nanostructures. One structure were colloidal gold nanorods coated with an organic J-aggregated dye and the other one nanocrystals of organic-inorganic lead halide perovskites. Transient absorption spectroscopy and degenerate four-wave mixing were used as experimental methods. The time resolution in both experiments is only limited by the pulse duration itself which is about 100 fs.

Both structures are very interesting for the current scientific community: The first exhibits strong coupling between a plasmon polarization and an excitonic transition. Due to the interaction, hybrid resonances between plasmons and excitons are formed. In my thesis, I could prove that the optical behaviour of these mixed states shows both plasmonic and excitonic properties. The second material system was found to be very effective in the fabrication of solar cells and light emitting devices. My experiments enabled the determination of two important optical material constants: The binding energy and the homogenous linewidth of the 1s exciton.

I expect lots of future scientific work in both fields to which I have contributed with my experiments: Tuneable states with plasmonic and excitonic optical properties might become interesting especially for excitons in semiconductors. First works have already successfully shown that cadmium selenide nanoparticles can strongly couple to the surface plasmons on metal films [207]. Since excitons in semiconductors have many technical applications, hybrid states with additional plasmonic properties might enable the fabrication of new, to date unknown material types. Such studies might profit from the strategy which was developed in my experiments to distinguish plasmons and excitons by their different non-linear optical behaviour with transient absorption spectroscopy. Furthermore, I have developed an easy model to understand and reproduce the linear and non-linear optical absorption of a model system in the strong coupling regime. It can

not only be used to explain experimental phenomena of previous and future experiments with similar structures but also provides a comprehensive analysis of optical phenomena in the strong coupling regime.

The scientific interest of lead halide perovskites is still tremendous and consequently I expect increasing industrial interest on this material because first start-ups have already begun to fabricate solar cells [208]. Both the binding energy and the homogenous linewidth of the 1s exciton which have been determined in my work are frequently needed to interpret optical experiments. So far both quantities have been guessed or fitted to analyse respective data. Therefore, my results are of big scientific interest to estimate the validity of previous physical models or interpret future experiments. Since my work is purely experimental, a following comprehensive theoretical description of the third-order polarization in lead halide perovskites might help to understand the coherent dynamics of excitons.

I also want to outline here, that the effort of my experiments was to apply the method of four-wave mixing and show its experimental benefits for a colloidally synthesized system. Such experiments have been done almost exclusively on epitaxially grown semiconductors and have passed out of mind for particles synthesized by wet chemistry. Furthermore, my experiments were conducted with a kHz laser system. Time resolved four-wave mixing is usually done with lasers with a repetition rate in the MHz range to ensure low excitation densities and high sampling rates. However, the tunability of femtosecond MHz systems by optical parametric amplification is strongly limited by the low pulse power and cannot be compared with typical kHz amplifiers. My results should motivate the scientific community to conduct similar experiments with particles which have absorption spectra out of the wavelength range accessible to the common Ti:Sa oscillators. This could give insight into the coherent dynamics of many different semiconductor (nano)particles which have been synthesized within the past years.

Literature

1. Monroe, C., D. Meekhof, B. King, and D.J. Wineland, *A" Schrodinger cat" superposition state of an atom.* Science, 1996. **272**(5265): p. 1131.
2. Brune, M., E. Hagley, J. Dreyer, X. Maitre, A. Maali, C. Wunderlich, J. Raimond, and S. Haroche, *Observing the progressive decoherence of the "meter" in a quantum measurement.* Physical Review Letters, 1996. **77**(24): p. 4887.
3. Guerlin, C., J. Bernu, S. Deleglise, C. Sayrin, S. Gleyzes, S. Kuhr, M. Brune, J.-M. Raimond, and S. Haroche, *Progressive field-state collapse and quantum non-demolition photon counting.* Nature, 2007. **448**(7156): p. 889-893.
4. Schrödinger, E., *Die gegenwärtige Situation in der Quantenmechanik.* Naturwissenschaften, 1935. **23**(48): p. 807-812.
5. Schlosshauer, M., *Decoherence, the measurement problem, and interpretations of quantum mechanics.* Reviews of Modern physics, 2005. **76**(4): p. 1267.
6. Takagahara, T., *Quantum Coherence Correlation and Decoherence in Semiconductor Nanostructures*. 2003: Academic Press.
7. Haken, H. and H.C. Wolf, *The physics of atoms and quanta: introduction to experiments and theory*. Vol. 1439. 2005: Springer Science & Business Media.
8. Joos, E. and H.D. Zeh, *The emergence of classical properties through interaction with the environment.* Zeitschrift für Physik B Condensed Matter, 1985. **59**(2): p. 223-243.
9. Joos, E., H.D. Zeh, C. Kiefer, D.J. Giulini, J. Kupsch, and I.-O. Stamatescu, *Decoherence and the appearance of a classical world in quantum theory*. 2013: Springer Science & Business Media.
10. Freestone, I., N. Meeks, M. Sax, and C. Higgitt, *The Lycurgus cup—a roman nanotechnology.* Gold bulletin, 2007. **40**(4): p. 270-277.
11. Maier, S.A., *Plasmonics: fundamentals and applications*. 2007: Springer Science & Business Media.
12. Liedberg, B., C. Nylander, and I. Lunström, *Surface plasmon resonance for gas detection and biosensing.* Sensors and actuators, 1983. **4**: p. 299-304.
13. Homola, J., S.S. Yee, and G. Gauglitz, *Surface plasmon resonance sensors: review.* Sensors and Actuators B: Chemical, 1999. **54**(1): p. 3-15.
14. Willets, K.A. and R.P. Van Duyne, *Localized surface plasmon resonance spectroscopy and sensing.* Annu. Rev. Phys. Chem., 2007. **58**: p. 267-297.
15. Maier, S.A., P.G. Kik, H.A. Atwater, S. Meltzer, E. Harel, B.E. Koel, and A.A. Requicha, *Local detection of electromagnetic energy transport below the diffraction limit in metal nanoparticle plasmon waveguides.* Nature materials, 2003. **2**(4): p. 229-232.
16. Maier, S.A. and H.A. Atwater, *Plasmonics: Localization and guiding of electromagnetic energy in metal/dielectric structures.* Journal of Applied Physics, 2005. **98**(1): p. 10.
17. Bardeen, J. and W.H. Brattain, *The transistor, a semi-conductor triode.* Physical Review, 1948. **74**(2): p. 230.

18. Shirakawa, H., E.J. Louis, A.G. MacDiarmid, C.K. Chiang, and A.J. Heeger, *Synthesis of electrically conducting organic polymers: halogen derivatives of polyacetylene,(CH) x.* Journal of the Chemical Society, Chemical Communications, 1977(16): p. 578-580.
19. Tang, C.W. and S.A. VanSlyke, *Organic electroluminescent diodes.* Applied physics letters, 1987. **51**(12): p. 913-915.
20. Burroughes, J., D. Bradley, A. Brown, R. Marks, K. Mackay, R. Friend, P. Burns, and A. Holmes, *Light-emitting diodes based on conjugated polymers.* nature, 1990. **347**(6293): p. 539-541.
21. Günes, S., H. Neugebauer, and N.S. Sariciftci, *Conjugated polymer-based organic solar cells.* Chemical reviews, 2007. **107**(4): p. 1324-1338.
22. You, J., L. Dou, K. Yoshimura, T. Kato, K. Ohya, T. Moriarty, K. Emery, C.-C. Chen, J. Gao, and G. Li, *A polymer tandem solar cell with 10.6% power conversion efficiency.* Nature communications, 2013. **4**: p. 1446.
23. Lee, M.M., J. Teuscher, T. Miyasaka, T.N. Murakami, and H.J. Snaith, *Efficient hybrid solar cells based on meso-superstructured organometal halide perovskites.* Science, 2012. **338**(6107): p. 643-647.
24. Kim, H.-S., C.-R. Lee, J.-H. Im, K.-B. Lee, T. Moehl, A. Marchioro, S.-J. Moon, R. Humphry-Baker, J.-H. Yum, J.E. Moser, and M. Grätzel, *Lead iodide perovskite sensitized all-solid-state submicron thin film mesoscopic solar cell with efficiency exceeding 9%.* Scientific reports, 2012. **2**: p. 591.
25. Liu, M., M.B. Johnston, and H.J. Snaith, *Efficient planar heterojunction perovskite solar cells by vapour deposition.* Nature, 2013. **501**(7467): p. 395-398.
26. Burschka, J., N. Pellet, S.-J. Moon, R. Humphry-Baker, P. Gao, M.K. Nazeeruddin, and M. Grätzel, *Sequential deposition as a route to high-performance perovskite-sensitized solar cells.* Nature, 2013. **499**(7458): p. 316-319.
27. Xing, G., N. Mathews, S.S. Lim, N. Yantara, X. Liu, D. Sabba, M. Grätzel, S. Mhaisalkar, and T.C. Sum, *Low-temperature solution-processed wavelength-tunable perovskites for lasing.* Nature materials, 2014. **13**(5): p. 476-480.
28. Deschler, F., M. Price, S. Pathak, L.E. Klintberg, D.-D. Jarausch, R. Higler, S. Hüttner, T. Leijtens, S.D. Stranks, and H.J. Snaith, *High photoluminescence efficiency and optically pumped lasing in solution-processed mixed halide perovskite semiconductors.* The journal of physical chemistry letters, 2014. **5**(8): p. 1421-1426.
29. Jeon, N.J., J.H. Noh, W.S. Yang, Y.C. Kim, S. Ryu, J. Seo, and S.I. Seok, *Compositional engineering of perovskite materials for high-performance solar cells.* Nature, 2015. **517**(7535): p. 476-480.
30. Eperon, G.E., S.D. Stranks, C. Menelaou, M.B. Johnston, L.M. Herz, and H.J. Snaith, *Formamidinium lead trihalide: a broadly tunable perovskite for efficient planar heterojunction solar cells.* Energy & Environmental Science, 2014. **7**(3): p. 982-988.
31. Protesescu, L., S. Yakunin, M.I. Bodnarchuk, F. Krieg, R. Caputo, C.H. Hendon, R.X. Yang, A. Walsh, and M.V. Kovalenko, *Nanocrystals of cesium lead halide perovskites (CsPbX3, X= Cl, Br, and I): novel optoelectronic materials showing*

bright emission with wide color gamut. Nano letters, 2015. **15**(6): p. 3692-3696.
32. Saliba, M., T. Matsui, J.-Y. Seo, K. Domanski, J.-P. Correa-Baena, M.K. Nazeeruddin, S.M. Zakeeruddin, W. Tress, A. Abate, and A. Hagfeldt, *Cesium-containing triple cation perovskite solar cells: improved stability, reproducibility and high efficiency.* Energy & Environmental Science, 2016. **9**(6): p. 1989-1997.
33. Zhang, X., H. Lin, H. Huang, C. Reckmeier, Y. Zhang, W.C. Choy, and A.L. Rogach, *Enhancing the brightness of cesium lead halide perovskite nanocrystal based green light-emitting devices through the interface engineering with perfluorinated ionomer.* Nano letters, 2016. **16**(2): p. 1415-1420.
34. Stoumpos, C.C., C.D. Malliakas, and M.G. Kanatzidis, *Semiconducting tin and lead iodide perovskites with organic cations: phase transitions, high mobilities, and near-infrared photoluminescent properties.* Inorganic chemistry, 2013. **52**(15): p. 9019-9038.
35. Farahani, J.N., D.W. Pohl, H.-J. Eisler, and B. Hecht, *Single quantum dot coupled to a scanning optical antenna: a tunable superemitter.* Physical review letters, 2005. **95**(1): p. 017402.
36. Ringler, M., A. Schwemer, M. Wunderlich, A. Nichtl, K. Kürzinger, T. Klar, and J. Feldmann, *Shaping emission spectra of fluorescent molecules with single plasmonic nanoresonators.* Physical review letters, 2008. **100**(20): p. 203002.
37. Kinkhabwala, A., Z. Yu, S. Fan, Y. Avlasevich, K. Müllen, and W. Moerner, *Large single-molecule fluorescence enhancements produced by a bowtie nanoantenna.* Nature Photonics, 2009. **3**(11): p. 654-657.
38. Herz, L.M., *Charge-carrier dynamics in organic-inorganic metal halide perovskites.* Annual review of physical chemistry, 2016. **67**: p. 65-89.
39. Ashcroft, N.W. and N.D. Mermin, *Solid state physics.* 1976.
40. Kreibig, U. and M. Vollmer, *Optical properties of metal clusters*. Vol. 25. 2013: Springer Science & Business Media.
41. Corti, C. and R. Holliday, *Gold: science and applications*. 2009: CRC Press.
42. Choy, T.C., *Effective medium theory: principles and applications*. Vol. 165. 2015: Oxford University Press.
43. Demtröder, W., *Experimentalphysik 3: Atome, Moleküle und Festkörper.* Moleküle und Festkörper Springer Verlag, 2000.
44. Johnson, P.B. and R.-W. Christy, *Optical constants of the noble metals.* Physical review B, 1972. **6**(12): p. 4370.
45. Mie, G., *Beiträge zur Optik trüber Medien, speziell kolloidaler Metallösungen.* Annalen der physik, 1908. **330**(3): p. 377-445.
46. Sönnichsen, C., T. Franzl, T. Wilk, G. von Plessen, J. Feldmann, O. Wilson, and P. Mulvaney, *Drastic reduction of plasmon damping in gold nanorods.* Physical review letters, 2002. **88**(7): p. 077402.
47. Huergo, M.A., C.M. Maier, M.F. Castez, C. Vericat, S. Nedev, R.C. Salvarezza, A.S. Urban, and J. Feldmann, *Optical Nanoparticle Sorting Elucidates Synthesis of Plasmonic Nanotriangles.* ACS nano, 2016. **10**(3): p. 3614-3621.
48. Jain, P.K., K.S. Lee, I.H. El-Sayed, and M.A. El-Sayed, *Calculated absorption and scattering properties of gold nanoparticles of different size, shape, and*

composition: applications in biological imaging and biomedicine. J. Phys. Chem. B, 2006. **110**(14): p. 7238-7248.
49. Shankar, S.S., A. Rai, B. Ankamwar, A. Singh, A. Ahmad, and M. Sastry, *Biological synthesis of triangular gold nanoprisms.* Nature materials, 2004. **3**(7): p. 482-488.
50. Kumar, P.S., I. Pastoriza-Santos, B. Rodríguez-González, F.J.G. de Abajo, and L.M. Liz-Marzán, *High-yield synthesis and optical response of gold nanostars.* Nanotechnology, 2007. **19**(1): p. 015606.
51. Kim, F., S. Connor, H. Song, T. Kuykendall, and P. Yang, *Platonic gold nanocrystals.* Angewandte Chemie, 2004. **116**(28): p. 3759-3763.
52. Nikoobakht, B. and M.A. El-Sayed, *Preparation and growth mechanism of gold nanorods (NRs) using seed-mediated growth method.* Chemistry of Materials, 2003. **15**(10): p. 1957-1962.
53. Gans, R., *Über die form ultramikroskopischer goldteilchen.* Annalen der Physik, 1912. **342**(5): p. 881-900.
54. Griffiths, D.J., *Introduction to electrodynamics*. 2005, AAPT.
55. Geddes, C.D. and J.R. Lakowicz, *Radiative decay engineering*. Vol. 8. 2007: Springer Science & Business Media.
56. Perner, M., P. Bost, U. Lemmer, G. Von Plessen, J. Feldmann, U. Becker, M. Mennig, M. Schmitt, and H. Schmidt, *Optically induced damping of the surface plasmon resonance in gold colloids.* Physical review letters, 1997. **78**(11): p. 2192.
57. Jelley, E.E., *Spectral absorption and fluorescence of dyes in the molecular state.* Nature, 1936. **138**(3502): p. 1009-1010.
58. Scheibe, G., *Über die Veränderlichkeit der Absorptionsspektren in Lösungen und die Nebenvalenzen als ihre Ursache.* Angewandte Chemie, 1937. **50**(11): p. 212-219.
59. Scheibe, G.v., *Reversible Polymerisation als Ursache neuartiger Absorptionsbanden von Farbstoffen.* Colloid & Polymer Science, 1938. **82**(1): p. 1-14.
60. Kobayashi, T., *J-aggregates*. Vol. 2. 2012: World Scientific.
61. Tani, T., *Photographic sensitivity: theory and mechanisms*. 1995: Oxford University Press on Demand.
62. Kasha, M., H. Rawls, and M. Ashraf El-Bayoumi, *The exciton model in molecular spectroscopy.* Pure and Applied Chemistry, 1965. **11**(3-4): p. 371-392.
63. Scheibe, G. and L. Kandler, *Anisotropie organischer Farbstoffmoleküle. Nebenvalenz-Bindung als Energieüberträger.* Naturwissenschaften, 1938. **26**(24): p. 412-413.
64. Forster, T., *Energiewanderung und fluoreszenz.* Naturwissenschaften, 1946. **33**(6): p. 166-175.
65. Bücher, H. and H. Kuhn, *Scheibe aggregate formation of cyanine dyes in monolayers.* Chemical Physics Letters, 1970. **6**(3): p. 183-185.
66. Von Berlepsch, H., C. Böttcher, and L. Dähne, *Structure of J-aggregates of pseudoisocyanine dye in aqueous solution.* The Journal of Physical Chemistry B, 2000. **104**(37): p. 8792-8799.

67. Würthner, F., T.E. Kaiser, and C.R. Saha-Möller, *J-Aggregates: From Serendipitous Discovery to Supramolecular Engineering of Functional Dye Materials.* Angewandte Chemie International Edition, 2011. **50**(15): p. 3376-3410.
68. Fidder, H., J. Terpstra, and D.A. Wiersma, *Dynamics of Frenkel excitons in disordered molecular aggregates.* The Journal of chemical physics, 1991. **94**(10): p. 6895-6907.
69. Sigma-Adrich. *T4069 Sigma JC-1* 2017 [cited 2017 09.05.]; Available from: http://www.sigmaaldrich.com/catalog/product/sigma/t4069?lang=de&region=DE.
70. Slichter, C.P., *Principles of magnetic resonance*. Vol. 1. 2013: Springer Science & Business Media.
71. Knapp, E., *Lineshapes of molecular aggregates, exchange narrowing and intersite correlation.* Chemical physics, 1984. **85**(1): p. 73-82.
72. Purcell, E.M., H. Torrey, and R.V. Pound, *Resonance absorption by nuclear magnetic moments in a solid.* Physical review, 1946. **69**(1-2): p. 37.
73. Gérard, J., B. Sermage, B. Gayral, B. Legrand, E. Costard, and V. Thierry-Mieg, *Enhanced spontaneous emission by quantum boxes in a monolithic optical microcavity.* Physical review letters, 1998. **81**(5): p. 1110.
74. Kleppner, D., *Inhibited spontaneous emission.* Physical Review Letters, 1981. **47**(4): p. 233.
75. Haroche, S. and J.-M. Raimond, *Exploring the quantum: atoms, cavities, and photons*. 2006: Oxford university press.
76. Nolting, W., *Grundkurs Theoretische Physik 5/1*. Vol. 6. 2010: Springer.
77. Allen, L. and J.H. Eberly, *Optical resonance and two-level atoms*. 2012: Courier Corporation.
78. Jaynes, E.T. and F.W. Cummings, *Comparison of quantum and semiclassical radiation theories with application to the beam maser.* Proceedings of the IEEE, 1963. **51**(1): p. 89-109.
79. Shore, B.W. and P.L. Knight, *The jaynes-cummings model.* Journal of Modern Optics, 1993. **40**(7): p. 1195-1238.
80. Bellessa, J., C. Symonds, K. Vynck, A. Lemaitre, A. Brioude, L. Beaur, J. Plenet, P. Viste, D. Felbacq, and E. Cambril, *Giant Rabi splitting between localized mixed plasmon-exciton states in a two-dimensional array of nanosize metallic disks in an organic semiconductor.* Physical Review B, 2009. **80**(3): p. 033303.
81. Sakurai, J.J., S.-F. Tuan, and E.D. Commins, *Modern quantum mechanics, revised edition*. 1995, AAPT.
82. Schmitt-Rink, S., D. Chemla, and D. Miller, *Linear and nonlinear optical properties of semiconductor quantum wells.* Advances in Physics, 1989. **38**(2): p. 89-188.
83. Elliott, R., *Intensity of optical absorption by excitons.* Physical Review, 1957. **108**(6): p. 1384.
84. Shinada, M. and S. Sugano, *Interband optical transitions in extremely anisotropic semiconductors. I. Bound and unbound exciton absorption.* Journal of the Physical Society of Japan, 1966. **21**(10): p. 1936-1946.

85. Alivisatos, A., A. Harris, N. Levinos, M. Steigerwald, and L. Brus, *Electronic states of semiconductor clusters: Homogeneous and inhomogeneous broadening of the optical spectrum.* The Journal of chemical physics, 1988. **89**(7): p. 4001-4011.
86. Gammon, D., E. Snow, B. Shanabrook, D. Katzer, and D. Park, *Homogeneous linewidths in the optical spectrum of a single gallium arsenide quantum dot.* Science, 1996: p. 87-90.
87. Bayer, M. and A. Forchel, *Temperature dependence of the exciton homogeneous linewidth in In 0.60 Ga 0.40 As/GaAs self-assembled quantum dots.* Physical Review B, 2002. **65**(4): p. 041308.
88. Loudon, R., *The quantum theory of light*. 2000: OUP Oxford.
89. Meschede, D., *Optik, Licht und Laser*. 2009: Springer-Verlag.
90. Göbel, E., *Kohärente Anregungszustände in Halbleitern.* Physikalische Blätter, 1991. **47**(1): p. 47-50.
91. Di Bartolo, B., *Ultrafast Dynamics of Quantum Systems: Physical Processes and Spectroscopic Techniques*. Vol. 372. 2006: Springer Science & Business Media.
92. Moody, G., C.K. Dass, K. Hao, C.-H. Chen, L.-J. Li, A. Singh, K. Tran, G. Clark, X. Xu, and G. Berghäuser, *Intrinsic homogeneous linewidth and broadening mechanisms of excitons in monolayer transition metal dichalcogenides.* Nature communications, 2015. **6**: p. 8315.
93. Shah, J., *Ultrafast spectroscopy of semiconductors and semiconductor nanostructures*. Vol. 115. 2013: Springer Science & Business Media.
94. Warburton, R.J., C.S. Dürr, K. Karrai, J.P. Kotthaus, G. Medeiros-Ribeiro, and P.M. Petroff, *Charged Excitons in Self-Assembled Semiconductor Quantum Dots.* Physical Review Letters, 1997. **79**(26): p. 5282-5285.
95. Grossmann, P., J. Feldmann, E. Göbel, P. Thomas, D. Arent, K. Bertness, and J. Olson, *Homogeneous and inhomogeneous linewidths of excitons in partially ordered Ga0. 52In0. 48P.* Applied physics letters, 1994. **65**(18): p. 2347-2349.
96. Yajima, T. and Y. Taira, *Spatial optical parametric coupling of picosecond light pulses and transverse relaxation effect in resonant media.* Journal of the Physical Society of Japan, 1979. **47**(5): p. 1620-1626.
97. Hahn, E.L., *Spin echoes.* Physical review, 1950. **80**(4): p. 580.
98. Forrester, A.T., W.E. Parkins, and E. Gerjuoy, *On the possibility of observing beat frequencies between lines in the visible spectrum.* Physical Review, 1947. **72**(8): p. 728.
99. Forrester, A.T., R.A. Gudmundsen, and P.O. Johnson, *Photoelectric mixing of incoherent light.* Physical Review, 1955. **99**(6): p. 1691.
100. Feldmann, J., T. Meier, G. Von Plessen, M. Koch, E. Göbel, P. Thomas, G. Bacher, C. Hartmann, H. Schweizer, and W. Schäfer, *Coherent dynamics of excitonic wave packets.* Physical review letters, 1993. **70**(20): p. 3027.
101. Inc., C., *Operator´s Manual Evolution-45 High-Energy, High-Average Power Q-Switched Laser System*. 2013: Coherent Inc.
102. Inc., C., *Operator´s Manual Vitesse Diode-Pumped, Modelocked Ti:Sapphire Laser*. 2013: Coherent Inc.
103. Strickland, D. and G. Mourou, *Compression of amplified chirped optical pulses.* Optics communications, 1985. **55**(6): p. 447-449.

104. Inc., C., *Operator´s Manual Libra Ultrafast Amplifier System Laser System*. 2013: Coherent Inc.
105. Trebino, R., *Frequency-resolved optical gating: the measurement of ultrashort laser pulses*. 2012: Springer Science & Business Media.
106. Conversion, L., *OPerA Solo User´s Manual*. 2013: Light Conversion.
107. Inc., N. *Stepper Linear Stage, 100 mm, iPP motor/controller, FC Series*. 2017 [cited 2017 09.05.]; Available from: https://www.newport.com/p/FCL100.
108. Inc., N., *Newport Transient Absorption Spectrometer*. 2013: Newport Inc.
109. nzjakemartin. *PyTrA*. 2012 [cited 2017 14.07.]; Available from: https://sourceforge.net/projects/pytra/.
110. Eichler, H.J., P. Günter, and D.W. Pohl, *Laser-Induced Dynamic Gratings*. 2013: Springer Berlin Heidelberg.
111. Koch, M., J. Feldmann, G. Von Plessen, E. Göbel, P. Thomas, and K. Köhler, *Quantum beats versus polarization interference: An experimental distinction.* Physical review letters, 1992. **69**(25): p. 3631.
112. Kaluzny, Y., P. Goy, M. Gross, J. Raimond, and S. Haroche, *Observation of self-induced Rabi oscillations in two-level atoms excited inside a resonant cavity: the ringing regime of superradiance.* Physical review letters, 1983. **51**(13): p. 1175.
113. Thompson, R., G. Rempe, and H. Kimble, *Observation of normal-mode splitting for an atom in an optical cavity.* Physical Review Letters, 1992. **68**(8): p. 1132.
114. Weisbuch, C., M. Nishioka, A. Ishikawa, and Y. Arakawa, *Observation of the coupled exciton-photon mode splitting in a semiconductor quantum microcavity.* Physical Review Letters, 1992. **69**(23): p. 3314.
115. Reithmaier, J., G. Sęk, A. Löffler, C. Hofmann, S. Kuhn, S. Reitzenstein, L. Keldysh, V. Kulakovskii, T. Reinecke, and A. Forchel, *Strong coupling in a single quantum dot–semiconductor microcavity system.* Nature, 2004. **432**(7014): p. 197-200.
116. Yoshie, T., A. Scherer, J. Hendrickson, G. Khitrova, H. Gibbs, G. Rupper, C. Ell, O. Shchekin, and D. Deppe, *Vacuum Rabi splitting with a single quantum dot in a photonic crystal nanocavity.* Nature, 2004. **432**(7014): p. 200-203.
117. Lidzey, D.G., D. Bradley, M. Skolnick, T. Virgili, S. Walker, and D. Whittaker, *Strong exciton–photon coupling in an organic semiconductor microcavity.* Nature, 1998. **395**(6697): p. 53-55.
118. Lidzey, D., D. Bradley, T. Virgili, A. Armitage, M. Skolnick, and S. Walker, *Room temperature polariton emission from strongly coupled organic semiconductor microcavities.* Physical review letters, 1999. **82**(16): p. 3316.
119. Houdré, R., C. Weisbuch, R. Stanley, U. Oesterle, P. Pellandini, and M. Ilegems, *Measurement of cavity-polariton dispersion curve from angle-resolved photoluminescence experiments.* Physical Review Letters, 1994. **73**(15): p. 2043.
120. Barnes, W.L., A. Dereux, and T.W. Ebbesen, *Surface plasmon subwavelength optics.* Nature, 2003. **424**(6950): p. 824-830.
121. Bellessa, J., C. Bonnand, J. Plenet, and J. Mugnier, *Strong coupling between surface plasmons and excitons in an organic semiconductor.* Physical review letters, 2004. **93**(3): p. 036404.

122. Dintinger, J., S. Klein, F. Bustos, W.L. Barnes, and T. Ebbesen, *Strong coupling between surface plasmon-polaritons and organic molecules in subwavelength hole arrays.* Physical Review B, 2005. **71**(3): p. 035424.
123. Sugawara, Y., T. Kelf, J. Baumberg, M. Abdelsalam, and P. Bartlett, *Strong coupling between localized plasmons and organic excitons in metal nanovoids.* Physical review letters, 2006. **97**(26): p. 266808.
124. Wurtz, G.A., P.R. Evans, W. Hendren, R. Atkinson, W. Dickson, R.J. Pollard, A.V. Zayats, W. Harrison, and C. Bower, *Molecular Plasmonics with Tunable Exciton– Plasmon Coupling Strength in J-Aggregate Hybridized Au Nanorod Assemblies.* Nano letters, 2007. **7**(5): p. 1297-1303.
125. Ni, W., T. Ambjornsson, S.P. Apell, H. Chen, and J. Wang, *Observing Plasmonic–Molecular Resonance Coupling on Single Gold Nanorods.* nano letters, 2009. **10**(1): p. 77-84.
126. Fofang, N.T., N.K. Grady, Z. Fan, A.O. Govorov, and N.J. Halas, *Plexciton dynamics: exciton– plasmon coupling in a J-aggregate– Au nanoshell complex provides a mechanism for nonlinearity.* Nano letters, 2011. **11**(4): p. 1556-1560.
127. Prodan, E., C. Radloff, N.J. Halas, and P. Nordlander, *A hybridization model for the plasmon response of complex nanostructures.* Science, 2003. **302**(5644): p. 419-422.
128. Jain, P.K., S. Eustis, and M.A. El-Sayed, *Plasmon coupling in nanorod assemblies: optical absorption, discrete dipole approximation simulation, and exciton-coupling model.* The Journal of Physical Chemistry B, 2006. **110**(37): p. 18243-18253.
129. Fofang, N.T., T.-H. Park, O. Neumann, N.A. Mirin, P. Nordlander, and N.J. Halas, *Plexcitonic nanoparticles: plasmon– exciton coupling in nanoshell– J-aggregate complexes.* Nano letters, 2008. **8**(10): p. 3481-3487.
130. Liu, M. and P. Guyot-Sionnest, *Mechanism of silver (I)-assisted growth of gold nanorods and bipyramids.* The Journal of Physical Chemistry B, 2005. **109**(47): p. 22192-22200.
131. Rodríguez-Fernández, J., J. Perez-Juste, P. Mulvaney, and L.M. Liz-Marzan, *Spatially-directed oxidation of gold nanoparticles by Au (iii)– CTAB complexes.* The Journal of Physical Chemistry B, 2005. **109**(30): p. 14257-14261.
132. Dulkeith, E., A. Morteani, T. Niedereichholz, T. Klar, J. Feldmann, S. Levi, F. Van Veggel, D. Reinhoudt, M. Möller, and D. Gittins, *Fluorescence quenching of dye molecules near gold nanoparticles: radiative and nonradiative effects.* Physical review letters, 2002. **89**(20): p. 203002.
133. Olivero, J.J. and R. Longbothum, *Empirical fits to the Voigt line width: A brief review.* Journal of Quantitative Spectroscopy and Radiative Transfer, 1977. **17**(2): p. 233-236.
134. Wang, W., P. Vasa, R. Pomraenke, R. Vogelgesang, A. De Sio, E. Sommer, M. Maiuri, C. Manzoni, G. Cerullo, and C. Lienau, *Interplay between strong coupling and radiative damping of excitons and surface plasmon polaritons in hybrid nanostructures.* ACS nano, 2014. **8**(1): p. 1056-1064.
135. Demtröder, W., *Experimentalphysik 1.* Mechanik und Wärme, 2006. **7**.

136. Fidder, H., J. Knoester, and D.A. Wiersma, *Observation of the one-exciton to two-exciton transition in a J aggregate.* The Journal of chemical physics, 1993. **98**(8): p. 6564-6566.
137. Sundström, V., T. Gillbro, R. Gadonas, and A. Piskarskas, *Annihilation of singlet excitons in J aggregates of pseudoisocyanine (PIC) studied by pico-and subpicosecond spectroscopy.* The Journal of chemical physics, 1988. **89**(5): p. 2754-2762.
138. Vasa, P., W. Wang, R. Pomraenke, M. Lammers, M. Maiuri, C. Manzoni, G. Cerullo, and C. Lienau, *Real-time observation of ultrafast Rabi oscillations between excitons and plasmons in metal nanostructures with J-aggregates.* Nature Photonics, 2013. **7**(2): p. 128-132.
139. Melnikau, D., R. Esteban, D. Savateeva, A. Sánchez-Iglesias, M. Grzelczak, M.K. Schmidt, L.M. Liz-Marzán, J. Aizpurua, and Y.P. Rakovich, *Rabi splitting in photoluminescence spectra of hybrid systems of gold nanorods and J-aggregates.* The journal of physical chemistry letters, 2016. **7**(2): p. 354-362.
140. Wersäll, M., J. Cuadra, T.J. Antosiewicz, S. Balci, and T. Shegai, *Observation of mode splitting in photoluminescence of individual plasmonic nanoparticles strongly coupled to molecular excitons.* Nano Letters, 2016.
141. Schlather, A.E., N. Large, A.S. Urban, P. Nordlander, and N.J. Halas, *Near-field mediated plexcitonic coupling and giant Rabi splitting in individual metallic dimers.* Nano letters, 2013. **13**(7): p. 3281-3286.
142. Zengin, G., G. Johansson, P. Johansson, T.J. Antosiewicz, M. Käll, and T. Shegai, *Approaching the strong coupling limit in single plasmonic nanorods interacting with J-aggregates.* Scientific reports, 2013. **3**: p. 3074.
143. Zengin, G., T. Gschneidtner, R. Verre, L. Shao, T.J. Antosiewicz, K. Moth-Poulsen, M. Käll, and T. Shegai, *Evaluating conditions for strong coupling between nanoparticle plasmons and organic dyes using scattering and absorption spectroscopy.* The Journal of Physical Chemistry C, 2016. **120**(37): p. 20588-20596.
144. Zengin, G., M. Wersäll, S. Nilsson, T.J. Antosiewicz, M. Käll, and T. Shegai, *Realizing strong light-matter interactions between single-nanoparticle plasmons and molecular excitons at ambient conditions.* Physical review letters, 2015. **114**(15): p. 157401.
145. Wang, W., P. Vasa, E. Sommer, A. De Sio, P. Gross, R. Vogelgesang, and C. Lienau, *Observation of Lorentzian lineshapes in the room temperature optical spectra of strongly coupled Jaggregate/metal hybrid nanostructures by linear two-dimensional optical spectroscopy.* Journal of Optics, 2014. **16**(11): p. 114021.
146. Vasa, P., W. Wang, R. Pomraenke, M. Maiuri, C. Manzoni, G. Cerullo, and C. Lienau, *Optical Stark Effects in J-Aggregate–Metal Hybrid Nanostructures Exhibiting a Strong Exciton–Surface-Plasmon-Polariton Interaction.* Physical review letters, 2015. **114**(3): p. 036802.
147. Hao, Y.W., H.Y. Wang, Y. Jiang, Q.D. Chen, K. Ueno, W.Q. Wang, H. Misawa, and H.B. Sun, *Hybrid-State Dynamics of Gold Nanorods/Dye J-Aggregates under Strong Coupling.* Angewandte Chemie, 2011. **123**(34): p. 7970-7974.
148. Balci, S., C. Kocabas, B. Küçüköz, A. Karatay, E. Akhüseyin, H. Gul Yaglioglu, and A. Elmali, *Probing ultrafast energy transfer between excitons and*

plasmons in the ultrastrong coupling regime. Applied Physics Letters, 2014. **105**(5): p. 051105.
149. Balci, S., B. Kucukoz, O. Balci, A. Karatay, C. Kocabas, and G. Yaglioglu, *Tunable Plexcitonic Nanoparticles: A Model System for Studying Plasmon–Exciton Interaction from the Weak to the Ultrastrong Coupling Regime.* ACS Photonics, 2016. **3**(11): p. 2010-2016.
150. Zhou, N., M. Yuan, Y. Gao, D. Li, and D. Yang, *Silver Nanoshell Plasmonically Controlled Emission of Semiconductor Quantum Dots in the Strong Coupling Regime.* ACS nano, 2016. **10**(4): p. 4154-4163.
151. Li, R.-Q., D. Hernángomez-Pérez, F. García-Vidal, and A. Fernández-Domínguez, *Transformation optics approach to plasmon-exciton strong coupling in nanocavities.* Physical Review Letters, 2016. **117**(10): p. 107401.
152. Tsargorodska, A., M.L. Cartron, C. Vasilev, G. Kodali, O.A. Mass, J.J. Baumberg, P.L. Dutton, C.N. Hunter, P.i. Törmä, and G.J. Leggett, *Strong Coupling of Localized Surface Plasmons to Excitons in Light-Harvesting Complexes.* Nano Letters, 2016. **16**(11): p. 6850-6856.
153. Weber, D., *CH3NH3PbX3, ein Pb (II)-system mit kubischer Perowskitstruktur/CH3NH3PbX3, a Pb (II)-system with cubic perovskite structure.* Zeitschrift für Naturforschung B, 1978. **33**(12): p. 1443-1445.
154. Docampo, P., F.C. Hanusch, S.D. Stranks, M. Döblinger, J.M. Feckl, M. Ehrensperger, N.K. Minar, M.B. Johnston, H.J. Snaith, and T. Bein, *Solution deposition-conversion for planar heterojunction mixed halide perovskite solar cells.* Advanced Energy Materials, 2014. **4**(14).
155. Yang, W.S., J.H. Noh, N.J. Jeon, Y.C. Kim, S. Ryu, J. Seo, and S.I. Seok, *High-performance photovoltaic perovskite layers fabricated through intramolecular exchange.* Science, 2015. **348**(6240): p. 1234-1237.
156. Tan, Z.-K., R.S. Moghaddam, M.L. Lai, P. Docampo, R. Higler, F. Deschler, M. Price, A. Sadhanala, L.M. Pazos, and D. Credgington, *Bright light-emitting diodes based on organometal halide perovskite.* Nature nanotechnology, 2014. **9**(9): p. 687-692.
157. Kim, Y.H., H. Cho, J.H. Heo, T.S. Kim, N. Myoung, C.L. Lee, S.H. Im, and T.W. Lee, *Multicolored Organic/Inorganic Hybrid Perovskite Light-Emitting Diodes.* Advanced materials, 2015. **27**(7): p. 1248-1254.
158. Zhu, H., Y. Fu, F. Meng, X. Wu, Z. Gong, Q. Ding, M.V. Gustafsson, M.T. Trinh, S. Jin, and X. Zhu, *Lead halide perovskite nanowire lasers with low lasing thresholds and high quality factors.* Nature materials, 2015. **14**(6): p. 636-642.
159. Noh, J.H., S.H. Im, J.H. Heo, T.N. Mandal, and S.I. Seok, *Chemical management for colorful, efficient, and stable inorganic–organic hybrid nanostructured solar cells.* Nano letters, 2013. **13**(4): p. 1764-1769.
160. Zhou, H., Q. Chen, G. Li, S. Luo, T.-b. Song, H.-S. Duan, Z. Hong, J. You, Y. Liu, and Y. Yang, *Interface engineering of highly efficient perovskite solar cells.* Science, 2014. **345**(6196): p. 542-546.
161. Jeon, N.J., J.H. Noh, Y.C. Kim, W.S. Yang, S. Ryu, and S.I. Seok, *Solvent engineering for high-performance inorganic–organic hybrid perovskite solar cells.* Nature materials, 2014. **13**(9): p. 897-903.

162. D'Innocenzo, V., G. Grancini, M.J. Alcocer, A.R.S. Kandada, S.D. Stranks, M.M. Lee, G. Lanzani, H.J. Snaith, and A. Petrozza, *Excitons versus free charges in organo-lead tri-halide perovskites.* Nature communications, 2014. **5**.
163. Stranks, S.D., V.M. Burlakov, T. Leijtens, J.M. Ball, A. Goriely, and H.J. Snaith, *Recombination kinetics in organic-inorganic perovskites: excitons, free charge, and subgap states.* Physical Review Applied, 2014. **2**(3): p. 034007.
164. Stranks, S.D., G.E. Eperon, G. Grancini, C. Menelaou, M.J. Alcocer, T. Leijtens, L.M. Herz, A. Petrozza, and H.J. Snaith, *Electron-hole diffusion lengths exceeding 1 micrometer in an organometal trihalide perovskite absorber.* Science, 2013. **342**(6156): p. 341-344.
165. Wehrenfennig, C., G.E. Eperon, M.B. Johnston, H.J. Snaith, and L.M. Herz, *High charge carrier mobilities and lifetimes in organolead trihalide perovskites.* Advanced materials, 2014. **26**(10): p. 1584-1589.
166. Edri, E., S. Kirmayer, S. Mukhopadhyay, K. Gartsman, G. Hodes, and D. Cahen, *Elucidating the charge carrier separation and working mechanism of CH3NH3PbI3− xClx perovskite solar cells.* Nature communications, 2014. **5**.
167. Schmidt, L.C., A. Pertegás, S. González-Carrero, O. Malinkiewicz, S. Agouram, G. Minguez Espallargas, H.J. Bolink, R.E. Galian, and J. Pérez-Prieto, *Nontemplate synthesis of CH3NH3PbBr3 perovskite nanoparticles.* Journal of the American Chemical Society, 2014. **136**(3): p. 850-853.
168. Tyagi, P., S.M. Arveson, and W.A. Tisdale, *Colloidal organohalide perovskite nanoplatelets exhibiting quantum confinement.* The journal of physical chemistry letters, 2015. **6**(10): p. 1911-1916.
169. Sichert, J.A., Y. Tong, N. Mutz, M. Vollmer, S. Fischer, K.Z. Milowska, R. García Cortadella, B. Nickel, C. Cardenas-Daw, and J.K. Stolarczyk, *Quantum size effect in organometal halide perovskite nanoplatelets.* Nano letters, 2015. **15**(10): p. 6521-6527.
170. Hintermayr, V.A., A.F. Richter, F. Ehrat, M. Döblinger, W. Vanderlinden, J.A. Sichert, Y. Tong, L. Polavarapu, J. Feldmann, and A.S. Urban, *Tuning the Optical Properties of Perovskite Nanoplatelets through Composition and Thickness by Ligand-Assisted Exfoliation.* Advanced Materials, 2016. **28**(43): p. 9478-9485.
171. Sun, S., T. Salim, N. Mathews, M. Duchamp, C. Boothroyd, G. Xing, T.C. Sum, and Y.M. Lam, *The origin of high efficiency in low-temperature solution-processable bilayer organometal halide hybrid solar cells.* Energy & Environmental Science, 2014. **7**(1): p. 399-407.
172. Wu, K., A. Bera, C. Ma, Y. Du, Y. Yang, L. Li, and T. Wu, *Temperature-dependent excitonic photoluminescence of hybrid organometal halide perovskite films.* Physical Chemistry Chemical Physics, 2014. **16**(41): p. 22476-22481.
173. Yang, Y., D.P. Ostrowski, R.M. France, K. Zhu, J. Van De Lagemaat, J.M. Luther, and M.C. Beard, *Observation of a hot-phonon bottleneck in lead-iodide perovskites.* Nature Photonics, 2015.
174. Miyata, A., A. Mitioglu, P. Plochocka, O. Portugall, J.T.-W. Wang, S.D. Stranks, H.J. Snaith, and R.J. Nicholas, *Direct measurement of the exciton binding energy and effective masses for charge carriers in organic-inorganic tri-halide perovskites.* Nature Physics, 2015. **11**(7): p. 582-587.

175. Lin, Q., A. Armin, R.C.R. Nagiri, P.L. Burn, and P. Meredith, *Electro-optics of perovskite solar cells.* Nature Photonics, 2015. **9**(2): p. 106-112.
176. Wehrenfennig, C., M. Liu, H.J. Snaith, M.B. Johnston, and L.M. Herz, *Homogeneous Emission Line Broadening in the Organo Lead Halide Perovskite CH3NH3PbI3–x Cl x.* The journal of physical chemistry letters, 2014. **5**(8): p. 1300-1306.
177. Wright, A.D., C. Verdi, R.L. Milot, G.E. Eperon, M.A. Pérez-Osorio, H.J. Snaith, F. Giustino, M.B. Johnston, and L.M. Herz, *Electron-phonon coupling in hybrid lead halide perovskites.* Nature communications, 2016. **7**.
178. Tilchin, J., D.N. Dirin, G.I. Maikov, A. Sashchiuk, M.V. Kovalenko, and E. Lifshitz, *Hydrogen-like Wannier–Mott Excitons in Single Crystal of Methylammonium Lead Bromide Perovskite.* ACS nano, 2016. **10**(6): p. 6363-6371.
179. Leo, K., E. Göbel, T. Damen, J. Shah, S. Schmitt-Rink, W. Schäfer, J. Müller, K. Köhler, and P. Ganser, *Subpicosecond four-wave mixing in GaAs/Al x Ga 1− x As quantum wells.* Physical Review B, 1991. **44**(11): p. 5726.
180. Feldmann, J., K. Leo, J. Shah, D. Miller, J. Cunningham, T. Meier, G. Von Plessen, A. Schulze, P. Thomas, and S. Schmitt-Rink, *Optical investigation of Bloch oscillations in a semiconductor superlattice.* Physical Review B, 1992. **46**(11): p. 7252.
181. Noll, G., U. Siegner, S. Shevel, and E. Göbel, *Picosecond stimulated photon echo due to intrinsic excitations in semiconductor mixed crystals.* Physical review letters, 1990. **64**(7): p. 792.
182. Stanley, R., J. Hegarty, R. Fischer, J. Feldmann, E. Göbel, R. Feldman, and R. Austin, *Hot-exciton relaxation in Cd x Zn 1− x Te/ZnTe multiple quantum wells.* Physical review letters, 1991. **67**(1): p. 128.
183. Boles, M.A., D. Ling, T. Hyeon, and D.V. Talapin, *The surface science of nanocrystals.* Nature materials, 2016. **15**(2): p. 141.
184. Koch, M., D. Weber, J. Feldmann, E. Göbel, T. Meier, A. Schulze, P. Thomas, S. Schmitt-Rink, and K. Ploog, *Subpicosecond photon-echo spectroscopy on GaAs/AlAs short-period superlattices.* Physical Review B, 1993. **47**(3): p. 1532.
185. Schultheis, L., J. Kuhl, A. Honold, and C. Tu, *Ultrafast phase relaxation of excitons via exciton-exciton and exciton-electron collisions.* Physical review letters, 1986. **57**(13): p. 1635.
186. Asai, H. and K. Oe, *Energy band-gap shift with elastic strain in Ga x In1− x P epitaxial layers on (001) GaAs substrates.* Journal of Applied Physics, 1983. **54**(4): p. 2052-2056.
187. Lany, S. and A. Zunger, *Assessment of correction methods for the band-gap problem and for finite-size effects in supercell defect calculations: Case studies for ZnO and GaAs.* Physical Review B, 2008. **78**(23): p. 235104.
188. Neugebauer, J. and C.G. Van de Walle, *Atomic geometry and electronic structure of native defects in GaN.* Physical Review B, 1994. **50**(11): p. 8067.
189. Adachi, S., *GaAs, AlAs, and Al x Ga1− x As: Material parameters for use in research and device applications.* Journal of Applied Physics, 1985. **58**(3): p. R1-R29.

190. Weisbuch, C., R. Dingle, A. Gossard, and W. Wiegmann, *Optical characterization of interface disorder in GaAs-Ga1-xAlxAs multi-quantum well structures.* Solid State Communications, 1981. **38**(8): p. 709-712.
191. De Roo, J., M. Ibáñez, P. Geiregat, G. Nedelcu, W. Walravens, J. Maes, J.C. Martins, I. Van Driessche, M.V. Kovalenko, and Z. Hens, *Highly dynamic ligand binding and light absorption coefficient of cesium lead bromide perovskite nanocrystals.* 2016.
192. Grattan, K.T. and B.T. Meggitt, *Optical fiber sensor technology*. Vol. 1. 1995: Springer.
193. Kerker, M., *Colloid and Interface Science V5: Biocolloids, Polymers, Monolayers, Membranes, And General Papers*. 2012: Elsevier.
194. Even, J., L. Pedesseau, and C. Katan, *Understanding quantum confinement of charge carriers in layered 2D hybrid perovskites.* ChemPhysChem, 2014. **15**(17): p. 3733-3741.
195. Jahnke, F., M. Koch, T. Meier, J. Feldmann, W. Schäfer, P. Thomas, S. Koch, E. Göbel, and H. Nickel, *Simultaneous influence of disorder and Coulomb interaction on photon echoes in semiconductors.* Physical Review B, 1994. **50**(11): p. 8114.
196. Koch, M., G. von Plessen, J. Feldman, and E.O. Göbel, *Excitonic quantum beats in semiconductor quantum-well structures.* Chemical physics, 1996. **210**(1-2): p. 367-388.
197. Koch, M., R. Hellmann, S. Cundiff, J. Feldmann, E. Göbel, D. Yakovlev, A. Waag, and G. Landwehr, *Excitonic quantum beats in CdTeCd1− xMnxTe Quantum wells.* Solid state communications, 1993. **88**(7): p. 515-519.
198. Leo, K., M. Wegener, J. Shah, D. Chemla, E. Göbel, T. Damen, S. Schmitt-Rink, and W. Schäfer, *Effects of coherent polarization interactions on time-resolved degenerate four-wave mixing.* Physical review letters, 1990. **65**(11): p. 1340.
199. Wegener, M., D. Chemla, S. Schmitt-Rink, and W. Schäfer, *Line shape of time-resolved four-wave mixing.* Physical Review A, 1990. **42**(9): p. 5675.
200. Tong, Y., E. Bladt, M.F. Aygüler, A. Manzi, K.Z. Milowska, V.A. Hintermayr, P. Docampo, S. Bals, A.S. Urban, and L. Polavarapu, *Highly Luminescent Cesium Lead Halide Perovskite Nanocrystals with Tunable Composition and Thickness by Ultrasonication.* Angewandte Chemie International Edition, 2016. **55**(44): p. 13887-13892.
201. March, S.A., C. Clegg, D.B. Riley, D. Webber, I.G. Hill, and K.C. Hall, *Simultaneous observation of free and defect-bound excitons in CH3NH3PbI3 using four-wave mixing spectroscopy.* Scientific reports, 2016. **6**: p. 39139.
202. Feldmann, J., G. Peter, E. Göbel, P. Dawson, K. Moore, C. Foxon, and R. Elliott, *Linewidth dependence of radiative exciton lifetimes in quantum wells.* Physical review letters, 1987. **59**(20): p. 2337.
203. Hellmann, R., M. Koch, J. Feldmann, S. Cundiff, E. Göbel, D. Yakovlev, A. Waag, and G. Landwehr, *Homogeneous linewidth of excitons in semimagnetic CdTe/Cd 1− x Mn x Te multiple quantum wells.* Physical Review B, 1993. **48**(4): p. 2847.
204. March, S.A., D.B. Riley, C. Clegg, D. Webber, X. Liu, M. Dobrowolska, J.K. Furdyna, I.G. Hill, and K.C. Hall, *Four-wave mixing reveals weaker many-body*

interactions and slower dephasing in perovskite photovoltaic materials than GaAs. arXiv, 2016. **1602**.
205. Richter, J.M., F. Branchi, F.V.d.A. Camargo, B. Zhao, R.H. Friend, G. Cerullo, and F. Deschler, *Ultrafast carrier thermalization in lead iodide perovskite probed with two-dimensional electronic spectroscopy.* arXiv preprint arXiv:1701.03919, 2017.
206. Webb, M., S. Cundiff, and D. Steel, *Stimulated-picosecond-photon-echo studies of localized exciton relaxation and dephasing in GaAs/Al x Ga 1− x As multiple quantum wells.* Physical Review B, 1991. **43**(15): p. 12658.
207. Gomez, D., K. Vernon, P. Mulvaney, and T. Davis, *Surface Plasmon Mediated Strong Exciton− Photon Coupling in Semiconductor Nanocrystals.* Nano letters, 2009. **10**(1): p. 274-278.
208. Kane, A., *'Game-changing' perovskite solar tech could be cheaper and more efficient* in *The Guardian*. 2015, Guardian News & Media Ltd. : London.

Appendix

```
a="V:\data\Thomas.Simon\PhD\J Aggregates\Theory 2\B6 bare
rods different times.txt";
\\ Import of data matrix

data300fs=Import[a,{"Data",{All},{1,5}}];
\\ Definition of data vector

L=Function[{w(*w/w0*),f,w0,G(*G/w0*)},f/(w-w0-I G)];
f10=0.04;
w10=2.4;
g10=0.13;
f30=0.14;
w30=1.92;
g30=0.14;
\\ Lorentz function with parameters obtained from linear absorption

model=-Im[L[w,f10,w10,g10]]+Im[L[w,f11,w11,g11]]-
Im[L[w,f30,w30,g30]]+Im[L[w,f33,w33,g33]];
\\ Fit function, compare to equation (4.8)

fit300fs=FindFit[data300fs,{model,{f10-
0.002<f11<f10,g10<g11<g10+0.1,f30-
0.002<f33<f30,g30<g33<g30+0.1,w10-0.02<w11<w10+0.02,w30-
0.1<w33<w30+0.1}},{f11,g11,f33,g33,w11,w33},w];
\\ Find fitting parameters f11, w11, g11 and f33, w33, g33

fit300fsf=Function[{w},Evaluate[model/.fit300fs]];
\\ Fit function with parameters

Plot[fit300fsf[w],{w,1,3},Epilog-
>Map[Point,data300fs],PlotRange->All] \\ Fit function with original data
```

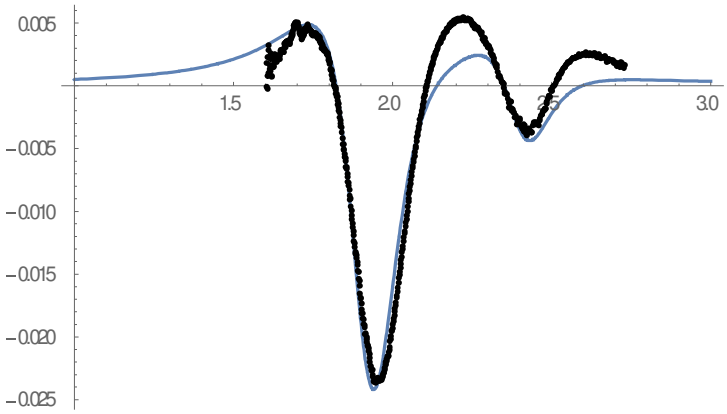

Mathemaica 10.2 was used to analyse the experimental data of chapter four. Since the reproduction of the differential absorption spectra was rather complex, the program script is given above and should be briefly explained in the following. The example shown here reproduces the transient absorption spectrum for a sample containing bare gold nanorods (similar to 4.2.1). The experimental data was composed in a matrix, where the first column was the photon energy and the other columns the corresponding differential absorption for different delay times between pump and probe pulse. I. e.: column 1: photon energy, column 2: delay 0 fs, column 3: delay 100fs, column 4: delay 200 fs, etc. Each data set which has to be fitted by the program is therefore a matrix with two columns where the first (x-coordinate) is the photon energy and the second (y-coordinate) the respective delay time. The second command creates the data matrix for a delay time of 300 fs out of the entire data which was imported with the first command line. In my program, I reproduced the spectra for 28 different delay times between 0 and 300 ps. In the script above, I present only one delay (300 fs) since the rest is just a repetition of the same commands with an exchange of the second column in the data matrix.

According to equation (4.8), the differential absorption spectra are the difference of the imaginary part of Lorentz functions. Therefore, the function $L(w) = \frac{f}{w - w_0 - ig}$ is defined. Each resonance maximum w_0 in the linear absorption spectrum (Figure 4.1) is described with respective parameters for the oscillator strength f and homogenous linewidth g (see 4.1.2). Since bare gold nanorods are analysed here, two resonance maxima occur (longitudinal and transverse plasmon resonance). The parameters (read out from the respective absorption spectrum) are defined as f_{10}, w_{10}, g_{10} for the transverse plasmon resonance and f_{30}, w_{30}, g_{30} for the longitudinal plasmon. In case that the script is used to reproduce the differential absorption of the gold-dye hybrid structures, three resonance peaks (*plex*, *plex** and the transverse plasmon) are necessary. I. e. a further Lorentzian with f_{20}, w_{20}, g_{20} has to be added.

The fit function is defined as:

$$\left(\mathrm{Im}\left(\frac{f_{11}}{w - w_{11} - ig_{11}}\right) - \mathrm{Im}\left(\frac{f_{10}}{w - w_{10} - ig_{10}}\right)\right) +$$

$$\left(\mathrm{Im}\left(\frac{f_{33}}{w - w_{33} - ig_{33}}\right) - \mathrm{Im}\left(\frac{f_{30}}{w - w_{30} - ig_{30}}\right)\right).$$

The parameters with the indices 11 and 33 are used as fitting parameters and are optimized by the program to reproduce the respective data. The equation above is equivalent to equation (4.8). Some very weak constrains for the fitting parameters have to be given that the fit converges: $f_{i0} - 0.002 < f_{ii} < f_{i0}$, $g_{i0} < g_{ii} < g_{i0} + 0.1$, $w_{10} - 0.02 < w_{11} < w_{10} + 0.02$ and $w_{30} - 0.1 < w_{33} < w_{30} + 0.1$. The fit is not sensitive to these constrains. I. e. they were more or less randomly chosen.

The last two commands define the fit function with the respective fitting parameters obtained by the program and plot it together with the original data set. In case of gold-dye hybrid structures (with three resonances) the fit function would look like:

$$\left(\mathrm{Im}\left(\frac{f_{11}}{w - w_{11} - ig_{11}}\right) - \mathrm{Im}\left(\frac{f_{10}}{w - w_{10} - ig_{10}}\right)\right) +$$

$$\left(\mathrm{Im}\left(\frac{f_{22}}{w - w_{22} - ig_{22}}\right) - \mathrm{Im}\left(\frac{f_{20}}{w - w_{20} - ig_{20}}\right)\right) +$$

$$\left(\mathrm{Im}\left(\frac{f_{33}}{w - w_{33} - ig_{33}}\right) - \mathrm{Im}\left(\frac{f_{30}}{w - w_{30} - ig_{30}}\right)\right),$$

according to equation (4.9).

Acknowledgement

The achievements of this PhD thesis would have been impossible without the advice and the contribution of many people. I would like to thank everyone who supported me during the last four years.

Prof. Dr. Jochen Feldmann, my supervisor and group leader. I would like to thank him for giving me the opportunity to work at his chair and supervise my PhD thesis. He helped me with the realization of my experiments and gave me lots of input with his broad experiences and knowledge in many productive meetings. I benefited from the great and diverse scientific environment at his chair. Under his supervision, I learned how to develop and realize my own ideas for my research projects. I am very grateful that he gave me the possibilities to present my results at international conferences where I got lots of input from other scientists and met new people working in similar fields.

Dr. Alexander Urban, for his excellent support during my research. I profited a lot from his enthusiasm and his creativity for new experiments. He always had an open ear for my scientific questions and made the achievements of this thesis possible. I also owe him special thanks for professionally revising my manuscripts and contributions.

Prof. Dr. Yury Rakovich, **Prof. Dr. Luis Liz-Marzan**, and **Dr. Dimitry Melnikau**, the collaborators from San Sebastian who synthesized the gold-dye structures and helped me editing the manuscript.

Bernhard Bohn, for the great time we worked together on perovskite nanoplatelets. Thank you for all your efforts and your great motivation. It was always entertaining and productive when we developed and conducted our experiments.

Dr. Lakshminarayana Polavarapu, **Alexander Richter**, and **Yu Tong** who synthesized the perovskite nanoplatelets and advised me on all the material issues.

Dr. Jacek Stolarczyk and **Dr. Michael Carlson**, for the successful scientific projects on photocatalytic water splitting I worked on in parallel to the work which is shown in this thesis.

I also would like to thank my other colleagues at the chair: **Verena Hintermayr** and **Carla Pernpeintner**, for helping me revising the manuscript of this thesis. Apart from that, Verena and Carla are great colleagues and always motivated me with their good mood. **Aurora Manzi**, for all your efforts you did when we worked together during your master thesis. Everyone owes you special thanks for this great workshop in Syracuse. **Florian Ehrat**, **Dr. Carlos Cardenas-Daw**, **Ludwig Hüttenhofer**, **Jasmina Sichert** and **Verena Baumann**, my office mates for the nice atmosphere in the third floor. **Patrick Urban** and **Christoph Maier**, the system admins of the chair who bailed me out of countless technical problems. **PD Dr. Theobald Lohmüller**, for supporting me finalizing this thesis. Special thanks also goes to all other PhD, master and bachelor students who shared the time with me at the chair. In this context I want to highlight **Clemens Sonnleitner** who collaborated with me during his bachelor thesis.

Gerlinde Adam, the secretary with the good heart. She reduced the amount of paperwork during my research significantly**. Stefan Niedermaier**, **Christian Holopirek**, **Katja Lyons**, and **Martin Vogel** the technical assistants who always helped me with problems in the lab or fabricated useful devices for my experiments.

I also would like to acknowledge **Alexander Grothe** and **Dr. Alexander Podlipensky** from *Coherent Inc.* for the help to maintain the femtosecond amplifier. Special thanks also goes to **Dr. Matthew Kelley** from *Newport Inc*. It was great and very constructive to meet you in California.

The greatest thank is dedicated to my family. Without the support of my parents **Margret** and **Martin Simon** it would have been never possible for me to study in Munich. I also would like to thank my sister **Kristin Simon** for the good atmosphere at home in Neumarkt and in Paris. I will never forget the support of my grandfather **Alois Simon**. Unfortunately, I could share only the first half of my PhD time with my grandmother **Belanda Simon**. I am always aware about your positive life philosophy which affected my personality that I never get upset in difficult situations.

Last but not least, I want to thank the funding agencies of my research: Bayerisches Staatsministerium für Wissenschaft, Forschung und Kunst (Solar Technologies Go Hybrid) and Nanosystems Initiative Munich. I also acknowledge the Center of Nanoscience for granting me the Travelling Award and giving me the great opportunity to attend the famous SPIE Organic Photonics+ Electronics in San Diego.